Brigham Young University
BYU ScholarsArchive

Theses and Dissertations

2015-12-01

Stochastic Simulation of Lagrangian Particle Transport in Turbulent Flows

Guangyuan Sun
Brigham Young University - Provo

Follow this and additional works at: https://scholarsarchive.byu.edu/etd

Part of the Chemical Engineering Commons

BYU ScholarsArchive Citation

Sun, Guangyuan, "Stochastic Simulation of Lagrangian Particle Transport in Turbulent Flows" (2015). *Theses and Dissertations*. 5838.
https://scholarsarchive.byu.edu/etd/5838

This Dissertation is brought to you for free and open access by BYU ScholarsArchive. It has been accepted for inclusion in Theses and Dissertations by an authorized administrator of BYU ScholarsArchive. For more information, please contact scholarsarchive@byu.edu, ellen_amatangelo@byu.edu.

Stochastic Simulation of Lagrangian Particle Transport in Turbulent Flows

Guangyuan Sun

A dissertation submitted to the faculty of
Brigham Young University
in partial fulfillment of the requirements for the degree of

Doctor of Philosophy

David O. Lignell, Chair
Thomas H. Fletcher
Larry L. Baxter
Morris D. Argyle
John C. Hewson

Department of Chemical Engineering

Brigham Young University

December 2015

Copyright © 2015 Guangyuan Sun

All Rights Reserved

ABSTRACT

Stochastic Simulation of Lagrangian Particle Transport in Turbulent Flows

Guangyuan Sun
Department of Chemical Engineering, BYU
Doctor of Philosophy

This dissertation presents the development and validation of the One Dimensional Turbulence (ODT) multiphase model in the Lagrangian reference frame. ODT is a stochastic model that captures the full range of length and time scales and provides statistical information on fine-scale turbulent-particle mixing and transport at low computational cost. The flow evolution is governed by a deterministic solution of the viscous processes and a stochastic representation of advection through stochastic domain mapping processes.

The three algorithms for Lagrangian particle transport are presented within the context of the ODT approach. The Type-I and -C models consider the particle-eddy interaction as instantaneous and continuous change of the particle position and velocity, respectively. The Type-IC model combines the features of the Type-I and -C models. The models are applied to the multiphase flows in the homogeneous decaying turbulence and turbulent round jet. Particle dispersion, dispersion coefficients, and velocity statistics are predicted and compared with experimental data. The models accurately reproduces the experimental data sets and capture particle inertial effects and trajectory crossing effect. A new adjustable particle parameter is introduced into the ODT model, and sensitivity analysis is performed to facilitate parameter estimation and selection.

A novel algorithm of the two-way momentum coupling between the particle and carrier phases is developed in the ODT multiphase model. Momentum exchange between the phases is accounted for through particle source terms in the viscous diffusion. The source term is implemented in eddy events through a new kernel transformation and an iterative procedure is required for eddy selection. This model is applied to a particle-laden turbulent jet flow, and simulation results are compared with experimental measurements. The effect of particle addition on the velocities of the gas phase is investigated. The development of particle velocity and particle number distribution are illustrated. The simulation results indicate that the model qualitatively captures the turbulent modulation with the presence of difference particle classes with different solid loadings.

The model is then extended to simulate temperature evolution of the particles in a non-isothermal hot jet, in which heat transfer between the particles and gas is considered. The flow is bounded by a wall on the one side of the domain. The simulations are performed over a range of particle inertia and thermal relaxation time scales and different initial particle locations. The present study investigates the post-blast-phase mixing between the particles, the environment that is intended to heat them up, and the ambient environment that dilutes the jet flow. The results indicate that the model can qualitatively predict the important particle statistics in jet flame.

Keywords: One Dimensional Turbulence, Lagrangian particle transport, particle-eddy interaction

ACKNOWLEDGMENTS

This dissertation could not have come to its finish without the supports from my mentors, friends and family. Dr. David Lignell, my research advisor, has not only taught me so much knowledge and many skills in CFD and combustion field, but also influenced me with his passion in research. During the most difficult times, he understood and encouraged me so that I could grow not only as an engineer but also an individual.

I am so glad to get to know Dr. Thomas Fletcher, Dr. Larry Baxter, Dr. Morris Argyle, and all the members of Dr. Lignell's research group. They have helped me from the very beginning of my graduate study, and always provided their insights and helps in need. My sincere thanks go to Dr. John Hewson and Dr. Alan Kerstein, who offered a large amount of time and effort in providing constructive feedback and help with this project.

The time in graduate school has been the most memorable five years in my life. I am blessed with great friends who witnessed the changes on me during this time. I owe my deepest gratitude to these dearest friends.

Last but not least, I would like to thank my parents, Youguang Sun and Jian Ma, and my wife, Xiaoxi Jin. No words can describe my love for them. They have been providing me everything in every possible way, and encouraged me to pursue what I believed important. I am forever grateful for the unsurpassable love.

This work was supported by the Defense Threat Reduction Agency Scientific Research Grant HDTRA-11-4503I.

TABLE OF CONTENTS

LIST OF TABLES . . . . **vi**

LIST OF FIGURES . . . . **vii**

NOMENCLATURE xi

Chapter 1 Introduction **1**
- 1.1 Motivation of the work 1
- 1.2 Scope of the work 3
- 1.3 Outline of the dissertation 4

Chapter 2 Background **7**
- 2.1 Turbulent models 7
- 2.2 Particle transport in turbulent flow 9
  - 2.2.1 Fluid reference frame and fluid-particle interaction categories 9
  - 2.2.2 Particle behavior in homogeneous isotropic turbulence 10
  - 2.2.3 Particle behavior in turbulent jet 11
- 2.3 One dimensional turbulence model 13

Chapter 3 Computational methodology and approach **15**
- 3.1 Governing equations for ODT 16
  - 3.1.1 Diffusive advancement 16
  - 3.1.2 Eddy events 19
- 3.2 Lagrangian formulation for particles 22
  - 3.2.1 Governing equations 23
  - 3.2.2 Type-I particle-eddy interaction 27
  - 3.2.3 Type-C particle-eddy interaction 32
  - 3.2.4 Instantaneous and continuous particle-eddy interaction 33
  - 3.2.5 Type-IC particle-eddy interaction 35
  - 3.2.6 Two-way momentum coupling 36
- 3.3 Temperature evolution of particles 42

Chapter 4 Particle dispersion in homogeneous turbulence **45**
- 4.1 Introduction 45
- 4.2 Model formulation 47
  - 4.2.1 ODT model description 48
  - 4.2.2 Lagrangian particle model 50
- 4.3 Results 53
  - 4.3.1 Grid-generated turbulence 53
  - 4.3.2 Particle dispersion 57
  - 4.3.3 Derived statistics 60
- 4.4 Discussion 63

4.5 Conclusions 69

Chapter 5 Particle dispersion in jet flow 71
5.1 Introduction 71
5.2 Numerical description 72
5.3 Turbulent jet configuration 73
5.3.1 Experimental details 73
5.3.2 Simulation details 73
5.4 Results and discussion 75
5.4.1 Jet evolution 75
5.4.2 Particle phase 77
5.4.3 Parameter sensitivity analysis 88
5.5 Conclusions 91

Chapter 6 Turbulent particle-laden jets 93
6.1 Introduction 93
6.2 Numerical description 94
6.3 Computational configuration 94
6.4 Results and discussion 95
6.4.1 Single phase flow 95
6.4.2 Particle-laden flow 97
6.4.3 Parameter sensitivity analysis 112
6.5 Conclusions 114

Chapter 7 Statistics of particle temperature histories 117
7.1 Introduction 117
7.2 Computational configuration 118
7.3 Results and discussion 120
7.3.1 Jet evolution 120
7.3.2 Particle evolution 122
7.4 Conclusions 131

Chapter 8 Summary and recommendations 133
8.1 Summary of results 133
8.2 Recommendation for future work 135

REFERENCES 137

LIST OF TABLES

3.1 Contribution of different forces in the equation of particle motion (Eq. 3.26) [1]. . . 25

4.1 Particle properties of Snyder and Lumley [2]. 55
4.2 Particle properties of Wells and Stock [3]. 55

5.1 Initial conditions of gas phase and particle phase (60 and 90 μm) and particle Stokes number in the 7 mm jet. 74
5.2 Particle dispersivity (60 μm and 90 μm) in the 7 mm jet. 86

6.1 Simulation initialization details of particle properties in the gas solid jet. 95

7.1 Particle properties in ethylene jet. 118

LIST OF FIGURES

3.1 Trajectories of a tracer particle (left) and a ballistic particle (right) in the y direction (ODT-aligned direction) evolve with real time; dashed lines represent the particle trajectories; solid vertical lines represent eddy events; the small domain between two small horizontal lines at the occurrence of eddy events represents the location of fluid surrounding the particle. (Adapted from John Schmidt [4]). 27
3.2 Schematic diagram of the particle-eddy interactions in the interaction and real time coordinates. The figure also illustrates the need to treat the so-called double counting effect. Dashed lines represent the trajectories of ballistic particle; rectangular box and vertical line represent eddy events; small domain between two small horizontal lines at the occurrence of eddy event represents the location of surrounding fluid of the particle. (Adapted from John Schmidt [4].) 28
3.3 Triplet map implemented on the gas phase; jagged lines indicate eddy edges; solid lines are cell boundaries; dash lines are the $1/3$ and $2/3$ fraction location of the cell before the mapping. 30
3.4 New position and velocity of the particle under the coordinate of interaction time (left) and real time (right) after the particle-eddy interaction. (Adapted from John Schmidt [4].) 31
3.5 Type-I vs. Type-C particle-eddy interaction. Shadow boxes represent eddy effect over spatial domain $[y_0, y_0 + L]$ and temporal period $\beta_p \tau_e$; single solid lines represent particle trajectory; dash line represents particle "interaction" trajectory due to particle velocity history in the Type-I interaction [5]. 34
3.6 Type-IC particle-eddy interaction in two different fluid contexts. 36

4.1 Maps of eddy sizes, locations, and occurrence times for a typical ODT realization for decaying homogeneous turbulence. Plot (a) shows instantaneous eddy locations; plot (b) illustrates eddy box extents for the particle eddy interactions (PEI) in the PEI time coordinate θ. 54
4.2 Normalized RMS streamwise velocity fluctuations: predictions and experiments of Snyder and Lumley [2] (SL), and Wells and Stock [3] (WS) on log (a) and linear (b) scales. The WS shifted data are Wells and Stock measurements shifted $15M$ to the right. 56
4.3 Comparison of ODT and experimental particle dispersion of Snyder and Lumley [2]. 57
4.4 Comparison of ODT and Wells and Stock [3] particle dispersion for 57 μm particles for four terminal velocities shown in the legend in units of (cm/s). 58
4.5 Scatter plot of eddy time scales with the corresponding mean and RMS along with particle time scales. Time zero is the dispersion reference time. Eddy information is collected from 10 representative realizations. 59

4.6 Normalized particle dispersion versus normalized particle terminal velocity for various β_p (shown in the legends). Plot (a) shows simulation results versus γ where γ is varied by varying τ_p (with $V_d = g\tau_p$), and compares to measurements of Snyder and Lumley [2]. Plot (b) shows results versus γ where γ is varied by varying particle acceleration for two particle sizes (5 μm, and 57 μm to the left and right, respectively, of the vertical dotted line), compared to measurements of Wells and Stock [3]. 61
4.7 Particle velocity fluctuation as a function of particle Stokes number. 62
4.8 Prediction of turbulent kinetic energy of particles in the study of Snyder and Lumley [2] with and without gravitational body forces. 65
4.9 Prediction of particle autocorrelation integral time scale as a function of β_p with and without body forces (a), and as a function of τ_p for hollow glass, corn pollen, and solid glass particles with and without body forces at several β_p (b). 66
4.10 Fraction of particle eddy interactions that result in particle crossing before the eddy duration $\beta_p\tau_e$, for several values of β_p. 68

5.1 Schematic of the tanh profile used to specify the initial streamwise velocity profile. 75
5.2 Normalized mean axial velocity (a) and turbulence intensity (b) along the jet centerline. Lines represent ODT predictions. Experimental measurements are represented by Cross points ($Re = 10,000$), square points ($Re = 20,000$), circular points ($Re = 30,000$). 76
5.3 Type-I dispersion of 60 μm and 90 μm particles in the 7 mm jet with $Re = 10,000$, 20,000 and 30,000. 78
5.4 Maps of eddy sizes, locations, and occurrence times for representative ODT realizations for jet flow. Plot (a) shows instantaneous eddy locations for a Type-I interaction; plot (b) shows eddy "box" extents for a Type-C interaction. 79
5.5 Type-I mean streamwise velocities of 60 μm and 90 μm particles in the 7 mm jet. . . 80
5.6 Type-C dispersion of 60 μm and 90 μm particles in the 7 mm jet with $Re = 10,000$, 20,000 and 30,000. 82
5.7 Type-C mean streamwise velocities of 60 μm and 90 μm particles in the 7 mm jet. . 83
5.8 Comparison of Lagrangian dispersion of tracer particle and "quasi" tracer predicted by the Type-C model in the 7 mm jet and $Re = 30,000$. 84
5.9 Comparison between the dispersion of 60 μm and 90 μm particles in the 7 mm jet for $Re = 10,000$ predicted by the Type-I and Type-C models. 84
5.10 Type-IC dispersion of 60 μm and 90 μm particles in the 7 mm jet with $Re = 10,000$, 20,000 and $Re = 30,000$. 85
5.11 Comparison of Lagrangian dispersion of tracer particle and "quasi" tracer predicted by the Type-IC model in the 7 mm jet and $Re = 30,000$. 86
5.12 Lagrangian dispersion of 60 μm and 90 μm particles predicted by the Type-I model in the 7 mm jet. 87
5.13 Lagrangian dispersion of 60 μm and 90 μm particles predicted by the Type-C model in the 7 mm jet. 87
5.14 Lagrangian dispersion of 60 μm and 90 μm particles predicted by the Type-IC model in the 7 mm jet. 88

5.15 β_p sensitivity on the Type-I dispersion of $60\,\mu m$ and $90\,\mu m$ particles in the $7\,mm$ jet with Re = 10,000, 20,000 and 30,000. Square symbols represent experimental measurements. 90
5.16 β_p sensitivity on the Type-C dispersion of $60\,\mu m$ and $90\,\mu m$ particles in the $7\,mm$ jet with Re = 10,000, 20,000 and 30,000. Square symbols represent experimental measurements. 90
5.17 β_p sensitivity on the Type-IC dispersion of $60\,\mu m$ and $90\,\mu m$ particles in the $7\,mm$ jet with Re = 10,000, 20,000 and 30,000. Square symbols represent experimental measurements. 91
5.18 β_p sensitivity spread on dispersion of $60\,\mu m$ and $90\,\mu m$ particles at $x/D = 50$ in the $7\,mm$ jet with $Re = 10,000$, 20,000 and 30,000. 92

6.1 Normalized mean axial velocity (a) and turbulence intensity (b) of single phase flow along the jet centerline. 96
6.2 Radial profiles of gas mean velocity normalized by initial jet velocity at different streamwise locations x = 5D, 10D and 15D. 98
6.3 Streamwise development of axial mean gas velocity along the centerline with different particle solid loading. 99
6.4 Streamwise evolution of jet width with different solid loadings SL = 0.25, 0.5 and 1.0. 100
6.5 Radial profiles of gas mean velocity normalized by initial jet velocity with different solid loadings SL = 0.25, 0.5 and 1.0 of $70\,\mu m$ particles at streamwise location x = 10D. 101
6.6 Streamwise development of axial RMS gas velocity along the centerline with different particle solid loading. 102
6.7 Mean axial centerline particle velocity at different streamwise locations. 104
6.8 Radial profiles of mean particle velocity for $70\,\mu m$ particle and SL = 0.25 at different streamwise locations x = 5D, 10D and 15D. 105
6.9 Radial profiles of mean particle velocity for $70\,\mu m$ particle and SL = 0.5 at different streamwise locations x = 5D, 10D and 15D. 106
6.10 Radial profiles of mean particle velocity for $70\,\mu m$ particle and SL = 1.0 at different streamwise locations x = 5D, 10D and 15D. 107
6.11 Radial profiles of mean particle velocity for $25\,\mu m$ particle and SL = 0.5 at different streamwise locations x = 5D, 10D and 15D. 109
6.12 Radial profiles of normalized particle number density for $70\,\mu m$ particle and SL = 0.25, 0.5 and 1.0 at different streamwise locations x = 5D, 10D and 15D. 110
6.13 Normalized particle number density over the simulation domain for $25\,\mu m$ and $70\,\mu m$ particles of solid loading of 0.5 at streamwise locations x = 5D and 15D. . . 111
6.14 Radial profiles of normalized particle number density for $70\,\mu m$ particles at streamwise location x = 10D (top) and 15D (bottom) with different β_p. 113
6.15 Mean (top) and RMS (bottom) axial gas velocity along centerline with the presence of $70\,\mu m$ particles with different β_p. 114

7.1 Schematic plot of hot jet configuration interacting with eight particles. 119

7.2 Gas temperature contours across the time-space domain simulated by the ODT model and the trajectories of the nearest and furthest particles to the jet on each side ($\tau_p = \tau_H = 0.03$ ms. 121
7.3 Contour plots for the integral time scale (left) and turbulent diffusivity (right) estimated from the turbulent kinetic energy and dissipation rate. 122
7.4 Instantaneous profiles of particle evolution (single realization). 123
7.5 Trajectories of the nearest and furthest particles to the jet on each side overlaid on the mean gas temperature contours across the time-space domain simulated by the ODT model. 124
7.6 Average particle positions. Solid lines represent $\tau_p = \tau_H = 30$ ms; dash lines represent $\tau_p = \tau_H = 0.03$ ms. 125
7.7 Average gas temperature environment experienced by particles. Solid lines represent $\tau_p = \tau_H = 30$ ms; dash lines represent $\tau_p = \tau_H = 0.03$ ms. 127
7.8 Average particle temperature. Solid lines represent $\tau_p = \tau_H = 30$ ms; dash lines represent $\tau_p = \tau_H = 0.03$ ms. 129
7.9 Maximum temperature PDF of particles. Particle time scales are represented by smallest $\tau_p = \tau_H = 0.03$ ms, small $\tau_p = \tau_H = 0.3$ ms, medium $\tau_p = \tau_H = 3$ ms, and large $\tau_p = \tau_H = 30$ ms. 131

NOMENCLATURE

A_l	Normalization constant of eddy size distribution
b	Kernal coefficient of $J(y)$
β	ODT scaling parameter
β_p	ODT scaling parameter of particle-eddy interaction
C	ODT scaling parameter
C_c	Cunningham slip factor
c	Kernal coefficient of $K(y)$
$\tilde{c}$	Parabolic minimum of c
c_p	Particle specific heat
D_d	Diffusion coefficient
D	Jet exit diameter
D_L	Lagrangian particle dispersivity
D_p	Particle dispersion
D_s	Tracer dispersion
d_p	Particle diameter
r_p	Particle radius
E_{kin}	Eddy kinetic energy
E_{vp}	Viscous energy
$\triangle E$	Change of eddy energy
ε	Turbulent dissipation
ε_{ijk}	Third-order tensor
$f(y)$	Eddy triplet map as function
$f(l)$	Eddy size distribution
g	Gravity
$g(y_0)$	Eddy location distribution
γ_{ijk}	Third-order tensor
h	Ethalpy
h_p	Particle-to-fluid heat transfer coefficient
$J(y)$	Kernel function
j	Mass diffusion flux
K_B	Empirical constant of Bassett force
K_m	Empirical constant of virtual mass force
$K(y)$	Kernel function
k	Turbulent kinetic energy
L_1	Middle position of initial velocity transition on left
L_2	Middle position of initial velocity transition on right
l	Eddy size
$\tilde{l}$	Most probable eddy size
λ	Thermal conductivity
λ_E	Eddy rate
λ_g	Mean free path of fluid gas
M	Grid spacing of homogeneous turbulence
M_w	Mean molecular weight

$\triangle M_p$	Particle momentum source
m_p	Particle mass
$\dot{m}'''$	Reaction source term
μ	Dynamic viscosity
N_p	Particle number represented by a pseudo particle
n_p	Particle number
$n_{1,j}$	Unit vector
$n_{2,j}$	Unit vector
ν	Kinematic viscosity
ω_p	Angular velocity of particle
P	Pressure
P_a	Eddy acceptance probability
$P_0(y_0,l)$	Approximate eddy distribution
Q	Minimum value of $\triangle E$
q	Heat flux
q_{rad}	Radiative flux
R	Jet radius
Re	Reynolds number
Re_p	Slip Reynolds number of particle
ρ	Density
S_p	Particle momentum source
S_β	β sensitivity spreading parameter
SL	Solid loading
St	Particle Stokes number
T	Temperature
$\triangle t_s$	Sampling period
$t_{s,c}$	Cumulative sampling time
t	Real time coordinate
t_e	Eddy lifetime
t_{eo}	Eddy occurrence time
t_L	Lagrangian fluid time scale
τ	Viscous stress
τ_e	Eddy time scale
τ_H	Particle thermal time scale
τ_k	Kolmogorov fluid time scale
τ_p	Particle inertial time scale
θ	Interaction time coordinate
θ_c	Particle crossing time
θ_{ixn}	Interaction time
U	Streamwise velocity (perpendicular to the ODT line)
U_c	Mean axial centerline velocity
U_{crms}	Centerline turbulence intensity
U_∞	Axial velocity of gas phase far from the jet
U_e	Streamwise fluid velocity felt by particle during interaction
U_K	Integral u velocity across the kernal function $K(y)$

U_m	Convective velocity
U_r	Mean axial velocity along radial direction
U_{pc}	Particle axial velocity along centerline
U_{pr}	Particle axial velocity along radial direction
V	ODT-aligned velocity
$\tilde{V}$	Characteristic jet velocity
V_d	Particle settling velocity
V_e	ODT-aligned fluid velocity felt by particle during interaction
V_K	Integral v velocity across the kernal function $K(y)$
V_p^{new}	Particle velocity after interaction
V_p^i	Integral particle velocity with eddy effect
V_p^n	Integral particle velocity without eddy effect
V_{ph}	Particle velocity history
V_{tracer}	Tracer velocity
$V^{'}$	Fluid velocity after triplet map
$V^{''}$	Fluid velocity after triplet map and kernel function
$\triangle V_p$	Integral velocity difference of particle with and without eddy effect
W	Spanwise velocity
$\tilde{W}$	Characteristic jet width
W_e	Spanwise fluid velocity felt by particle during interaction
W_K	Integral w velocity across the kernal function $K(y)$
w_l	Transition boundary layer width
X	Mole fraction
x	Streamwise direction
x_e	Eddy box size in x direction
x_0	Initial x position of particle at the beginning of interaction
$\triangle x$	Grid cell size in streamwise direction
Y	Mass fraction of chemical species
$\triangle Y_{TM}$	Displacement of a notional Lagrangian fluid particle by the triplet map at the particle location
y	ODT line direction
y_p^{new}	Particle position after interaction
y_p^{old}	Particle position before interaction
y_p^i	Integral particle displacement with eddy effect
y_p^n	Integral particle displacement without eddy effect
y_0	Left bound of eddy
$y_{1/2}$	Half of jet width
$\triangle y$	Grid cell size in ODT line direction
$\triangle y_p$	Integral displacement difference of particle with and without eddy effect
Z	ODT scaling parameter
z	Spanwise direction
z_e	Eddy box size in z direction
z_0	Initial z position of particle at the beginning of interaction

Subscripts, superscripts, and other indicators

$[\ ]^{\cdot}$	indicates [ ] is a rate

$\overline{[\ ]}$	indicates [ ] is the average value of a property
$\tilde{[\ ]}$	indicates [ ] is a characteristic property or an extremum value
$[\ ]'$	indicates [ ] is a property following triplet map or a fluctuating property
$[\ ]''$	indicates [ ] is a property following triplet map and kernel function
$[\ ]^{i}$	indicates [ ] is a property with eddy effect
$[\ ]^{n}$	indicates [ ] is a property without eddy effect
$[\ ]^{new}$	indicates [ ] is a property before triplet map
$[\ ]^{old}$	indicates [ ] is a property after triplet map
$[\ ]_0$	indicates [ ] is the initial value or property at $y = 0$ in the domain
$[\ ]_c$	indicates [ ] is a property along centerline
$[\ ]_E$	indicates [ ] is a property of eddy
$[\ ]_e$	indicates [ ] is from the east face of a grid cell
$[\ ]_g$	indicates [ ] is a property of gas phase
$[\ ]_i$	indicates [ ] is a property in streamwise direction
$[\ ]_j$	indicates [ ] is a property in ODT-aligned direction
$[\ ]_k$	indicates [ ] is a property in spanwise direction or a property of chemical species k
$[\ ]_p$	indicates [ ] is a property of particle phase
$[\ ]_r$	indicates [ ] is a property in radial direction
$[\ ]_u$	indicates [ ] is a property relevant to streamwise velocity
$[\ ]_v$	indicates [ ] is a property relevant to ODT-aligned velocity
$[\ ]_w$	indicates [ ] is from the west face of a grid cell or a property relevant to spanwise velocity

CHAPTER 1. INTRODUCTION

1.1 Motivation of the work

In the field of fluid mechanics, turbulent multiphase flows can be used to refer to any turbulent fluid flow consisting of more than one phase or component flowing simultaneously in the mixture, having some levels of phase separation at a scale well above the molecular level. Multiphase flows can be classified into many different forms according to the state of the different phases or components. Gas-particle flows, identified as gas-solid or gas-droplet flows, are considered with the motion of suspended solid or droplet in the gas phase. The functional problems involving turbulent gas-particle flows exist in a broad range of industrial applications, human body system and natural environments that human beings live. Examples of common turbulent gas-particle flows based upon the classifications are listed below.

Gas-solid flows:

- Pneumatic transport, dust collectors, fluidized bed mixing, solid propellant rockets, combustion of pulverized coal, spray drying, spray casting
- Natural sand blasting, volcanoes, avalanches
- Biological aerosols, dust particles, smoke (finely soot particles), rain droplets, mist formation

Gas-droplet flows:

- Industrial heat exchangers, boiling water and pressurized water nuclear reactors, chemical desalination systems, internal combustion engines, liquid propellant rockets
- Natural ocean waves
- Biological blood flow

The above examples are intended to cover an overview of the broad range of applications of the turbulent gas-particle fluid system. These application examples also clearly reflect the extensive challenges that exist when such flows are constantly being dealt with.

The complex nature of particle-laden flows in contrast to single-phase flows originates because of the existence of dynamically changing interfaces, significant discontinuities of the fluid properties and complicated flow field near the interface. When gas phase becomes turbulent, interactions between the turbulent eddies and the interfacial structures and exchanges between the phases introduce additional complexities to the flow phenomena.

A popular theme throughout the study of turbulent particle-laden flows is the requirement to model and predict the detailed behavior of such flows and to investigate the physical insight of the phenomena involved. Regarding the limited scaling that can be realized in laboratory models, a reliable computational model, which should be thoroughly verified and validated through the availability of experimental data, is essential for the confident extrapolation to the scale of the actual multi-phase flow system.

One famous traditional approach to model particle transport is the Reynolds-averaged Navier-Stokes (RANS) equations. It is known that the accurate prediction of particle transport is strongly dependent on a realistic description of the time-dependent velocity field encountered along particle trajectories. But the RANS approach can not accurately predict the properties of the Eulerian turbulence field [6]. On the basis of the current availability of modern computational power and speed, direct numerical simulation (DNS) is becoming more possible to solve directly the transport equations governing the conservation of mass, momentum and energy for each of the phases and to compute every detail of the multi-phase flow, the motion of all the fluid around every particle and droplet, and the position of every interface. However, such comprehensive treatment is still restricted to low Reynolds number and a limited amount of particles and droplets. An alternative that is not restricted in the range of Reynolds number as DNS is large eddy simulation (LES). Although the LES approach has higher computational cost than RANS, it has the advantage that allows a more accurate and natural accounting of particle-turbulence interactions at an affordable numerical cost. The prediction of the small-scale velocity field in the LES computation depends on the statistical performance of a subgrid-scale (SGS) model that sometimes is undesirable for the particles of small inertial relaxation time scale.

Therefore, during the past four decades, scientists have explored for numerical methods of turbulent multiphase flow that can meet the following requirements of (1) simplicity and minimal empiricism; (2) high computational efficiency and low cost; (3) accurate description of relevant physics of interest; (4) wide range of flow applications. As a suitable alternative, one dimensional turbulence (ODT) model has been developed as a stochastic modeling approach that captures the full range of length and time scales, and thus the details of molecular mixing. ODT has been proven to be a successful model of many different kinds of shear-dominated nonreacting [7–9] and reacting flows [10–16].

This work is part of a large effort to develop a computationally efficient multiphase model compared with the current existing numerical methods. The model is able to capture enough of the relevant physics of turbulent multiphase flows, especially the fine scales of particle-turbulence interactions, and also to quantitatively predict particle behavior in different flow configurations of practical interest.

1.2 Scope of the work

This study aims at the development and validation of a computationally affordable model to investigate the dispersive transport of the particles in turbulent multiphase flows. Of specific focus is the detailed numerical description of particle-turbulence interactions in different flow configurations. As a pioneer exploration, Schmidt [17] came up with a novel idea to incorporate particle-turbulence interaction into the existing ODT single-phase model. He validated the approach in the nonreacting turbulent channel flow that is coupled with a representation of particles by a drag law with one-way coupling (only the fluid can affect the particles). Although some fundamental physics behind ODT multiphase model is still worthy of further exploration, his work gives the author the enlightenment to further develop the comprehensive ODT multiphase models in this dissertation.

The contribution of this work is summarized as follows:

- An instantaneous particle-turbulence interaction approach originally proposed by John Schmidt [17] is implemented in the current ODT turbulence model and validated in the simulation of particle dispersion in homogeneous decaying turbulence configuration. The fundamental understanding of ODT multiphase physics is given in detail.

- Two new particle-turbulence interaction approaches are developed and implemented in this work. One applies a continuous interaction mechanism, and the other combines the instantaneous and continuous features of particle-turbulence interaction. These two are validated in the simulation of particle dispersion in a turbulent jet flow. The distinction between different ODT multiphase approaches are demonstrated for future extension to other flow configurations.
- A mechanism of relative motion between the particle and turbulent eddies is built into continuous interaction approach. This allows more accurate predictions of particle behavior.
- The two-way momentum coupling mechanism is proposed and implemented in this work and validated in a turbulent particle-laden jet flow. This allows momentum transfer between the gas and particles in the ODT multiphase model.
- The ODT study of particle temperature in a hot ethylene jet flow is performed in wall-bounded configuration. The work in this particular configuration reveals much relevant physics of interest that is not studied elsewhere and has practical attractions for biomedical field.

1.3 Outline of the dissertation

The dissertation consists of the formulation and validation of new variants of the ODT multiphase model that are applied to different sets of turbulent particle-gas flow problems.

Chapter 2 provides the background information on common turbulence models, the category of particle-turbulence interaction, and particle behavior in different turbulent flow of interest.

Chapter 3 presents a comprehensive introduction of three ODT multiphase interaction models and illustrates the comparisons between them. That is, (1) instantaneous Type-I model, (2) continuous Type-C model, and (3) combined Type-IC model. Two-way momentum coupling mechanism and multiphase heat transfer are also presented.

Chapter 4 investigates particle dispersion using Type-I model in homogeneous decaying turbulence configurations. The model is validated by the comparison to experimental data of particle dispersion for a range of intrinsic particle time scales and body forces. Particle dispersion, velocity, and integral time scale results are presented. The work presented in this chapter has been published in *Physics of Fluid* [5].

Chapter 5 compares the simulations of particle-gas interactions using three models (Type-I, -C, and -IC) in the jet flow configuration. The flow statistics of the above models are validated by comparison to experimental measurements. The differences between the particle motions predicted by different models are discussed. The work presented in this chapter has been submitted to *Physics of Fluid* for review.

Chapter 6 applies two-way momentum coupling mechanism in Type-I model for a temporally developing turbulent particle-laden planar jet and compares the model prediction with experimental measurements. The turbulence modulation by particle addition is investigated, in which gas mean velocities, gas velocity variance modulated by particles, particle velocity, and particle distributions are presented. The study presented in this chapter is being prepared for publication.

Chapter 7 predicts particle temperature histories in the nonisothermal ethylene jet flow. The particle positions, particle temperature, and gas environment temperature felt by the particles are predicted by Type-I model for the particles of varying inertia and thermal relaxation time scale.

Chapter 8 presents the conclusions drawn from the present work as well as some recommendations proposed for future work to be done on the subject of ODT multiphase flows.

CHAPTER 2. BACKGROUND

This chapter first gives an overview to the most common turbulence models. Turbulent particle-laden flows of interest are then described, followed by the introduction of the ODT model adopted in the present work.

2.1 Turbulent models

The most important advances of computational techniques to investigate turbulence appeared in the 1970s and 80s. The first of these was large-eddy simulation (LES) as proposed by Deardorff [18] in 1970. This was rapidly followed by the first direct numerical simulation (DNS) by Orszag and Patterson [19] in 1972, and the introduction of a wide range of Reynolds-averaged Navier-Stokes (RANS) approaches beginning with Launder et al. [20, 21].

DNS [22] requires no modeling, and simply exploits numerical analysis to construct an efficient implementation of an appropriate Navier-Stokes solution procedure. No physical assumptions need be made beyond those already embodied in the Navier-Stokes equations themselves. However, because of the extremely wide range of length and time scales, reflected in the magnitude of the Reynolds number (Re), it is not yet possible to perform such calculations if Re is at all large. The total computational cost scales as Re^3 for DNS calculations. It is often pointed out that at the current rate of improvement in computing hardware, DNS is hardly acceptable from a practical standpoint in commercial applications.

Due to high computational cost, DNS in particle-laden modeling is limited to small-scale (low Re), canonical turbulent flows with dilute dispersed phase [23, 24]. DNS is a standard numerical measurement to which other turbulence models can be compared, particularly in multiphase flows [25, 26]. Because the data of those flows are too hard to get from direct measurements, or the multi-physics effects involved are so complicated that one cannot see if the results are the measures of certain desired phenomenon.

RANS [27, 28] is a good alternative to DNS, even recently. The Reynolds decomposition of $U(x,t)$ is

$$U(x,t) = \bar{U}(x) + U^{'}(x,t),$$

where $\overline{U}(x)$ is the time-averaged velocity and $U^{'}(x,t)$ is the fluctuating velocity. In RANS, the information about turbulent fluctuations is contained in the time averaged Reynolds stresses of the form $\overline{U_iU_j}$. These are obtained as an outcome of a turbulence model that links Reynolds stresses to mean flow quantities (e.g., $k-\varepsilon$ model), or solves modeled transport equations for each Reynolds stress component. In these models, computational cost is nearly independent of Re, and, in fact, many of such methods work well at very high Re. However, it is difficult for RANS to model some flows, e.g., recirculating, and near-wall flows, since there is no turbulence closure model adequate for all the flow configurations.

Any particle-laden RANS simulations would be starting with average particle velocities [29]. However, accurate prediction of particle transport is strongly dependent upon providing a realistic description of the time-dependent, three dimensional velocity field encountered along particle trajectories [30]. Thus, the deficiencies in the prediction of turbulence field will in turn adversely impact prediction of dispersed phase transport. In order to overcome this, additional modeling is required for RANS applications of multiphase flows to describe individual particle behavior [4].

LES [31] involves a spatial filtering operation, a temporal filtering operation, or both. The LES decomposition is given by

$$\begin{aligned} U(x,t) &= \widetilde{U}(x,t) + U^{'}(x,t), \\ \widetilde{U}(x,t) &= \iint U\left(r,t^{'}\right) G\left(x-r,t-t^{'}\right) dt^{'} dr, \end{aligned}$$

where G is the kernel of the filter, $\tilde{U}$ is termed the resolved-scale velocity, $U^{'}$ is termed the subgrid-scale or unresolved velocity component, and r is distance difference. LES requires modeling of part of the inertial subrange and dissipation scales. The amount of required modeling is set by the amount of resolution that can be afforded, and the total computational cost will scale around Re^2. LES solves the large flow scales like DNS, but models the effect of the small scales with a subgrid-scale (SGS) model. LES is largely a research tool but was also being applied to some industrial applications, and hence be seen as an intermediate between RANS and DNS [32].

LES is very attractive method available for particle-laden multiphase turbulent flows since it provides the optimum means of capturing the unsteady physical features in the flows. The accuracy and the reliability of LES predictions are, however, dependent on several factors such as the accurate modeling of the SGS phase interactions and the correct representation of the initial/boundary conditions for all phases [33, 34]. The importance of the SGS closure needs to be emphasized, because using a filtered velocity field alone to advance the particles can lead to serious inaccuracies [35]. Meanwhile, gross errors in the prediction of the particle drag force may result from the negligence of the SGS velocity fluctuation in LES [36].

2.2 Particle transport in turbulent flow

2.2.1 Fluid reference frame and fluid-particle interaction categories

The simulations of particle dispersion can be classified based on the type of fluid reference frame, Eulerian or Lagrangian [37]. In Eulerian models, the reference frame is stationary, and defined in terms of spatial location and time. These models treat the particles as a continuum phase similar to the fluid phase, which is often popular when the particle loading is high, e.g., in the fluidized-bed combustion systems. In the Lagrangian reference frame, individual particles are tracked when they pass through fixed differential control volumes. The instantaneous positions of the particles can be considered as a function of the location from where the particle originated and the time elapsed. The Lagrangian frame is a natural way to treat particles as a discrete phase in dilute flows.

Particle interactions and concentrations are important factors to account for in particle dispersion studies [17, 38, 39]. When the addition of the particles is at low volume fraction, the assumption is made that the properties of the turbulent flow field are not modified by the presence of the particle cloud. Such dilute particle-laden flows are governed predominantly by the surface interaction and body forces acting on the particles. This is termed as one-way coupling. Otherwise, problems of turbulence modification by particles arise when particles are present in large enough concentrations such that the loss or gain of momentum and energy to the turbulence provided by the particles is no longer negligible, that is, two-way coupling. The current study mainly focuses on momentum transfer between the particle and gas phase in the application of two-way coupling. A four-way coupling formulation arises when both the particle-particle and particle-fluid interactions are included. In the sufficiently dense particle-laden flows, the collisions between the particles significantly alter the movement of the particles in the gas phase.

2.2.2 Particle behavior in homogeneous isotropic turbulence

Turbulent flows are referred to as homogeneous and isotropic when it is assumed that (1) statistical properties remain invariant with the change of position, which implies, for example, that $\overline{U'^2}(x) = \overline{U'^2}(x+r)$ for any possible vector r within the domain of flow field; (2) rotation and reflection are not important and can be neglected which implies that, $\overline{U'^2} = \overline{V'^2} = \overline{W'^2}$ throughout the flow field.

In these flows, the dispersion of particles in turbulent flows has received a lot of theoretical and experimental attention. The Lagrangian time scale of the fluid velocity seen by a particle, t_e, or interaction time, is the most important parameter determining the eddy-particle interaction time and thus the diffusivity of the particles. During the interaction, a particle may or may not remain trapped inside an eddy for the eddy lifetime. This phenomenon is called the crossing trajectories effect in the literature. Theoretical investigations made by Yudine [40] and Csanady [41] demonstrated the crossing trajectories effect for particles settling under gravity and proposed expressions for t_e. Hinze [42] attempted to describe particle dispersion, and assumed t_e to be the same as the Lagrangian time scale of fluid t_L, thus leading to the result that the diffusivity of the particles is equal to that of fluid particles. Reeks [43] found that t_e may initially decrease with increasing particle relaxation time though it eventually rises and approaches the particle relaxation time. Squires and Eaton [44] performed DNS of particle-laden isotropic turbulence, but did not recognize the role of t_e in the dispersion of the particles. Wang and Stock [45] and Pozorski and Minier [46] noticed the importance of the deviation of t_e from t_L and suggested approximate forms for t_e. He et al. [47] and Jung et al. [48] provided t_e as a function of the Stokes number in their DNS of particle-laden isotropic turbulence.

Another phenomenon of great interest is the inertia effect, that is, the reduction of root mean square (RMS) fluctuation of particle velocities. Maxey and Riley [49] studied small spherical particles subject to a Stokes drag force in a two-dimensional incompressible, steady, periodic flow field with a single length scale, and in homogeneous turbulence generated by random Fourier modes with a limited range of scales. Their work had shown that the inertia effect of particles produces a bias in the particle trajectories. The particles were found to tend to accumulate along isolated paths. This preferential accumulation has been confirmed by the results of full direct numerical simulation developed by Squires and Eaton [44]. Fung et al. [50] studied the average settling velocity of a small spherical particles under gravity through a Gaussian random velocity field generated by a von Karman energy spectrum. The particles were subjected to the effects of linear or nonlinear drag forces, inertia, and gravity. It was shown that the effect of drag nonlinearity is a function of the particle to fluid density ratio ρ_p/ρ and of the ratio of particle relaxation time to the Kolmogorov timescale of the fluid τ_p/τ_k.

Almost all experimental studies use grids in wind tunnels that have a large mean velocity to create nearly homogeneous isotropic turbulence conditions [2,3]. Snyder and Lumley [2] used ten cameras placed successively in a vertical tunnel to observe that as the particle relaxation time increases, its diffusion timescale and consequently its diffusion coefficient decreases. Wells and Stock [3] investigated the particle motions in a horizontal tunnel, where the body force of the particles can be altered by an electric field. They were thus able to isolate the inertia effect and settling velocity, which gives rise to the crossing trajectory effect. There are a few computations of turbulent diffusion to simulate these experiments, e.g., Squires and Eaton [44], Yeh and Lei [51], Lu [52], Pozorski and Minier [46], Lightstone and Raithby [53], Hennick and Lightstone [54], Reynolds and Lacono [55], among others.

2.2.3 Particle behavior in turbulent jet

In a round jet, the fluid steadily flows through the nozzle of diameter d to produce a flat-topped velocity profile. The jet from the nozzle flows into an ambient fluid. The flow is statistically stationary and axisymmetric. Hence, statistics depends on the axial and radial coordinates x and r, and are independent of the time and the circumferential coordinate θ.

Experimental and numerical studies of particle-laden round jets have been reported in the past. The pioneering researchers, Yuu et al. [34,56,57] performed a series of studies on gas-particle turbulent round jets. Yuu et al. [57] conducted DNS to simulate gas and particle motions at a low

Reynolds number ($Re = 1700$). Turbulence characteristics (air and particle mean velocity, turbulent intensity, Reynolds stress and auto-correlation) had good agreement with their experimental data. Their latter work investigated the effect of particles on the subgrid-scale turbulence using LES of a round jet with $Re = 10^4$. They found that the particles reduce the subgrid-scale turbulence when the particle size is smaller than the grid size. When the product of the gas-particle relative velocity and particle concentration gradient is large, the particles increase the subgrid-scale turbulence. Chung and Troutt [58] numerically investigated the particle dispersion in an axisymmetric jet by the vortex method. They proposed that particle dynamics in the near field of a round jet are controlled by large-scale structures and particle dispersion depended strongly on the Stokes number, which is in agreement with experimental results of Longmire and Eaton [59]. Sbrizzai et al. [60] used LES to simulate a confined turbulent round jet. For particles characterized by $St < 1$, they found that particle clustering occurred not only by the action of azimuthal vorticity, but also the action of the streamwise vorticity field was important. Hansell et al. [61] used the vortex dynamics method for the calculation of turbulent round jet with vaporizing particles of varying sizes and pressure. They reported that the three-dimensional simulation did not show significantly different behaviors of particle dispersion from the axisymmetric code under the thin vortex assumption. They further demonstrated that the dispersion of particles simulated by the full equation was underestimated typically by 25% by the simple approximation of only the drag force employed in the particle equation, and the errors increased with increasing particle size.

The variations of particle properties, such as particle size and particle material density, particle mass loading ratios, and flow parameters, can lead a turbulence modulation in different ways [62–64]. The studies compared the turbulence intensities modulated by the particle-laden jets with those in particle-free turbulent jets. They found that the gas turbulence intensities decrease in the two-phase jets. The measurements of Tsuji et al. [65] demonstrated that the magnitude of particle effects on the gas flow is less with large particles than with small particles with the same loading ratio, and a delay in the decrease of the centerline air velocity and a reduction in the jet width are observed. Sheen et al. [66] used polystyrene particles of different sizes and mass loading ratios in their experiments and found that the axial gas-phase turbulence intensities of two-phase flow are higher than those of single-phase flows in the near-fields, while they are always lower in the far-fields. Modarress et al. [67] stated that the presence of particles reduces both the gas-phase fluctuating velocity and the Reynolds shear stress, and the reduction is proportional to the particle mass loading ratio in a two-phase round jet. The physics of turbulence modulations by particles have been investigated by the researchers [68–70]. It is thought that the reduction of turbulent intensities in two-phase flows is mainly induced by turbulence energy transfers from eddies to particles while the increase of turbulent intensities is mostly by infused energy from particle wakes to background turbulence. Some other physical mechanisms, such as the dissipation model and velocity gradient model, were also proposed by Yarin and Hetsroni [71], and Kenning and Crowe [70], respectively. Although these physical models are able to describe the effects of particles on the turbulence modulation, they are still not fully validated.

2.3 One dimensional turbulence model

The one-dimensional turbulence (ODT) model, developed by Kerstein [7] in 1999, simulates the evolution of fluid velocity and properties along a one-dimensional line of sight through a three-dimensional turbulent flow by completely resolving the full range of length scales and the finest time scales along this line. ODT was developed as an outgrowth of the linear-eddy model (LEM). In both of the models, turbulent stirring and molecular diffusion are treated separately. Different from other common turbulent models introduced in Sec. 2.1, turbulent advection is described by stochastic process rather than using an equation of transport evolution. In LEM, the time and length scales of eddies are sampled randomly from a predefined eddy distribution function. There is no provision for feedback of local flow properties to the random process governing subsequent events [7]. In contrast, the ODT model has the advantage to capture this feedback in that the formulation of the eddy distribution function is not predetermined and can reflect the local kinetic energy production mechanisms.

There are two different formulations of ODT. The temporal formulation manipulates the time evolution of fluid velocities and properties on the 1-D domain with the domain being treated as a closed system. The spatial formulation casts in a form that obeys the spatially developing flow conservation laws. The domain in this form evolves in the streamwise direction, and each realization of the spatial formulation can be interpreted as an instantaneous snapshot of the flow. In either formulation of ODT, the diffusive advancement uses a Lagrangian control volume formulation in such a way that the total mass flux is constant and the momentum is conserved in any given cell.

The turbulent advection is incorporated through instantaneous mapping rearrangement events and kernel transformations along the 1-D domain. The triplet mapping event imitates the rotational folding features of the eddy in a turbulent flow field. This procedure takes a line segment, shrinks it to a third of its original length, and places three copies of it on the original domain. The middle copy is reversed to ensure that properties remain continuous. The kernel transformation is included to describe the energy transfers between the velocity components.

The distinguishing features of ODT are its scope, simplicity, minimal empiricism, and capability to incorporate complex molecular processes (variable transport properties, chemical reactions, etc.) without introducing additional approximations [7]. The simplified low dimensional formulation of the ODT model makes itself computationally affordable and applies to problems of practical interest. The ODT model implemented for this work resolves full range of length and time scales of multiphase flows along the 1-D domain with detailed particle transport, flow modulation and particle-fluid interaction. More details of the ODT model used for the current study are given in the subsequent chapters.

CHAPTER 3. COMPUTATIONAL METHODOLOGY AND APPROACH

One-dimensional turbulence (ODT) is a numerical method to generate realizations of stochastic problems on a one-dimensional domain [7]. ODT is applied in flow configurations such as homogeneous turbulent flow, shear-driven flow (channels, jets), and buoyancy-driven flow (plumes), etc. The one-dimensional domain is formulated in the direction of primary gradients and the governing equations of mass, momentum, energy, and species are solved in the conservation form. We refer to the ODT-aligned direction as the y coordinate, and the streamwise direction as the x coordinate. The Cartesian coordination system is used in this project, which is consistent with most ODT applications. However, the model has been extended to cylindrical coordinate as well [13], where the ODT line aligns in the radial direction, and the axial velocity component represents the direction of turbulent stress. ODT has been proven to be a successful model of many different kinds of shear-dominated nonreacting [7–9] and reacting flows [10–16]. But until now there are only limited studies that extend ODT model to the multiphase [4,72]. In this chapter, a comprehensive introduction of various ODT multiphase interaction models is presented, and the comparisons between them are illustrated. The author hopes to establish a physically sound basis for the various ODT multiphase implementations that allow a clear distinction in comparing different approaches and will also provide more useful details of model implementation in future applications.

The remainder of this chapter is organized as follows: Sec. 3.1 summarizes the governing equations solved and important modeling concepts including the triplet map transformation and eddy selection, etc., which exist in the literature and are used in the current implementation of the ODT model. Sec. 3.2 introduces the formulations of three different particle-turbulence interaction models, and illustrates the differences between them. Two-way momentum coupling, as one of the important concepts in the multiphase field, is addressed in Sec. 3.2. Sec. 3.3 presents heat transfer between the particles and gas phase.

3.1 Governing equations for ODT

The ODT model consists of two main mechanisms : diffusive advancement and eddy events. The diffusive evolution on the 1D domain is governed by truncated transport equations (described below) that omit the nonlinear advective terms, which are modeled by the eddy events. These diffusive equations dissipate velocity fluctuations and kinetic energy, though this process is only significant at diffusive scales, and the eddy events model the cascade of fluctuations to the dissipative scales. The three-dimensional advection involves a vortex-stretching process that transfers the fluctuations to higher wave numbers and is costly to predict. To describe the turbulent advective terms, ODT introduces the concept of the so-called "triplet map" that transfers fluctuations to higher wave numbers during eddy events. The rate of this transfer by eddy events is determined through a stochastic sampling of the evolving velocity field through a measure of the shear energy that is a function of the location on the domain and the eddy length scale (wavenumber). There are two approaches to evolve the ODT domain: (1) temporal ODT is evolved on the (y,t) plane, and (2) spatial ODT is evolved on the (y,x) plane. Even in predicting spatially developing flows, most ODT simulations have been conducted using temporal evolution assuming a Lagrangian evolution of the flow domain to map results to the spatial evolution [11]. A thorough description of the ODT model formulation used in this work is provided in [16]. The interested reader could refer to it for details.

3.1.1 Diffusive advancement

Temporal formulation

In the Lagrangian frame of reference, choosing (t,y) as independent variables, the governing equations are derived from the Reynolds transport theorem and advanced in time along the ODT line [16]. Since there is no mass source term, no non-convection flux and uniform properties inside the grid control volumes in one dimension, the continuity equation is given by

$$\frac{d}{dt}\int \rho dy = 0. \tag{3.1}$$

A discretized equation applied on the grid cells for the above continuity equation is

$$\rho \triangle y = constant, \tag{3.2}$$

where the density ρ is calculated from an equation of state and is constant if the flow is nonreacting. The diffusive advancement evolves scalar equations of momentum, species and energy using a conservative finite volume method written here for a given cell:

$$\frac{dU}{dt} = -\frac{1}{\rho \triangle y}(\tau_{x,e} - \tau_{x,w}) + \frac{S_{p,u}}{\rho \triangle y}, \tag{3.3}$$

$$\frac{dV}{dt} = -\frac{1}{\rho \triangle y}(\tau_{y,e} - \tau_{y,w}) - \frac{1}{\rho}\frac{dP}{dx} + \frac{S_{p,v}}{\rho \triangle y}, \tag{3.4}$$

$$\frac{dW}{dt} = -\frac{1}{\rho \triangle y}(\tau_{z,e} - \tau_{z,w}) + \frac{S_{p,w}}{\rho \triangle y}, \tag{3.5}$$

$$\frac{dY_k}{dt} = -\frac{1}{\rho \triangle y}(j_e - j_w) + \dot{m}_k''', \tag{3.6}$$

$$\frac{dh}{dt} = -\frac{1}{\rho \triangle y}(q_e - q_w) + \frac{1}{\rho}\frac{dP}{dt}. \tag{3.7}$$

In these equations, x is the streamwise direction, y is the ODT-aligned direction and z is the spanwise direction. U, V, and W are the velocities in the streamwise, ODT-aligned, and spanwise directions, respectively. Y is mass fraction of chemical species. h is local ethalpy. τ is the viscous stress, j is the mass diffusion flux, $\dot{m}_k'''$ is a reaction source term and q is the heat flux. The subscripts e and w represent east and west faces of control volumes. P is the pressure. $S_{p,u}$, $S_{p,v}$, and $S_{p,w}$ are the gas-phase momentum source terms obtained from the particles in three directions for two-way coupling, respectively, or are negligible when there is no turbulent modulation induced by particles (one-way coupling). The subscript k refers to the species k. The stress tensors of three velocity components are represented as

$$\tau_i = -\mu \frac{dU_i}{dy}, \tag{3.8}$$

where μ is dynamic viscosity and i represents the direction component. Fick's law is used to define the diffusion flux of the species k,

$$j_k = -\frac{\rho Y_k D_{d,k}}{X_k}\frac{dX_k}{dy} = -\rho D_{d,k}\frac{dY_k}{dy} - \frac{\rho D_{d,k} Y_k}{M_w}\frac{dM_w}{dy}, \tag{3.9}$$

where M_w is the mean molecular weight, and $D_{d,k}$ and X_k are the diffusion coefficient and mole fraction, respectively. The general vector form of heat flux due to conduction, species diffusion flux and radiation flux is given by

$$q = -\lambda\frac{dT}{dx} + \sum_k h_k j_k + q_{rad}, \tag{3.10}$$

where λ is thermal conductivity, h_k is the species enthalpy, q_{rad} is the radiative flux, and T is the temperature.

Spatial formulation

Unlike the temporal formulation, the spatial formulation models turbulent flows that are two-dimensional in nature. The diffusive-reactive system is advanced as if the flow were steady, but instantaneous rearrangements occur due to the eddy events. The spatial evolution applies basic boundary layer assumptions and is parabolic in nature, in which a marching method is used. The constraint for continuity across the Lagrangian grid is constant mass flux $\rho U \triangle x = constant$, unlike constant mass $\rho \triangle x = constant$ in temporal evolution. The governing equations of momentum, species and energy are given by

$$\frac{dU}{dx} = -\frac{1}{\rho U \triangle y}\left(\tau_{x,e} - \tau_{x,w}\right), \tag{3.11}$$

$$\frac{dV}{dx} = -\frac{1}{\rho U \triangle y}\left(\tau_{y,e} - \tau_{y,w}\right) - \frac{1}{\rho U}\frac{\partial P}{\partial x}, \tag{3.12}$$

$$\frac{dW}{dx} = -\frac{1}{\rho U \triangle y}\left(\tau_{z,e} - \tau_{z,w}\right), \tag{3.13}$$

$$\frac{dY_k}{dx} = -\frac{1}{\rho U}\left(j_e - j_w\right) + \frac{\dot{m}_k'''}{U}, \tag{3.14}$$

$$\frac{dh}{dx} = -\frac{1}{\rho U \triangle y}\left(q_e - q_w\right) + \frac{1}{\rho U}\frac{dP}{dt}. \tag{3.15}$$

3.1.2 Eddy events

Triplet map transformation

Turbulence is characterized by a three-dimensional vortex stretching process that is modeled in ODT through a representative sequence of eddy events as introduced at the beginning of this section. This model has two key components, the triplet-map representation of the length-scale cascade and the model for the rate of triplet maps. Turbulent eddies are sampled randomly from the domain as a function of the eddy location, represented by its left bound, y_0, and by its length, l, with the triplet map occurring over the region $[y_0, y_0 + l]$ for the given sample. The triplet map spatially compresses the fluid property profiles within $[y_0, y_0 + l]$ by a factor of three. The original profiles are replaced with three copies of the compressed profiles, with the middle copy spatially inverted. This mapping is described by

$$f(y) = y_0 + \begin{cases} 3\left(y - y_0\right) & \text{if } y_0 \leq y \leq y_0 + 1/3l, \\ 2l - 3\left(y - y_0\right) & \text{if } y_0 + 1/3l \leq y \leq y_0 + 2/3l, \\ 3\left(y - y_0\right) - 2l & \text{if } y_0 + 2/3l \leq y \leq y_0 + l, \\ y - y_0 & \text{otherwise.} \end{cases} \tag{3.16}$$

where $f(y)$ and y are the original fluid location and the post-triplet-map location, respectively. The fluid outside $[y_0, y_0 + l]$ is unaffected.

The triplet map is measure preserving and all integral properties (e.g., mass, momentum, and energy) or moments thereof are constant during a triplet map. Specifically, the kinetic energy is conserved, which is a desirable property because eddy events physically model the inviscid advection process. During the triplet map, kernel transformations are introduced that redistribute energy among the velocity components [73]. The transformations are meant to model the velocity randomization and so-called return to isotropy effect in turbulent flows. The kernel can be considered as a wave function that adds or subtracts energy from the eddy based on the amplitude of the wave. An eddy event maps the velocity component i as follows:

$$U_i(y) \longrightarrow U_i(f(y)) + c_i K(y), \tag{3.17}$$

where the kernel $K(y) \equiv y - f(y)$ is the displacement induced by the triplet map and can be integrated to zero over the eddy interval. c_i is kernel coefficient of $K(y)$. However, this form merely obeys the conservation condition for the case of constant density. To ensure momentum conservation during an eddy event with variable density, the additional kernel donated as $J(y) = |K(y)|$ is introduced into the formulation [9]:

$$U_i(y) \longrightarrow U_i(f(y)) + c_i K(y) + b_i J(y), \tag{3.18}$$

where b_i is kernel coefficient of $J(y)$.

Eddy selection

The procedure to sample and accept an eddy follows that described in [16]. The rate density (per location and per eddy length) for eddy occurrence at location y_0 and length l is denoted $\lambda_e(y_0, l, t)$ and is dimensionally $\tau_e^{-1} l^{-2}$ where τ_e is an eddy time scale given in Eq. 3.22. The eddies are sampled from a presumed distribution

$$P_0(y_0, l) = g(y_0) f(l). \tag{3.19}$$

The eddy location distribution, $g(y_0)$, is taken to be uniform over the domain while the eddy size distribution is assumed to be

$$f(l) = A_l \exp(-2\tilde{l}/l), \tag{3.20}$$

where $\tilde{l}$ is the most probable eddy size and A_l is the PDF normalization constant. The eddies are sampled from the distributions $g(y_0)$ and $f(l)$ in a Bernoulli trial with a sampling period of Δt_s, and the eddy time scale τ_e is computed as described below. Given this sampled eddy, the acceptance probability for the eddy is

$$P_a = \frac{\lambda_e(y_0,l,t)\Delta t_s}{P_0(y_0,l)} = \frac{\Delta t_s}{\tau_e l^2 f(l) g(y_0)}. \tag{3.21}$$

Sampled eddies are accepted if a trial random number is less than the acceptance probability. For sufficient statistical sampling, it is important that Δt_s is small enough so that $P_a \ll 1$ for all sampled eddies, and the algorithm ensures this.

The eddy time scale τ_e is obtained using a measure of the available energy at wavelength l. In the present work (without buoyant or other forms of energy), τ_e is computed using scaling arguments to relate to the available kinetic energy, which is given by $E_{kin} = \rho\left(U_K^2 + V_K^2 + W_K^2\right)$,

$$\frac{1}{\tau_e} = C\sqrt{\frac{2}{\rho l^2}\left(E_{kin} - ZE_{vp}\right)}, \tag{3.22}$$

where ρ is constant density for nonreacting cases. In the reacting flows with variable density, additional contributions are present [9]. To obtain E_{kin} the velocities are integrated across the kernel function $K(y)$ as

$$U_K = \frac{1}{l^2}\int_{y_0}^{y_0+1} U(f(y))K(y)dy. \tag{3.23}$$

In Eq. 3.22, E_{vp} is included as a viscous penalty to restrict unphysically small eddies, which is defined below,

$$E_{vp} = \rho\nu/l. \tag{3.24}$$

where ν is kinematic viscosity of the fluid.

Beyond the basic elements of Eq. 3.23 as a measure of velocity fluctuations, the form of Eq. 3.23 is not fixed, and other forms have been used [7]. This leads to the introduction of C, a constant of proportionality between the kinetic energy formed from Eq. 3.23 and the eddy time scale in Eq. 3.22, that directly scales the probability of an eddy occurring as per Eq. 3.21. Similarly, a constant of proportionality, Z, is introduced for the viscous energy dissipation factor, E_{vp}. C plays an important role in the rate for the turbulent cascade, and flow evolution is sensitive to it. Z is provided more as a numerical expedient to reduce the occurrence of sub-Kolmogorov scale eddies; these small eddies affect transport less than the viscous evolution in Eq. 3.13-3.15. A maximum value of Z will exist above which there will be an unphysical buildup of fluctuations above the Kolmogorov scale that is visible in spectra (not shown here).

Eddy events may result in the occurrence of unphysically large eddies that adversely affect the overall mixing. There are several mechanisms of large eddy suppression that have been developed [8, 9, 11, 12]. The method favored for jet flows is an elapsed time method in which the eddy time scale τ_e can be compared with the simulation elapsed time t; eddy events are allowed only when $t \geq \beta\tau_e$, where β is a model parameter.

3.2 Lagrangian formulation for particles

The velocity and trajectory of particles are described by a Lagrangian approach in this study. Like the ODT treatment of the continuous fluid phase, the action of turbulent eddies is handled in a special manner, referred to here as the particle-eddy interaction (PEI), as compared with diffusive processes characterized by the standard approaches described in Sec. 3.2.1. The triplet map is implemented as an instantaneous process, and the action of the triplet map on the particle can be treated either as an instantaneous process or continuous process as observed in the flow evolution coordinate. The motion of the particles is traced as they interact with a random succession of turbulent eddy motions, each of which represents a Type-I (referred to as "instantaneous") or Type-C (referred to as "continuous") or Type-IC (referred to as "instantaneous and continuous") interaction between the particle and triplet map. In the Type-I model, the PEI is represented as an instantaneous change of the particle position and velocity in the same manner that the triplet-map itself is an instantaneous event. In the Type-C model, the PEI occurs during the flow evolution by mapping the equivalent triplet-map space-time influence to the flow evolution. In the Type-IC model, the particles undergo the Type-I PEI when they are in the eddy region at the time of the eddy occurrence, and experience the Type-C PEI if they are initially outside the eddy, but move into the eddy region during the flow evolution. Mean dispersive transport properties of particles are obtained by averaging over a statistically significant number of particle trajectories. Schmidt proposed several particle models that are similar in nature to the ones here and implemented one (Type-I) to study particle behavior in a different context [4, 26]. A version of the Type-C model was used by Punati [72]. In this section, we summarize the implementation of the models, and more importantly, discuss and compare different types of PEI.

A particle-eddy interaction occurs when both the particle and the triplet map occupy the same space-time. To predict the interaction, a finite temporal interval and spatially cubic region, consistent with turbulence isotropy, is assumed for each eddy based on the eddy time and length scale, τ_e and l. This spatial-temporal region is referred to as the eddy "box". Within the eddy box, the particle evolves in the x, y and z dimensions as described in the following subsection, and the PEI ends when the particle leaves the idealized eddy box or when the eddy lifetime has passed. The eddy lifetime,

$$t_e = \beta_p \tau_e \left(y, l; t\right), \tag{3.25}$$

is related to the eddy time scale, $\tau_e(y, l; t)$, which represents the rate of eddy occurrence, but these quantities should not be expected to be equal; the proportionality between these times is represented by the parameter β_p.

In many flows, the particles typically leave the box at the end of the eddy lifetime, t_e, but if there is significant relative motion between particles and eddies, the particles will depart spatially. This latter spatial crossing of the eddy boundary is referred to in the literature as the crossing trajectory effect [41]. This use of an eddy length and lifetime to predict the eddy influence on the particles is common to the stochastic approaches. In the ODT model, the fluid evolution results in a full spectrum of eddy scales as opposed to only predicting integral scale eddies. The selection of the eddy lifetime in the ODT formulation is equivalent to the selection of t_e, and a proportionality appears there between the integral turbulent time scale evaluated from, for example, the turbulent kinetic energy and its dissipation rate. In approaches we will refer to as discontinuous random walk an eddy velocity fluctuation is selected to act for an eddy lifetime [56, 74, 75]. Another class of models referred to as continuous random walk approaches sampled fluctuating velocity increments [30, 76, 77].

3.2.1 Governing equations

The particle trajectory can be determined by solving its equation of motion. The full expression for the motion of a spherical particle that accounts for all the types of forces is given below [1,37],

$$
\begin{aligned}
m_p \frac{U_{p,i}}{dt} = & \underbrace{3\pi\mu d_p f\left(U_{g,i} - U_{p,i}\right)}_{\text{steady-state drag force}} + \underbrace{m_p g_i}_{\text{body force-gravity}} \\
& \underbrace{+ K_B d_p^2 \sqrt{\pi\rho\mu} \int_{t_0}^{t} \frac{\frac{d}{dt}\left(U_{g,i} - U_{p,i}\right)}{\sqrt{t - t'}} dt'}_{\text{Bassett force}} \\
& \underbrace{+ K_m \rho_p \frac{\pi}{6} d_p^3 \frac{d}{dt}\left(U_{g,i} - U_{p,i}\right)}_{\text{virtual mass force}} \\
& \underbrace{+ \frac{\pi}{8} \rho d_p^3 \omega_p \varepsilon_{ijk} n_{1,j} \left(U_{g,k} - U_{p,k}\right)}_{\text{Magnus force}} \\
& \underbrace{+ 1.61 \sqrt{\mu\rho} d_p^2 \gamma_{ijk} \left(U_{g,j} - U_{p,j}\right) n_{2,k} \sqrt{U_{g,i}}}_{\text{Saffman force}} \\
& \underbrace{- \rho \frac{\pi}{6} d_p^3 g_i,}_{\text{buoyancy}}
\end{aligned}
\tag{3.26}
$$

where m_p, ρ_p, d_p, ω_p and g are the mass, density, diameter, angular velocity and gravitational acceleration of the particle, respectively. U_g, μ and ρ are the velocity, viscosity and density of the fluid, respectively. The subscripts i, j, and k represent the scalar components in the x, y, and z directions. $n_{1,j}$ is a unit vector in the j direction of the particle angular momentum vector for Magnus force. $n_{2,k}$ is a unit vector in the direction of the gradient of gas phase in the k direction component. The third-order tensors ε_{ijk} and γ_{ijk} are defined as,

$$
\varepsilon_{ijk} \equiv \begin{cases} 1 & \text{for } ijk = 123,\ 231, \text{ or } 312 \\ -1 & \text{for } ijk = 132,\ 213, \text{ or } 321 \\ 0 & \text{otherwise} \end{cases}
\tag{3.27}
$$

and

$$
\gamma_{ijk} \equiv \begin{cases} 1 & \text{for } ijk = 123,\ 231,\ 312,\ \ldots \text{ (non-repeated indices)} \\ 0 & \text{for } ijk = 121,\ 322,\ 221,\ \ldots \text{ (repeated indices).} \end{cases}
\tag{3.28}
$$

Table 3.1: Contribution of different forces in the equation of particle motion (Eq. 3.26) [1].

Force	Relative contribution
Steady state drag force	0.93
Body force-gravity	0.05
Bassett force	0.001
Virtual mass force	0.01
Magnus force	< 0.0001
Saffman force	< 0.0001
Buoyancy	0.001

Table 3.1 compares the inertial contribution of different forces in Eq. 3.26 [1]. The steady-state drag force due to viscous drag contributes to over 90% of the inertial force, which is linear with the relative velocity between the gas phase and particle. Particle gravity has the second largest contribution to the inertial force. The Bassett force accounts for unsteady drag force due to particle acceleration with respect to the fluid that involves an empirical constant K_B of the order 6. It only contributes about 0.1% of total inertial force and can be neglected as the flow approaches steady state. The virtual mass force results from the difference in the acceleration between the fluid and the particle and has an overall contribution of less than 1%. The Magnus force results when a rotating particle is subjected to a nonrotating fluid, and can be ignored as it contributes less than 0.1% of the total inertial force. The Saffman force is a lift force of particles caused by the velocity gradient and is entirely negligible for most applications because it has an estimated $10^{-6}\%$ contribution to the total inertial force. The buoyancy is not considered in this work because the ratio of the material density of particle to fluid is high: 200-2000. The fluid is a dilute two-phase flow here so that the interaction between particles is neglected.

Under the above conditions, the particle momentum equation can be greatly simplified in which all other forces are negligible other than the drag force and the gravity. In the Lagrangian framework, the simplified momentum equation of a single spherical particle can be written in the form of

$$\frac{dU_{p,i}}{dt} = -\frac{U_{p,i} - U_{g,i}}{\tau_p} f + g_i, \tag{3.29}$$

The response time τ_p of a particle with mass m_p and density ρ_p in the fluid of viscosity μ is based on Stokes flow, given by

$$\tau_p = \frac{m_p C_c}{3\pi d_p \mu}. \tag{3.30}$$

Clift et al. [78] suggested that for particle slip-velocity Reynolds number $Re_p < 200$, which is true for most practical dilute flow systems, the nonlinear correction factor f needs to be added,

$$f = 1 + 0.15 Re_p^{0.687}, \tag{3.31}$$

where $Re_p = \rho \left| \overrightarrow{V_p} - \overrightarrow{V_g} \right| d_p/\mu$. Also the Cunningham slip factor C_c with mean free path of fluid λ_g is

$$C_c = 1 + \frac{\lambda_g}{r_p} \left[1.257 + 0.4 \exp\left(-1.1 \frac{r_p}{\lambda_g} \right) \right]. \tag{3.32}$$

In the two-way coupled implementation, the momentum coupling term of the fluid evolution introduced by the particles for a given i component is defined as

$$S_{p,i} = -\sum_n m_{p,n} N_p \frac{dU_{p,n,i}}{dt} = -\sum_n m_{p,n} N_p \left(\frac{U_{gi} - U_{p,n,i}}{\tau_{p,n}} f_n + g_i \right), \tag{3.33}$$

where the subscript n represents the particle n that introduces momentum change of gas phase. To decrease computational cost and make the simulation efficient, a computational-effect particle representation is applied in the simulations with high particle loading in which two-way coupling is included. Each particle in these ODT simulations is a pseudo particle that is used to represent certain number of "real" particles with identical properties. That is, each representative particle stands for N_p "real" particles. N_p has the unit of $\frac{\#}{m^2}$ in the one dimensional domain.

There are two important limits of particle inertia considered in the two-phase flow model. Small particles with vanishing Stokes number (zero τ_p) are termed tracer particles. Tracer particles always follow the fluid around them in the process of both diffusion and eddy events, and, therefore, their velocities in the x, y and z directions are equal to fluid velocities. On the contrary, large particles with infinite Stokes number (huge τ_p) are termed ballistic particles, and the fluid does not influence them. Particles between these limits are termed inertial particles. Figure 3.1 shows a schematic of the trajectories of tracer and ballistic particles during eddy events.

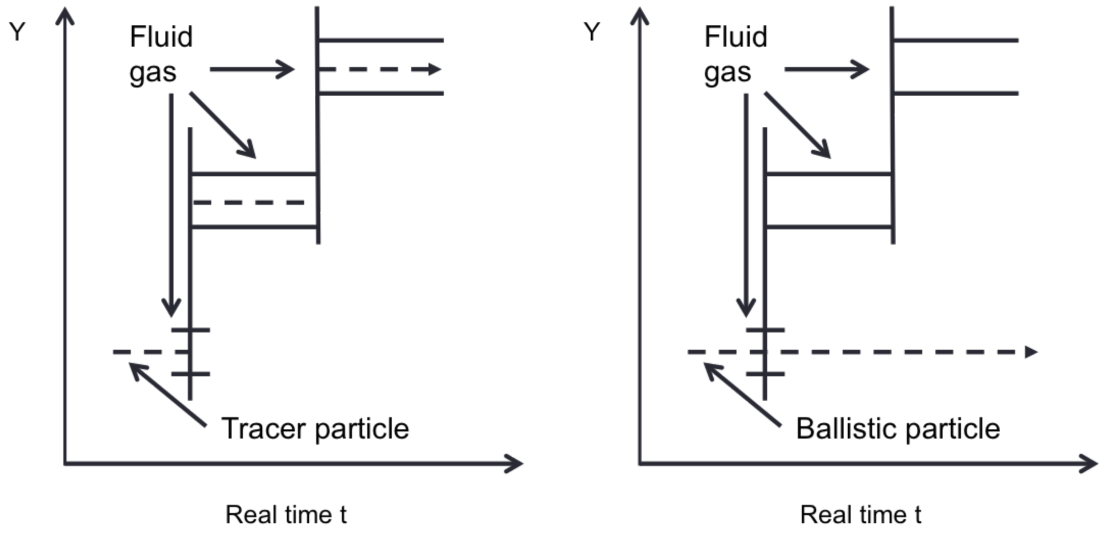

Figure 3.1: Trajectories of a tracer particle (left) and a ballistic particle (right) in the *y* direction (ODT-aligned direction) evolve with real time; dashed lines represent the particle trajectories; solid vertical lines represent eddy events; the small domain between two small horizontal lines at the occurrence of eddy events represents the location of fluid surrounding the particle. (Adapted from John Schmidt [4]).

3.2.2 Type-I particle-eddy interaction

The interaction between a particle and an eddy event is defined as both the particle and the triplet map occupying the same space-time. It is noted that the particle-eddy interaction is instantaneous in real time or advancement time t, which is referred to as *Type-I particle-eddy interaction*. However, to capture the interaction, a finite temporal interval and cubic spatial region of each eddy is assumed based on its own time and length scale. The interaction between particles and an eddy evolves in three directions governed by the x, y and z components of the Stokes' law. The interaction has the same length scale in all three directions, consistent with turbulence isotropy. The particle-eddy interaction ends when the particle leaves the idealized eddy or when the eddy lifetime has passed, whichever comes first. A new temporal coordinate is needed which is called the interaction time coordinate, θ, which describes how long the particle interacts with the eddy. When $\theta_{ixn} > t_e$, the interaction ceases even if the particles are still in the eddy box, where θ_{ixn} is interaction time between the particles and eddy. When $\theta_{ixn} \leq t_e$, the particles exit the eddy box by reaching the boundaries of the box. Simply speaking, the particle-eddy interaction is instantaneous

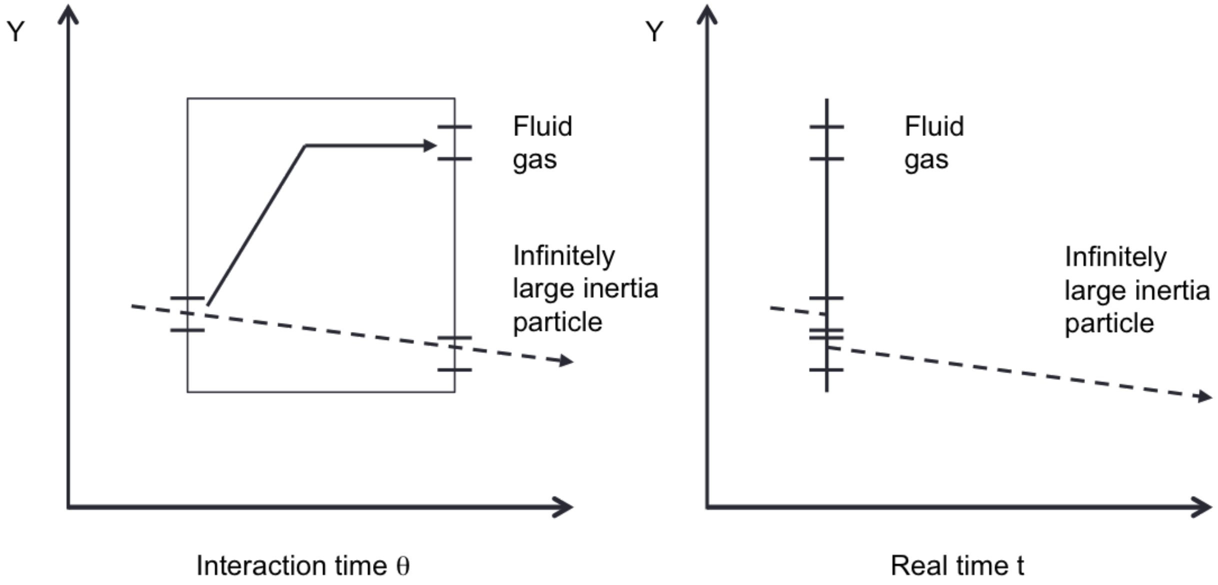

Figure 3.2: Schematic diagram of the particle-eddy interactions in the interaction and real time coordinates. The figure also illustrates the need to treat the so-called double counting effect. Dashed lines represent the trajectories of ballistic particle; rectangular box and vertical line represent eddy events; small domain between two small horizontal lines at the occurrence of eddy event represents the location of surrounding fluid of the particle. (Adapted from John Schmidt [4].)

in real time coordinate t while it exists for finite time in interaction time coordinate θ. Figure 3.2 shows the eddy effect in the interaction time coordinate (left) and real time coordinate (right) in the y direction. Eddy velocities in the x, y and z directions are defined to describe the drag force between the particle and the eddy and to obtain new positions and velocities of particles after the interaction,

$$U_e = U_g, \tag{3.34}$$

$$V_e = \frac{\triangle Y_{TM}}{t_e}, \tag{3.35}$$

$$W_e = W_g. \tag{3.36}$$

Eddy velocities U_e and W_e are the local fluid velocities at PEI location in the x and z directions, respectively. The eddy velocity V_e in the y direction is the turnover velocity of a fluid parcel containing the particles during the triplet map. $\triangle Y_{TM}$ is the displacement of a notional Lagrangian fluid particle by the triplet map at the particle location.

As shown in Fig. 3.3 of the triplet mapping operation, there are three distinct displacements of a given fluid element that correspond to its three subdivisions. Unlike the fluid elements, the particles cannot be subdivided, which requires the determination of which of three distinct fluid displacements to use in Eq. 3.35. There are two distinct ways to make this determination. One is to use the discrete implementation of the triplet map to assign a unique displacement of the fluid that contains the particles. A disadvantage of this approach is that the first and last fluid cells of the eddy subdivisions are not moved that make $\triangle Y_{TM} = 0$ in Eq. 3.35. Neglecting small displacement near eddy endpoints has a disproportionate impact near walls, where these small displacements can be the dominant mechanism [17]. This undesired affect could be minimized by using high spatial resolution, but that significantly increases computational costs.

Another more cost-effective approach is a random selection procedure. In the infinitely high-resolution case, all the flow properties including particle distribution are statistically uniform at the fine scale. Any location class of particles is equally distributed among the eddy fluid cells that correspond to three distinct field subdivisions of given fluid element. This indicates that a given particle can be statistically localized to any of the three pre-mapped subdivisions with equal probabilities. Therefore, a random selection of one of the three fluid parcels for the particle environment is used in this work. The procedure is illustrated in Fig. 3.3 by the open and filled circles that denote the notional Lagrangian fluid elements. The notional fluid elements are positioned on the triplet map on the region of the discretized ODT domain. The letters a, b, and c represent the values of fluid profiles in the given cells and serve to identify the cells. After the triplet map, the original profile (a,b,c) becomes $(a,b,c;c,b,a;a,b,c)$. The original scalar profile is compressed spatially by a factor of three, and a copy is placed on the first and last third of the eddy domain, whereas the profile is spatially inverted for the middle third. The notional Lagrangian fluid element in the third, second, or first third subdivision of the cell will be mapped to a random one of the three post-mapped locations of the same fluid property. This is shown in the figure as the open circle in the cell b, and is moved to the cell b_1 (though it could have been cell b_2 or b_3), whereas the filled circle is in the cell c, and is mapped to the cell c_2 (though it could have been cell c_1 or c_3).

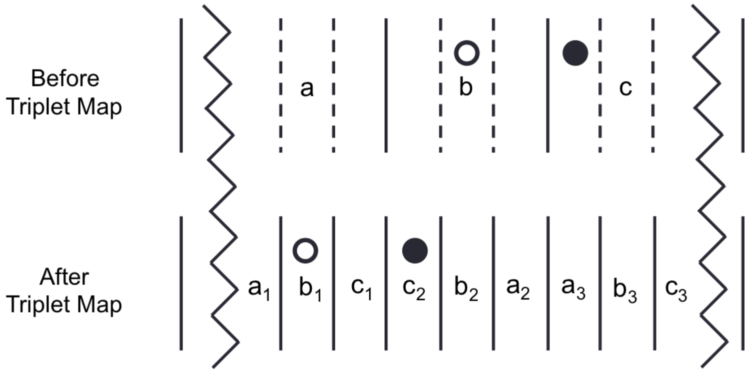

Figure 3.3: Triplet map implemented on the gas phase; jagged lines indicate eddy edges; solid lines are cell boundaries; dash lines are the $1/3$ and $2/3$ fraction location of the cell before the mapping.

Particle-eddy interaction in line direction

The y-direction (or ODT-aligned direction) drag law of particles in the interaction time coordinate θ is

$$\frac{dV_p}{d\theta} = -\frac{(V_p - V_e)}{\tau_p} f + g_y. \tag{3.37}$$

Notice that eddy events are instantaneous in real time coordinate t. Therefore, the equation of particle motion in t during the diffusive evolution of the flow is

$$\frac{dV_p}{dt} = -\frac{V_p}{\tau_p} f + g_y, \tag{3.38}$$

The boundary, y_e, of the eddy box in the y direction is

$$y_0 \le y_e \le y_0 + l. \tag{3.39}$$

Here, l is characteristic length of the eddy; and subscript 0 denotes the initial position of the particles.

Schmidt [4] found that since the particle transport is implemented instantaneously, but the momentum equation of particles is integrated for the interaction time, the concurrent diffusive advancement would result in a double integration effect. To elaborate this effect, consider a particle that has infinitely large inertia. The particle will not be affected by the eddy. However, as Fig. 3.2

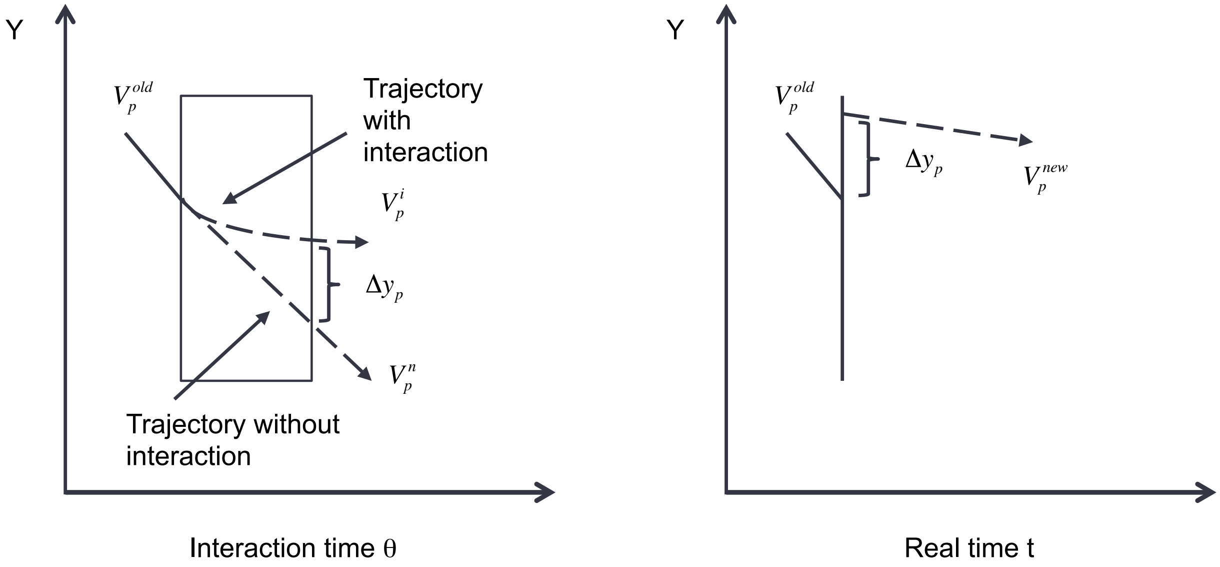
Y
V_p^{old}
Trajectory with interaction
V_p^i
Δy_p
V_p^n
Trajectory without interaction
Interaction time θ
Y
V_p^{old}
Δy_p
V_p^{new}
Real time t

Figure 3.4: New position and velocity of the particle under the coordinate of interaction time (left) and real time (right) after the particle-eddy interaction. (Adapted from John Schmidt [4].)

shows, the double integration effect will produce the shift of the particle velocity and position, which violates physical behavior. To avoid this, the particle velocity V_p^{new} and position y_p^{new} resulting from the particle-eddy interaction are computed by taking the difference of the integration solution of the momentum equation with and without the eddy velocity (Fig. 3.4). That is,

$$V_p^{new} = \triangle V_p = V_p^i\left(\theta_{ixn}\right) - V_p^n\left(\theta_{ixn}\right), \tag{3.40}$$

$$y_p^{new} = y_p^{old} + \triangle y_p = y_p^{old} + y_p^i\left(\theta_{ixn}\right) - y_p^n\left(\theta_{ixn}\right), \tag{3.41}$$

where superscript i and n indicate with and without the effect of the eddy, respectively and θ_{ixn} is interaction time.

Particle-eddy interactions in offline directions

The particle drag law(s) in the streamwise and spanwise directions are

$$\frac{dU_p}{d\theta} = -\frac{(U_p - U_e)}{\tau_p} f + g_x, \tag{3.42}$$

$$\frac{dW_p}{d\theta} = -\frac{(W_p - W_e)}{\tau_p} f + g_z. \tag{3.43}$$

Here, the boundaries of the eddy box in the x and z direction are given by:

$$x_0 + U_e\theta - \frac{l}{2} \leq x_e \leq x_0 + U_e\theta + \frac{l}{2}, \tag{3.44}$$

$$z_0 + W_e\theta - \frac{l}{2} \leq w_e \leq w_0 + W_e\theta + \frac{l}{2}, \tag{3.45}$$

where x_0 and z_0 are the initial positions of particles at the beginning of PEI (0 in the current implementation).

3.2.3 Type-C particle-eddy interaction

The Type-I PEI model described above leads to an instantaneous displacement and velocity change of the particles at the moment of the occurrence of the triplet map. The *Type-C particle-eddy interaction* model differs from the Type-I model in that the PEI occurs continuously during the continuous diffusive process. While the eddies occur instantaneously, the effect of the eddies on the particles is implemented over a finite duration during the diffusive advancement. As in the Type-I interaction, each eddy is modeled with a cubical eddy box that exists spatially over the domain $[y_0, y_0 + l]$ and temporally over the eddy lifetime t_e. Unlike the Type-I eddy, the interaction is not implemented instantaneously, but rather the eddy velocity is mapped to a spatial-temporal eddy box that starts at and continues after the eddy event. Each eddy box is advected in the off-line directions with a velocity equal to the average fluid velocity in the box at the occurrence time of the eddy. The crossing-trajectory effect is captured as the particles move relative to the eddy.

The line-directed eddy velocity is taken as $\pm(2l/\sqrt{27})/(\beta_p\tau_e)$ based on the root mean square displacement of fluid particles in an eddy due to a triplet map [9], and the sign is randomized. In the eddy space-time map, it often happens that eddy boxes will overlap. In this case, the line-directed velocity component for a given particle consists of the sum of velocities for each eddy box in which the particle is located. The off-line fluid velocities are taken as the local gas velocity on the line as before.

A significant drawback to the Type-C interaction is that it does not obey the tracer-particle limit. The fluid is mapped instantaneously to new locations during an eddy event, but the particles respond to this fluid motion over a finite time during the diffusive advancement. This may not be statistically important in particle dispersion studies, but in applications such as combustion, where particle temperature-history effects are important, the correct tracer-limiting behavior is important. Another potentially important difference is an apparent time shift. The result of an eddy triplet map is observed at the time of the triplet map in the Type-I eddies while there is a delay of time $\beta_p \tau_e$ for the same net effect to be observed with the Type-C eddies. The two models are compared below.

3.2.4 Instantaneous and continuous particle-eddy interaction

In this section, the fundamental difference between the Type-I and Type-C particle interaction implemented in this study is discussed. In a Type-I interaction, the particle has an instantaneous displacement in ODT-aligned direction when it interacts with an eddy. That is, the particle goes through discontinuous displacement due to the eddy interaction, and then the interaction will expire immediately because eddy event implementation is instantaneous. It turns out that each particle can interact with only one eddy during every Type-I interaction. In contrast to the Type-I interactions, there is no instantaneous displacement of particle motion in the Type-C interaction. In the Type-I interaction, although an eddy event is still instantaneous, the eddy effect on particles is allowed to exist in interaction time coordinate for the eddy duration. In this sense, the Type-C interaction results in a "delay" in the particle dispersion as Fig. 3.5 shows. In the Type-C interaction, the particle has continuous interactions with eddies no matter when and where it enters the same space and time region as the eddy has. It is quite likely that one particle can feel the effects of multiple eddies simultaneously. Implementation of the Type-C interactions in ODT requires keeping track of the positions of all eddies from the time each eddy is born until that individual eddy's duration has expired. In the Type-I PEI model, the particles are less likely to interact with the eddy event when the line velocity becomes larger. Assume that the velocity component in the line direction reaches the infinite limit; there is no way that the particle has a chance to enter the eddy because particle trajectories and the triplet maps are parallel lines in the space-time plane $y-t$. This is not a problem for many typical flows in which the particles move with similar or smaller velocities than the fluid. In contrast, the Type-C PEI model "extends" the eddies in the real time coordinate and thus allows the particles to interact with eddies when they occupy the same

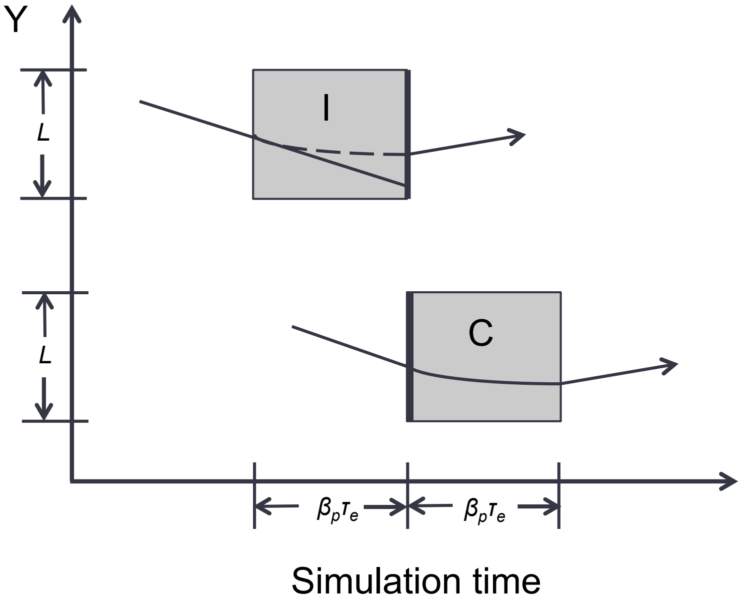

Figure 3.5: Type-I vs. Type-C particle-eddy interaction. Shadow boxes represent eddy effect over spatial domain $[y_0, y_0 + L]$ and temporal period $\beta_p \tau_e$; single solid lines represent particle trajectory; dash line represents particle "interaction" trajectory due to particle velocity history in the Type-I interaction [5].

spatial-temporal coordinate. The Type-C interaction is advantageous for cases in which particles move very quickly in the line direction. Examples of such flow might include shock-driven turbulence or buoyancy dominated flows where particles may move in a line direction corresponding to strong density gradients driving the mixing process. The particles are able to interact with an eddy in several different ways:

1. The particles could enter the eddy box in line direction at the time the eddy is born;
2. The particles could enter the eddy box through the offline edges;
3. If the eddy is still active, the particle could re-enter the eddy through all the edges of the box.

In the implementation of the Type-C interactions, a new scheme is proposed to allow eddy boxes to move in the x, y, and z directions that is similar to the idea of the Type-I interaction in this sense. That is, only the relative motion of particle and eddy box in all directions is recorded until either the particle crosses out of the box or eddy lifetime ends. This is very important for the Type-C interaction to accurately capture the effect of crossing trajectories.

The box velocity in the x (and z) direction has been described in the Type-I interaction as evolving at the local fluid velocity while it was described as the bulk (eddy-averaged) velocity for the Type-C eddies. Schmidt used the latter for all simulations [4, 25, 26]. While there is some appeal in using an eddy-average velocity, there are inconsistencies that arise in certain cases. These are most readily observed in the case of tracer particles. Particles that exist in fluid elements with velocities differing from the eddy-average velocity can cross out of the eddy even though they remain associated with fluid elements. This results in a shorter eddy interaction time and less dispersion than that of the actual fluid elements. Naturally, this breaks the coincidence of fluid and tracer particles in the Type-I interactions. This early crossing effect is severe for tracer particles because we find that the parameter β_p is relatively small leading to significantly reduced tracer dispersion when the eddy-average box velocity is used. It is possible to alter model coefficients to recover the appropriate particle dispersion, but differences will remain between the fluid and tracer evolution, and we find that the dependence of the dispersion on the Stokes number (or particle Froude number) is not correct. For the Type-C eddies, the particles do not match the tracer limit and the sensitivity to the local versus eddy-averaged velocity is less significant. Further, the application of the local velocity is more complicated for the Type-C eddies since it evolves in time. For these reasons, the simpler eddy-averaged velocity is employed for the Type-C interactions.

3.2.5 Type-IC particle-eddy interaction

In order to overcome the violation of tracer limit of the Type-C model, another alternative interaction model is introduced here, which is referred to as *Type-IC particle-eddy interaction*. Similarly, in this case, the eddy is allowed to exist in real time for the duration of the eddy lifetime. However, any particle that enters and interact with the eddy in an instantaneous Type-I way and is not allowed to interact with the same eddy in a continuous Type-C way even if the particle leaves the eddy interaction box and comes back into the box by one of the sides of eddy box. This is because the Type-I interaction already takes into account the entire lifetime of the eddy. Conversely a particle which first enters an eddy interaction box from one of the sides may not undergo a Type-I interaction with the eddy, therefore is able to interact with that eddy in a Type-C manner as long as the particle is in the interaction box and may interact with that same eddy as many times as it re-enters the box. It is worth noting that the Type-IC interaction model is able to

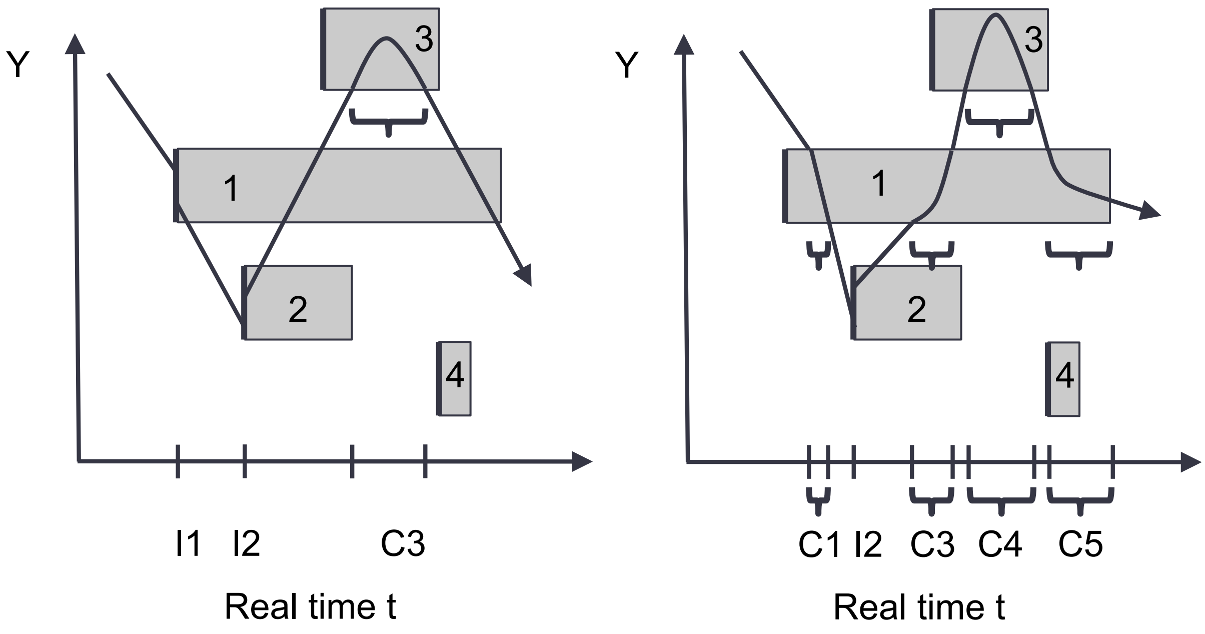

Figure 3.6: Type-IC particle-eddy interaction in two different fluid contexts.

match the tracer particle limit because in order to have a Type-C interaction a particle must enter an eddy interaction box from either of the sides, and a tracer or gas particle can not do so.

Figure 3.6 shows two possible particle trajectories in the Type-IC particle-eddy interaction context. In Fig. 3.6 (left) the particle first interacts with eddy 1 and 2 sequentially in the Type-I way ($I1$ and $I2$). Then it enters eddy 3 through the bottom side of the eddy box and experiences a Type-C interaction ($C3$). Although the particle reenters eddy 1 twice and eddy 2 once, it does not undergo any Type-C interaction with them because the Type-I interaction with eddy 1 and eddy 2 have already been taken into account at the beginning. In Fig. 3.6 (right) the particle has a Type-C interaction with eddy 1 ($C1$) and changes the direction to interact with eddy 2 in a Type-I interaction ($I2$). Then it re-enter eddy 3 to experience Type-C interactions twice ($C3$ and $C5$) due to direction change by the Type-C interaction with eddy 3 ($C4$).

3.2.6 Two-way momentum coupling

As introduced in Sec. 2.2.1, the evolution of the particle phase in a turbulent gas phase is commonly classified into three categories, one-way coupling, two-way coupling, and four-way coupling. In the current work, the two-way momentum coupling is implemented in that the volume fraction of the dispersed phase is high enough that the mean flow of the particles can induce turbulent motion in the fluid. This section gives detailed information of the implementation of two-way momentum coupling in diffusive advancement and turbulent advective mixing.

Diffusive advancement

The diffusive advancement of the fluid evolves scalar equations of momentum using a conservative finite volume method shown in Eq. 3.3-3.5, where $S_{p,u}$, $S_{p,v}$ and $S_{p,w}$ are particle source terms for the gas phase in the streamwise, ODT-aligned, and spanwise direction, respectively, as defined in Eq. 3.33. If the particles have the Type-C or Type-IC interactions with the eddies, U_{gi} are gas velocities due to the cumulative effect of active eddies; if the interactions are Type-I, U_{gi} are local instantaneous gas velocities.

Turbulent mixing (constant density)

In this section, we describe the implementation needed for the stochastic eddy events in constant-density flows with two-way momentum coupling between the particles and the fluid phase. In the single phase flows with constant density, one kernel function is added to the post triplet-map velocities to allow for energy redistributions among velocity components as shown in Eq. 3.17. Here with the momentum interactions between the phases, an additional kernel function is required to account for momentum transfer between the phases. More details are given below.

The triplet map itself is measure preserving. To ensure the conservation of kinetic energy and momentum, the triplet map can be augmented by the kernel transformation introduced in Sec. 3.1.2 when applied to the momentum field. For single phase flow with constant density, only one kernel function is enough to enforce the conservation of momentum and kinetic energy (Eq. 3.17). However, in two-way coupling implementation, only one kernel function cannot keep the momentum conserved because $\int \rho K(y)dy = 0$ and $\int \rho (V_i - V_i^{'})dy \neq 0$ due to particle source term. Thus, the triplet map operation of velocity components is shown as below,

$$V_i(y) \rightarrow V_i^{'}(f(y)) + c_i K(y) + b_i J(y), \tag{3.46}$$

where $K(y)$ is the K kernel function as in the one-way coupling, and $J(y)$ is the J kernel function defined as $|K(y)|$. As common notations denote, primed quantities represent ones following the triplet map and double primed quantities represent ones following the triplet map and kernel functions. The variables y and $f(y)$ are dropped for the simplicity in the following derivation. For momentum conservation, $\int \rho V_i dy = \int \rho V_i^{''} dy$, thereby $\int \rho V_i dy = \int (\rho V_i^{'} + \rho c K + \rho b J) dy$. Given that $\int \rho K = 0$,

$$b_i = \frac{\int \rho (V_i - V_i^{'}) dy}{\int \rho J dy} = \frac{\triangle M_{pi}}{\rho \int J dy}, \tag{3.47}$$

where $\triangle M_{pi}$ is the summation of all the momentum sources of the particles in given direction i,

$$\triangle M_{pi} = \sum m_{pk} (V_{ipk}^{new} - V_{ipk}^{old}). \tag{3.48}$$

m_{pk} is the mass of the kth particle that has interaction with the eddy, and V_{ipk}^{old} and V_{ipk}^{new} are the velocity of the kth particle before and after the interaction with the eddy, respectively.

The constant c_i is used to redistribute the energy between the three directions. When the flow in one direction loses energy, two other directions will gain the energy from this loss. Once b_i is obtained from Eq. 3.47, the constant c_i is computed in such a way that the flow in given direction i distributes the maximum energy to two other directions. The change of eddy energy in given direction i is

$$\begin{aligned}
\triangle E_i =& \frac{1}{2} \int \rho \left[\left(V_i^{'} + c_i K + b_i J \right)^2 - V_i^2 \right] dy && (3.49) \\
=& \frac{1}{2} \rho \int \left[K^2 c_i^2 + \left(2 b_i K J + 2 V_i^{'} K \right) c_i + \left(b_i^2 J^2 + 2 V_i^{'} b_i J + V_i^{'2} - V_i^2 \right) \right] dy && (3.50) \\
=& \frac{1}{2} \rho l^3 K_K c_i^2 + \left(\rho b_i l^3 K_J + \rho l^2 V_{iK} \right) c_i + \left(\frac{1}{2} \rho b_i^2 l^3 J_J + \rho b_i l^2 V_{iJ} + \triangle E_{TM} \right) && (3.51) \\
=& P_0 * c_i^2 + P_{1,i} * c_i + P_{2,i}, && (3.52)
\end{aligned}$$

with the new variables defined below,

$$K_J = \frac{1}{l^3} \int K J dy, \tag{3.53}$$

$$K_K = \frac{1}{l^3} \int K^2 dy = \frac{1}{l^3} \int J^2 dy = J_J, \tag{3.54}$$

$$V_{iK} = \frac{1}{l^2} \int V_i' K dy, \tag{3.55}$$

$$V_{iJ} = \frac{1}{l^2} \int V_i' J dy, \tag{3.56}$$

$$\triangle E_{TM} = \frac{1}{2} \rho \int \left(V_i'^2 - V_i^2 \right) dy, \tag{3.57}$$

$$P_0 = \frac{1}{2} \rho l^3 K_K, \tag{3.58}$$

$$P_{1,i} = \rho b_i l^3 K_J + \rho l^2 V_{iK}, \tag{3.59}$$

$$P_{2,i} = \frac{1}{2} \rho b_i^2 l^3 J_J + \rho b_i l^2 V_{iJ} + V_i'^2 - V_i^2. \tag{3.60}$$

The maximum removable energy from the given component i, Q_i, is the minimum value of $\triangle E_i$ that has the quadratic form in c_i. Eq. 3.52 is differentiated with respect to c_i, set to zero, solved for $\widetilde{c_i}$ at the parabola minimum, and then $\widetilde{c_i}$ is inserted into Eq. 3.52 to give

$$Q_i = -\left(P_{2,i} - \frac{P_{1,i}^2}{4P_0} \right). \tag{3.61}$$

So the change of eddy energy in given direction i can be calculated from the summation of energy loss from the direction i, Q_i, and energy gain from the directions j and k, Q_j and Q_k,

$$\triangle E_i = -\alpha Q_i + \frac{\alpha}{2} Q_j + \frac{\alpha}{2} Q_k, \tag{3.62}$$

where α is the coefficient of energy distribution. Then the value of $\triangle E_i$ is inserted into Eq. 3.52 to compute c_i, that is,

$$c_i = \frac{1}{2P_0} (-P_{1,i} \pm \sqrt{P_{1,i}^2 - 4P_0 * (P_{2,i} - \triangle E_i)}). \tag{3.63}$$

Turbulent mixing (variable density)

For the reacting flow, the density of the flow is no longer constant. Here the derivation is made by analogy to the case of constant density. Two kernel functions are added to post-triplet-map velocity components that are defined in the same way as in the constant density case,

$$V_i(y) \rightarrow V_i^{'}(f(y)) + c_i K(y) + b_i J(y). \tag{3.64}$$

Firstly, the equations of b coefficients are derived from momentum conservation. Given that $\int \rho K \neq 0$ due to variable density, the integral form of momentum conservation is,

$$\int \rho V_i dy = \int (\rho V_i^{'} + \rho c_i K + \rho b_i J) dy, \tag{3.65}$$

and then rearranged with the insertion of momentum source term of particles, $\triangle M_{pi}$, defined in Eq. 3.48 to give

$$b_i = \frac{\int \rho (V_i - V_i^{'}) dy - \int c_i \rho K dy}{\int \rho J dy} = \frac{\triangle M_{pi} - c_i \rho_K}{\rho_J}, \tag{3.66}$$

where

$$\rho_K = \frac{1}{l^2} \int \rho K dy, \tag{3.67}$$

$$\rho_J = \frac{1}{l^2} \int \rho J dy. \tag{3.68}$$

Equation 3.66 is inserted into the following expression of the change of eddy energy in given direction i,

$$\triangle E_i = \frac{1}{2} \int \rho \left[\left(V_i^{'} + c_i K + b_i J \right)^2 - V_i^2 \right] dy \tag{3.69}$$

$$\begin{aligned} &= c_i^2 * \left(\frac{1}{2} l^3 \rho_{KK} + \frac{1}{2} l^3 \frac{\rho_K^2}{\rho_J^2} \rho_{JJ} - l^3 \frac{\rho_K}{\rho_J} \rho_{KJ}\right) + c_i * \left(-l^3 \frac{\triangle M_{pi} \rho_K \rho_{JJ}}{\rho_J^2}\right. \\ &\quad \left. + l \frac{\triangle M_{pi} \rho_{KJ}}{\rho_J} + V_{i\rho K} - l^2 \frac{\rho_K}{\rho_J} V_{i\rho J}\right) + \left(\frac{1}{2l} \rho_{JJ} \frac{\triangle M_{pi}^2}{\rho_J^2} + l \frac{\triangle M_{pi}}{\rho_J} V_{i\rho J} + \triangle E_{TM}\right) \end{aligned} \tag{3.70}$$

$$= P_0 * c_i^2 + P_{1,i} * c_i + P_{2,i}, \tag{3.71}$$

where the new variables are defined as

$$\rho_{KK} = \frac{1}{l^3} \int \rho K K dy = \frac{1}{l^3} \int \rho J J dy = \rho_{JJ}, \tag{3.72}$$

$$\rho_{KJ} = \frac{1}{l^3} \int \rho K J dy, \tag{3.73}$$

$$V_{i\rho K} = \frac{1}{l^2} \int \rho V_i K dy, \tag{3.74}$$

$$V_{i\rho J} = \frac{1}{l^2} \int \rho V_i J dy, \tag{3.75}$$

$$\triangle E_{TM} = \frac{1}{2} \int \rho \left(V_i'^2 - V_i^2 \right) dy, \tag{3.76}$$

$$P_0 = \frac{1}{2} l^3 \rho_{KK} + \frac{1}{2} l^3 \frac{\rho_K^2}{\rho_J^2} \rho_{JJ} - l^3 \frac{\rho_K}{\rho_J} \rho_{KJ}, \tag{3.77}$$

$$P_{1,i} = -l^3 \frac{\triangle M_{pi} \rho_K \rho_{JJ}}{\rho_J^2} + l \frac{\triangle M_{pi} \rho_{KJ}}{\rho_J} + V_{i\rho K} - l^2 \frac{\rho_K}{\rho_J} V_{i\rho J}, \tag{3.78}$$

$$P_{2,i} = \frac{1}{2l} \rho_{JJ} \frac{\triangle M_{pi}^2}{\rho_J^2} + l \frac{\triangle M_{pi}}{\rho_J} V_{i\rho J} + \triangle E_{TM}. \tag{3.79}$$

The rest of the derivation is similar to the case of constant density. The maximum removable energy from the given component i, Q_i, is the minimum value of $\triangle E_i$ that is parabolic minimum of Eq. 3.71,

$$Q_i = -(P_{2,i} - \frac{P_{1,i}^2}{4P_0}). \tag{3.80}$$

The change of eddy energy in given direction i can be calculated from the summation of energy loss from the direction i, Q_i, and energy gain from the directions j and k, Q_j and Q_k,

$$\triangle E_i = -\alpha Q_i + \frac{\alpha}{2} Q_j + \frac{\alpha}{2} Q_k, \tag{3.81}$$

Then the value of $\triangle E_i$ is inserted into Eq. 3.71 to compute c_i, that is,

$$c_i = \frac{1}{2P_0} (-P_{1,i} \pm \sqrt{P_{1,i}^2 - 4P_0 * (P_{2,i} - \triangle E_i)}). \tag{3.82}$$

Eddy sampling

In the ODT model, each sampled eddy event is characterized by the time scale τ_e, the position y_0, and the size l, which is influenced by the instantaneous flow field. In other words, ODT accounts for the mutual interaction between the eddy rate distribution and the flow evolution. As defined in Eq. 3.22, the eddy time scale, τ_e, can be calculated from local kinetic energy and the eddy length. During particle-eddy interaction in the two-way coupled flows, the presence of particles changes the turbulent kinetic energy and thereby eddy time scale through the particle source term, $\triangle E_{pi}$ in Eq. 3.48. Particle source terms are calculated based on the interaction time of the particles with the eddy, θ_{ixn}, that is, the minimum of crossing time of particles out of the interaction and eddy lifetime, t_e. Therefore, in the implementation of two-way momentum coupling, eddy sampling and selection and particle-eddy interactions depend on each other. A necessary iteration procedure is required to determine eddy selection coupled with the influence of the particles. Here are the steps in detail:

1. Sample the size and position of the eddy;
2. Do triplet-map motion of eddy and calculate time scale of eddy based on one-way coupling as an initial guess;
3. Particles interact with the eddy, and thus particle source terms can be calculated;
4. Use particle source terms obtained in step 3 to calculate new time scale of eddy based on two-way coupling;
5. Repeat step 3 and 4 until the solution of eddy time scale is converged;
6. Decide whether the eddy is accepted using the converged solution of eddy time scale in step 5.

3.3 Temperature evolution of particles

In recent years, novel energetic materials (e.g., nano-aluminum particles [79]) with both thermal and chemical bio-agent kill mechanisms are being investigated for civilian and commercial applications. Reducing collateral effects using these novel materials requires accurate simulation of the chemical species and reactions followed by turbulent mixing with bio-agents and plume spread. Recent simulation models describe some of the mechanistic phenomena [80–83]; however, there is still a lack of understanding across the field as to how agent-defeat materials perform in turbulent conditions with elevated temperature and other environmental conditions. Little attention has been paid to developing fluid dynamic models for clumped units of the spores (micron-sized particles) in various turbulent flows, and bio-agent heating/burning in the environmental conditions following detonation (temperature, pressure, and corrosive atmospheres). Basic knowledge of the response of chemical agents and agent simulants to blast loading and high-temperature post-detonation environments are also inadequate. Furthermore, predicting where and when the flame products are hot enough to neutralize agents requires the models of detonation-induced instabilities leading to turbulent mixing. Uncertainty quantification in current mixed-grid models, when various scales and grid sizes are combined, remains a challenge.

As an integral part of this work, the ODT multiphase model is extended to the nonisothermal flows to evaluate the temperature history and probabilities of biological and chemical agent particles escaping from a blast environment, getting intimately mixed with hot detonation gas, interacting with the flame product, being distributed by turbulent instabilities, and surviving and escaping to the ambient environment.

The temperature of each particle is computed along its trajectory assuming that each particle is nonreactive and has a uniform temperature. Under such assumptions, the energy balance takes the following form:

$$\frac{dT_p}{dt} = -\frac{T_p - T_g}{\tau_H}, \tag{3.83}$$

where T_p and T_g are the instantaneous temperatures of the particle and of the fluid seen, respectively, and τ_H is the particle thermal relaxation time, defined by $\tau_H = (m_p c_p) / \left(\pi d_p^2 h_p\right)$, which is either constant or varies as a function of Re_p, depending on the particle Nusselt number expression used to estimate the particle-to-fluid heat transfer coefficient h_p. c_p is particle specific heat.

CHAPTER 4. PARTICLE DISPERSION IN HOMOGENEOUS TURBULENCE

Lagrangian particle dispersion is studied using the one-dimensional turbulence (ODT) model in homogeneous decaying turbulence configurations. The ODT model has been widely and successfully applied to a number of reacting and nonreacting flow configurations, but only limited application has been made to multiphase flows. A version of the particle implementation and interaction with the stochastic and instantaneous ODT eddy events (Type-I particle model) is presented in this chapter. The model is characterized by comparison to experimental data of particle dispersion for a range of intrinsic particle time scales and body forces. Particle dispersion, velocity, and integral time scale results are presented. The particle implementation introduces a single model parameter β_p, and sensitivity to this parameter and behavior of the model are discussed. The numerical results are analyzed to investigate the particle inertial and trajectory crossing effects. These results serve as a validation case of the multiphase implementations of ODT for extensions to other flow configurations. This chapter appears in much the same form as the paper published on *Physics of Fluid* by G. Sun et al [5].

4.1 Introduction

The motion and dispersion of particles in turbulent flow has important applications in many areas of engineering [37, 84]. As an example, turbulent reacting flows like those found in combustion often interact with particles in the form of droplets that might be a source of fuel, a source of fire suppressant or a hazardous material to be incinerated. Particles are dispersed throughout the flow field by the action of turbulence, and the extent of that dispersion is an important factor in designing effective systems.

One of the earliest predictive models for particle dispersion was developed by Einstein to describe Brownian motion through a distribution of displacements at a rate given by thermal energy [85, 86]. Taylor related turbulent fluid particle dispersion to the velocity fluctuations and their degree of correlation over time [87], while Batchelor extended this to multidimensional dispersion [88]. These concepts were directly extensible to particle dispersion, D_p, where rather than the fluid velocities and their Lagrangian autocorrelation time, the particle velocities and particle autocorrelation time are appropriate

$$\langle D_p^2 \rangle = 2 \int_0^t \int_0^{t'} V_p(0) V_p(\tau) d\tau dt'. \tag{4.1}$$

The particle velocities evolve according to the forcing introduced by the fluid drag, body forces, and other forces as appropriate (such as the Saffman lift force in velocity gradients [49, 89]). A challenge arises then because the fluid velocity at the particle location is required, and this fluid velocity is often solved only in an averaged or filtered sense due to the cost of direct numerical simulations (DNS). There are a number of approaches to modeling the instantaneous fluid velocities. The general approach involves the determination of statistical moments for the fluid velocity, the assumption of a distribution of fluid velocities from those moments that act over a given time scale (referred to as an eddy-interaction time), and the deterministic evolution of the particle forced by the given fluid velocity for a sequence of eddy-interaction times [37, 74, 75]. These approaches have found significant success, and their incorporation within large-eddy simulations (LES), where large scale anisotropy is resolved, leads to further improvement.

Here an alternate approach is presented. Rather than carry out a separate determination of the fluid moments and a sampling of expected fluid velocities, the particle evolution is integrated with a reduced dimension stochastic approach to evolve the flow field. This approach is referred to as the one-dimensional turbulence (ODT) model [7–9, 16]. Within the context of ODT fluid velocities and any associated scalars are fully resolved in a single dimension. Molecular processes like viscous dissipation evolve through a deterministic process along that single dimension, while the nonlinear turbulent cascade is modeled through a remapping procedure that reproduces key aspects of turbulent flows [90]. By carrying out a fully resolved temporal flow evolution in a single spatial dimension, the one-dimensional spectrum of velocity and scalar fluctuations is available and associated with a given physical location. A particle associated with that same physical location would then accelerate according to the velocity at that point and the appropriate drag law. While the present work focuses on the evolution of the particles in conjunction with the fluid velocity field, additional value will come through the joint evolution of the more complete fluid state, for example including a temperature field and its correlation with the velocity evolution.

The present work focuses on the process of particle dispersion within the ODT context. In this, it draws on the previous work of Schmidt and coworkers where the original Lagrangian particle tracking models within the ODT context were developed [4, 26].

Applications here focus on characteristics of ODT particle dispersion of finite Stokes number particles in homogeneous turbulence as experimentally manifest in grid-generated turbulence [2, 3]. ODT has previously been evaluated in a wide range of fluid mixing applications that demonstrate its capability to predict fluid particle dispersion in analogy to scalar mixing [10, 11, 90–92]. There are two phenomena of interest related to finite-Stokes number particles. First, inertial particles will have some slip relative to the fluid since they respond more gradually to accelerations. This leads to reduced particle fluctuations relative to the fluid [2, 41]. Second, particles acted on by body forces will have a finite mean velocity that tends to reduce the autocorrelation time as observed by particles in what Yudine [40] referred to as the "effect of crossing trajectories." This arises because the particles continuously change their fluid environment and are not acted upon for as long as a given eddy lifetime. It is shown here that the ODT particle dispersion model captures both of these phenomena through comparison with measurements in Sec. 4.3 and through analysis of the model itself in Sec. 4.4. First, we review the ODT model and describe the approach to coupling particle evolution with the ODT model in Sec. 4.2.

4.2 Model formulation

This section summarizes the ODT model and its implementation, along with the Lagrangian particle models applied and developed. In the following discussion y is the line direction, x is the streamwise flow direction (when relevant, as in grid turbulence), and z is a spanwise direction. The ODT line is generally aligned with the direction of mean shear (cross-stream, as in jets), although in the grid turbulence studied here it is along one of the directions transverse to the flow.

4.2.1 ODT model description

The ODT model has been described in detail in Sec. 3.1 of Chapter 3. A brief summary and description of the model implemented in this study is provided in this section and parallels the discussion in [16]. ODT is a stochastic model for turbulent flows that solves the unsteady, one-dimensional transport equations (diffusion equations) for mass, momentum, and optionally other scalars, such as energy and chemical species. Because the model is one-dimensional, turbulent advection cannot be computed directly. Instead, effects of turbulent advection are modeled by a stochastic mapping processes called eddy events that are implemented as so-called triplet maps, which rearrange fluid in the domain in a manner consistent with turbulent scaling laws. These eddy events are performed concurrently with the solution of the diffusion equations.

Eddy events are parameterized by the eddy location y_0, eddy size l and corresponding eddy timescale τ_e that depends on y_0 and l. The size, location, and frequency of eddies occur stochastically on the domain as described below. Each eddy event is implemented as a triplet map that consists of replacing each scalar in the eddy region with three copies of the scalar, each compressed spatially by a factor of three and lined up along the eddy region, with the central copy spatially inverted. The triplet map is consistent with the behavior of a canonical turbulent eddy in that it is continuous, conservative of all quantities (measure preserving), increases scalar gradients, and decreases length scales locally (by the factor-of-three compression). This compression is facilitated in the current implementation by the use of an automatically adapted computational grid, with assumed piecewise-constant scalar profiles in each grid control volume. An adaptive grid is convenient, but not necessary, as several discrete implementations have been used (including the original implementation of the model [7]). The adaptive formulation avoids the need for a discrete transport correction [93], and eddy sizes are not limited to multiples of three times the grid spacing. In the present implementation, grid cells are split where the edges of the eddy intersect the cell.

The specification of eddies is dependent on the spatially evolving momentum fields. Eddies are more likely in regions of high shear, and shear is locally increased by triplet maps, resulting in an eddy cascade. The diffusive advancement of the velocity fields smoothens the flow with viscous dissipation concentrated at the smallest scales.

The solution evolution procedure is as follows. Beginning with the initial condition, a candidate eddy is sampled from the joint PDF function $P_0(y_0, l)$ in Eq. 3.19, and the occurrence time is sampled as a Poisson process with mean rate $1/\Delta t_s$. The eddy is accepted or rejected with probability P_a given in Eq. 3.21. If rejected, the process is repeated, keeping track of cumulative sampled time $t_{s,c}$. If accepted, the eddy is implemented, and the diffusion process is solved for a time duration equal to $t_{s,c}$. (Diffusive advancement is also performed to advance the solution in the event that no eddies occur within a small factor of the characteristic grid diffusion timescale.) Further details of the eddy selection procedure, along with the form of $P_0(y_0, l)$ are given in the chapter 3.

The time Δt_s is initialized as $0.1\overline{P}_a\overline{\Delta y}^2/\nu n$, where n is the number of grid points, ν is the kinematic viscosity, $\overline{\Delta y}$ is the average grid spacing, and $\overline{P}_a$ is a specified average acceptance probability (here set to 0.02). The diffusive timescale $\overline{\Delta y}^2/\nu$ at the grid cell size approximates lower bound on an eddy timescale, and the factor $1/n$ reflects the proportionality of the total rate to the domain size. The sampling time Δt_s is dynamically adjusted during the simulation to maintain the specified $\overline{P}_a$.

In the vector formulation of ODT (three velocity components evolved), pressure scrambling and return-to-isotropy effects are modeled by adjusting the triplet mapped velocities by adding a term $c_i K(y)$, where subscript i denotes the velocity component, and c_i is given by [8]

$$c_i = \frac{l^2}{\int_{y_0}^{y_0+l} K(y)^2 dy}\left(-U_{K,i} + \mathrm{sgn}(U_{K,i})\sqrt{\frac{1}{3}\sum_i U_{K,i}^2}\right). \tag{4.2}$$

Here, a large eddy suppression mechanism [9–11] is incorporated, in which the criteria applied is

$$l \leq \beta \times L_0(t/t_0)^a, \tag{4.3}$$

where $L_0(t/t_0)^a$ is the time-evolving integral scale, with experimental [2] $L_0 = 2.8$ cm and $t_0 = 0.159$ s $(x/M = 41)$. Parameter $a = 0.45$ is adjusted to fit the experimental measurements, and β is an adjustable parameter.

The diffusive advancement portion of the simulation consists in solving three components of the momentum equations (velocity equations). The vector formulation [8] of ODT solves three components of the velocity in order to account for return-to-isotropy effects. They are also important in the particle model discussed below. These velocities are primarily used in specifying the eddy event frequencies, and are solved as scalar momentum equations in the diffusive advancement, but otherwise do not act as advecting velocities (except as detailed in Sec. 4.2.2). Advection is modeled with the eddy events.

The solution is evolved on a finite-volume computational grid. A Lagrangian formulation is applied and grid cells are allowed to expand and contract with the flow (which does not occur in the incompressible simulations presented here). The mass balance in this formulation reduces to $\rho \Delta y =$ constant for any given grid cell. The momentum equations discretized for a given grid cell are given by Eq. 3.3 through 3.5. The equations are normally solved using the explicit Euler method for efficiency, but the second order Modified Midpoint method [94] is also implemented for comparison. Spatial derivatives are evaluated using second order (on uniform grids) central differences.

Mesh adaption is applied during implementation of eddy events, and before and after diffusive advancement. Grid positions are based on a uniform scalar arc length profile between cells with limitations on the minimum allowed cell size (to avoid unphysically small cells by merging with a neighbor), and a constraint on the relative sizes between two adjacent cells. The reader can see the study in [16] for more details.

4.2.2 Lagrangian particle model

The description and implementation of the Lagrangian particle model is summarized in Sec. 3.2 of Chapter 3. The Type-I particle model is used in the study of this chapter. The brief description of model implementation is provided in this section.

For relatively small particles in dilute flows, the following drag law describing the particle motion is used for coordinate direction i:

$$\frac{dU_{p,i}}{dt} = -\frac{1}{\tau_p}(U_{p,i} - U_{g,i}) + g_i. \tag{4.4}$$

Here, g_i is the acceleration associated with any body force, $\tau_p = \rho_p d_p^2/18\mu f$, and $f = 1 + 0.15 Re_p^{0.687}$, where $Re_p = \rho_g d_p |\vec{V}_g - \vec{V}_p|/\mu$. Subscript p refers to particles and subscript g refers to the fluid. This chapter focuses on fundamental understanding of the behavior of individual particles assuming one-way coupling that ignores the effect of particles on the fluid phase.

Particles interact with the fluid during the instantaneous eddy events that account for turbulent advection and during the diffusive advancement. During diffusive advancement the particle drag law is integrated (velocity and position) along with the fluid equations. The fluid velocity in Eq. (4.4) is the local ODT velocity component in the off-line directions, but is zero in the line-direction (for incompressible flows) since the advection in this direction is treated through the eddy events and continuity implies zero advecting velocity on the one-dimensional ODT line.

The primary advection mechanism through which dispersion is modeled within the context of ODT is through particle-eddy interactions (PEI). An eddy (triplet map) results in fluid displacement and the PEI consists of computing the particle velocity and displacement in response to this fluid displacement during the eddy event. Eddy events occur instantaneously, and in the Type-I model the PEI is also implemented instantaneously. However, to compute the PEI, integration is performed in a so-called PEI time coordinate θ.

In the PEI time coordinate θ, each eddy is conceptualized as a cubical eddy box (though extents in different directions could be varied). In other words, an eddy exists in a defined three-dimensional space for a defined duration. The velocity and the relative motion of the particle and the eddy box are tracked to allow the prediction of the crossing-trajectory effect. The particle is assumed initially to be in the center of the box in the off-line directions (x, z), and at its initial location in the line-direction (y). The eddy box is stationary in the line-direction as per continuity, but moves in the off-line directions with velocity components equal to the fluid velocity components at the initial location of the particle in the box. An alternative for the off-line box velocities is to use the average of the local ODT velocity components [17]. However, this may result in particles crossing out of the eddy box in the tracer-particle limit (which should not happen) due to the difference in the particle and eddy box velocities.

The particle can interact with an eddy over the minimum of two durations: (1) the duration of the eddy, or (2) the time over which the particle remains within the conceptual eddy box. The eddy duration is related to the eddy rate, Eq. 3.22, but it is not strictly the inverse of the eddy rate τ_e. Rather, the eddy rate is only proportional to a local measure of the velocity fluctuations, E_{kin}, over the eddy length l. To account for the well-known eddy-crossing phenomenon, a measure of this eddy duration is required. For models of the random walk class in the context of k-ε modeling, this time scale is of the form $\sqrt{3/2}C_\mu^{3/4}k/\varepsilon$ and the eddy length scale is similarly modeled [37,74,75] as $C_\mu^{3/4}k^{3/2}/\varepsilon$. In those models, a proportionality constant is determined through calibration with experimental data, and a similar approach is required in relating the eddy rate to the eddy duration in ODT. This relation is taken as $\beta_p\tau_e$ and the PEI time θ_{ixn} will equal the smaller of $\beta_p\tau_e$ or the time θ_c at which the particle exits the eddy box. Here, β_p is an adjustable parameter discussed in detail in Sec. 4.4.

The eddy exit time θ_c is computed by integrating the drag law given in Eq. 4.4 and solving for the exit time (assuming the particle is not captured by the eddy, in which case $\theta_{ixn} = \beta_p\tau_e$). This is done in all three directions, and the minimum time is taken. The solution to Eq. 4.4, assuming constant f in τ_p, and using $dy_{p,i}/dt = V_{p,i}$, is given by

$$V_{p,i} = V_{g,i} + \tau_p g_i - (\tau_p g_i + V_{g,i} - V_{p0,i})e^{-\theta_{ixn}/\tau_p}, \tag{4.5}$$

$$\begin{aligned} y_{p,i} =& y_{p0,i} + V_{g,i}\theta_{ixn} + \tau_p g_i \theta_{ixn} - \\ & \tau_p(\tau_p g_i + v_{g,i} - V_{p0,i})(1 - e^{-\theta_{ixn}/\tau_p}), \end{aligned} \tag{4.6}$$

where $V_{p0,i}$, and $y_{p0,i}$ are the initial particle velocity and location, respectively.

Given the interaction time θ_{ixn}, the line-directed particle position y_p and velocity V_p are computed by integrating a modified version of the particle drag law for time θ_{ixn}. Because the drag law is also integrated during the diffusive advancement in the simulation time coordinate, it is important that the PEI only alters the eddy position and velocity due to the eddy contribution. This is done by taking the difference of the particle velocity computed in Eq. 4.5 and the particle velocity using the same equation with the gas velocity set equal to zero. The same is done for the particle position. The resulting triplet map-induced changes are

$$\Delta V_p = V_g(1 - e^{-\theta_{ixn}/\tau_p}), \tag{4.7}$$

$$\Delta y_p = V_g\theta_{ixn} - V_g\tau_p(1 - e^{-\theta_{ixn}/\tau_p}), \tag{4.8}$$

and the post triplet map state is $V_p = V_{p0} + \Delta V_p$, $y_p = y_{p0} + \Delta y_p$. In these equations, the gas velocity is taken as $\triangle Y_{TM}/\beta_p\tau_e$, where $\triangle Y_{TM}$ is the local fluid particle displacement defined by the triplet map.

During the PEI, the x and z velocity components (u and w) are used only to compute θ_c and hence θ_{ixn}, but the particle velocity in those off-line directions is not modified during the PEI process because these particles evolve during diffusive advancement over the full simulation time under the influence of the locally evolving ODT fluid velocity in those directions. As particles are confined to the ODT line, there are no advective displacements of particles in the x and z directions. However, since the particles and fluid retain velocity components in these directions, these components may be integrated to study, e.g., streamwise particle dispersion.

Figure 4.1 (a) shows the size, location, and occurrence time of eddies in a typical ODT realization of grid-generated turbulence [2,3]. The instantaneous eddies are denoted by horizontal line segments. The extent of the eddies in the PEI time coordinate θ is depicted in Fig. 4.1 (b), though this does not show the full eddy-box size, and the motion of the eddy boxes as has been described.

The Type-I formulation described has the important and desired effect of satisfying the tracer ($\tau_p \to 0$) and ballistic ($\tau_p \to \infty$) limits. In the tracer limit, the final particle position matches the fluid particle position induced by the triplet map since $\Delta y_p = v_g \theta_{ixn} = \triangle Y_{TM}$ for $\theta_{ixn} = \beta_p \tau_e$ and $V_g = \triangle Y_{TM}/(\beta_p \tau_e)$. In the tracer limit, the particle velocity after the eddy is $V_g = \triangle Y_{TM}/(\beta_p \tau_e)$ (the ODT-aligned eddy velocity component), but relaxes instantaneously to the zero gas velocity during the subsequent diffusive advancement. In the ballistic limit, the particle velocity and position are unchanged by the eddy. Inertial particles show intermediate behavior.

4.3 Results

In this section model predictions are presented, first at the level of properties that can be derived directly from the model and then through comparison with available literature results.

4.3.1 Grid-generated turbulence

The particle dispersion model is compared to the experimental decaying grid turbulence results of Snyder and Lumley [2] and Wells and Stock [3]. Snyder and Lumley studied the particle motion in a vertical wind tunnel, in which four particle types were used: hollow glass (HG), corn pollen (CP), solid glass (SG), and copper (Cu). The HG particles are similar to fluid particles due

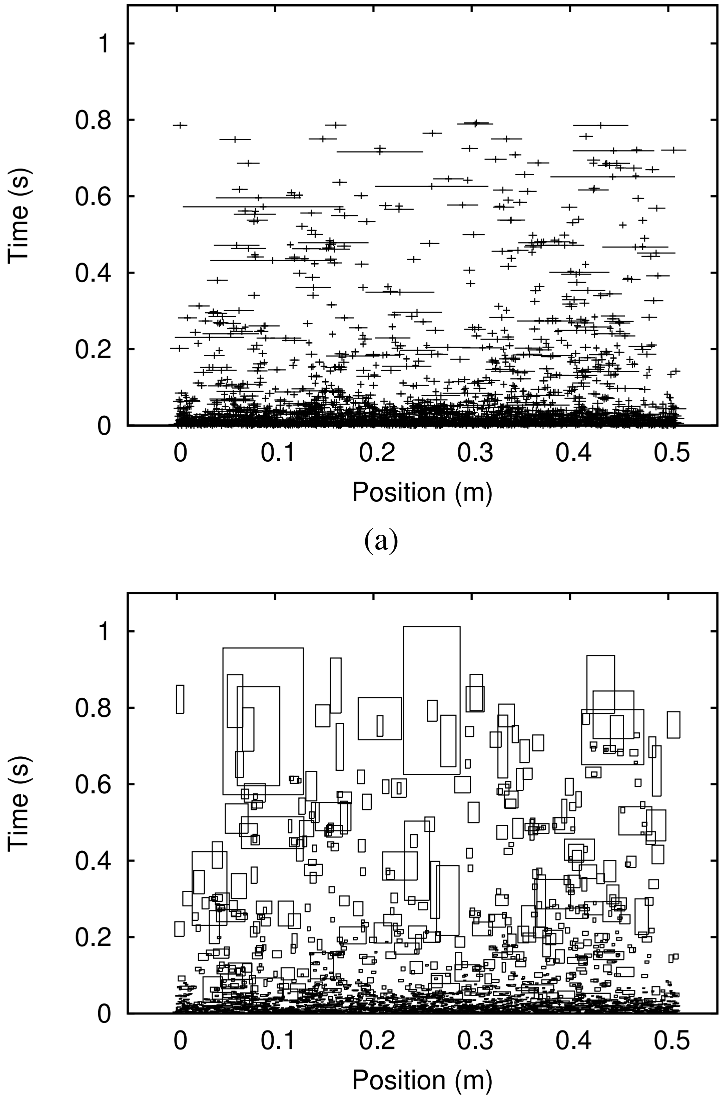

(a)

(b)

Figure 4.1: Maps of eddy sizes, locations, and occurrence times for a typical ODT realization for decaying homogeneous turbulence. Plot (a) shows instantaneous eddy locations; plot (b) illustrates eddy box extents for the particle eddy interactions (PEI) in the PEI time coordinate θ.

Table 4.1: Particle properties of Snyder and Lumley [2].

	hollow glass	corn pollen	solid glass
diameter (μm)	46.5	87	87
density (kg/m^3)	260	1000	2500
$\tau_p f = \rho_p d_p^2/18\mu$ (ms)	1.7	23	58

Table 4.2: Particle properties of Wells and Stock [3].

diameter (μm)	density (kg/m^3)	$\tau_p f$ (ms)	terminal velocity(cm/s)	particle acceleration(m/s^2)
5	2475	0.192	5.86	305.2
			17.06	888.5
			20.91	1089.1
			23.65	1231.8
57	2420	24.4	0	0
			25.8	10.6
			54.5	22.3
			108	44.3

to the small particle timescale compared to the Kolmogorov scale. Since the behavior of the solid glass is nearly identical to the copper, results are presented for the HG, CP, and SG particles. Wells and Stock [3] studied glass beads of two sizes in a horizontal wind tunnel, where the particle body force was altered by means of an electric field. Both experimental wind tunnels were operated under similar conditions with grid spacing M = 2.54 cm and a mean velocity U_0 = 6.55 m/s. The particle properties are listed in Tables 4.1 and 4.2.

The ODT simulations are conducted using a 0.508 m (20M) domain width. The initial velocity profile is taken as a sine wave (as done by Kerstein [7]): $U(y,0) = U_0 \sin(2\pi y/M)$, where $U_0 = U\sqrt{2S/(1-S)}$ gives a u variance in the grid-plane equal to the variance in a uniform profile with $u = 0$ for a grid-blocked area fraction S, and $u = U/(1-S)$ for an open area fraction $1-S$. The V and W velocity components are initially zero. The ODT parameters are $C = 5.2$, $Z = 10$, and $\beta = 2.4$. Also, for the large-eddy suppression mechanism $t_0 = 0.159$ and $L_0 = 0.028$, taken

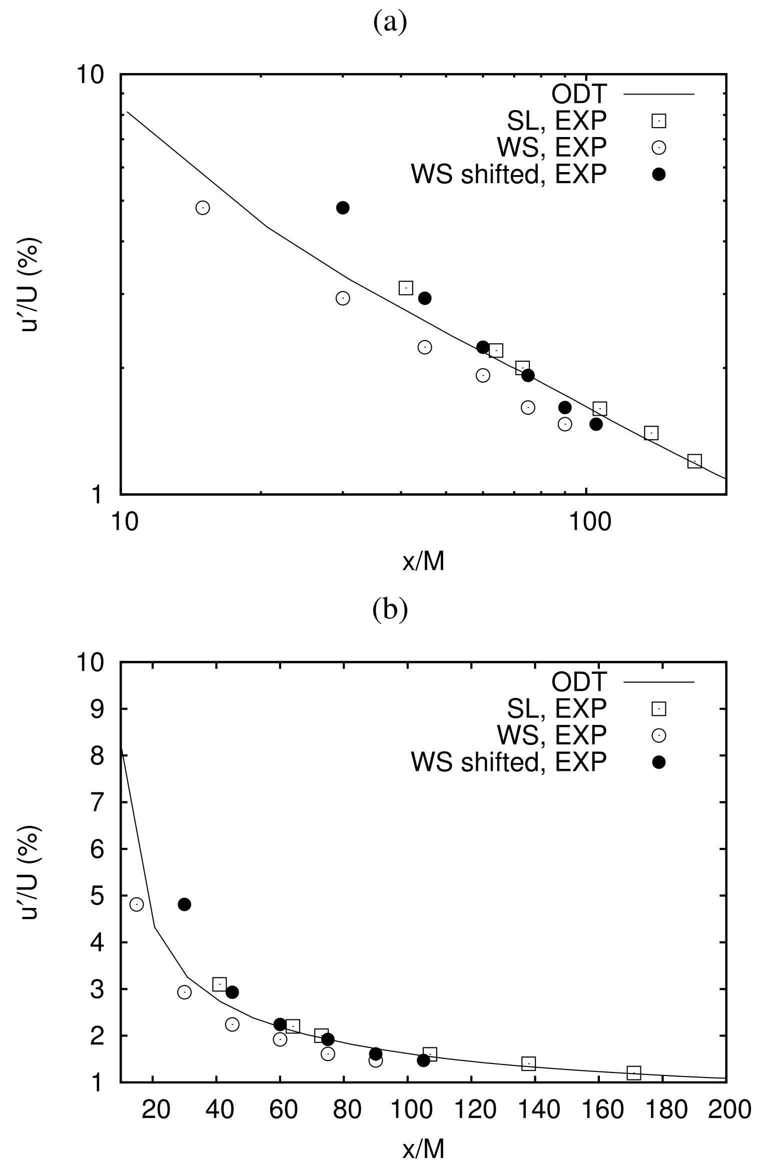

Figure 4.2: Normalized RMS streamwise velocity fluctuations: predictions and experiments of Snyder and Lumley [2] (SL), and Wells and Stock [3] (WS) on log (a) and linear (b) scales. The WS shifted data are Wells and Stock measurements shifted 15*M* to the right.

from Snyder and Lumley [2]. Simulations were performed using 2048 ODT realizations each with a single particle of a given type initially located in the center of the domain.

Figure 4.2 shows the decay of the streamwise root mean square (RMS) velocity compared to the experimental data. Both the measurements and predictions follow a power-law decay with an exponent of -1.2.

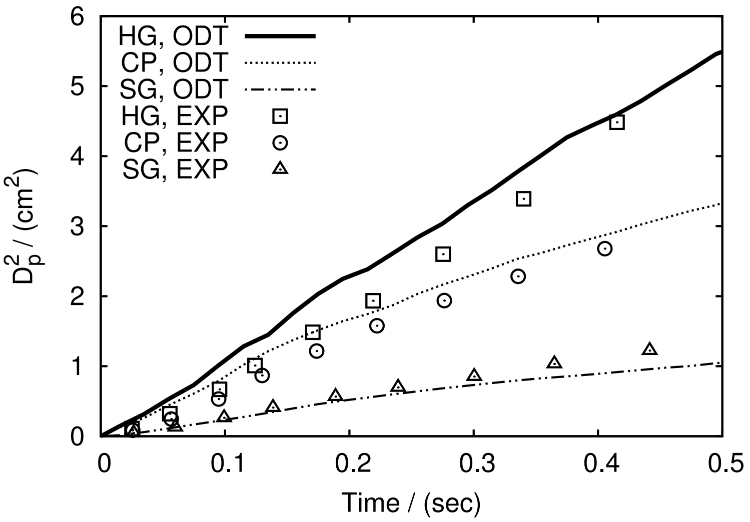

Figure 4.3: Comparison of ODT and experimental particle dispersion of Snyder and Lumley [2].

The gas decay curve in Fig. 4.2 can be matched by ODT using no large eddy suppression (with a different C parameter), but the resulting particle dispersion is incorrect due to the occurrence of unphysically large eddies causing disproportionate particle dispersion. Without suppression, such large eddies may occur even though the evolution time is less than the time for such a displacement to occur. β was selected together with C so that the gas decay curve is matched, and the dispersion of fluid particles approaches that of the hollow glass dispersion, presented below. The Wells and Stock tunnel has a similar decay rate but lower turbulent intensity at a given location; their data agree with Snyder and Lumley when shifted $15M$ to the right [95] as shown in Fig. 4.2.

4.3.2 Particle dispersion

The ODT model mean square dispersion D_p^2 (where D_p is the RMS particle displacement) predictions with $\beta_p = 0.05$ are shown with experimental measurements from Snyder and Lumley for the three particle types in Fig. 4.3. The reference position for dispersion of a given particle is consistent with the first experimental camera, which was located at $x/M = 68$. The greatest dispersion is obtained by the hollow glass, with dispersion decreasing for the corn pollen and solid glass. The dispersion trend in Fig. 4.3 is consistent with eddy trajectory crossing being the factor

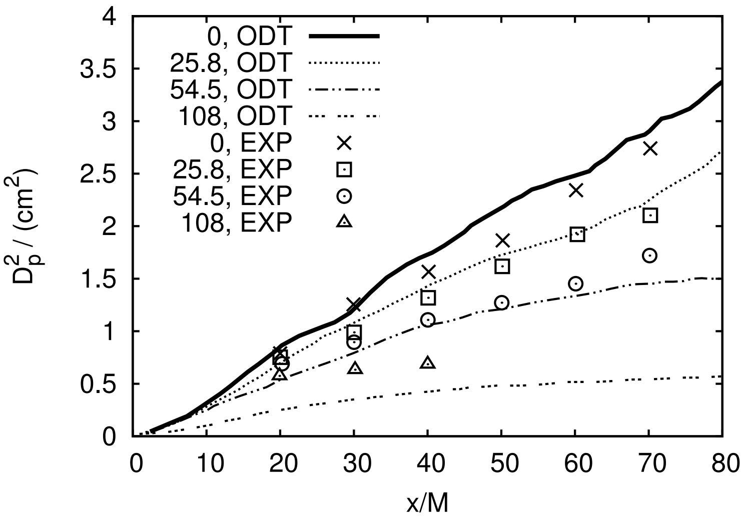

Figure 4.4: Comparison of ODT and Wells and Stock [3] particle dispersion for 57 μm particles for four terminal velocities shown in the legend in units of (cm/s).

that limits dispersion: particles with larger τ_p and larger settling velocities V_d are less affected by eddies.

To better understand the role of the settling velocity and the crossing trajectory effect, Wells and Stock measured dispersion as a function of V_d by using charged particles and varying the electric field strength. Figure 4.4 shows that in ODT particles also disperse less as particle settling velocity, $V_d = \tau_p g$, (where g is the resulting electric field acceleration), increases in agreement with the trajectory-crossing theory [41] and measurements (Wells and Stock). Wells and Stock did not specify the reference position in their published results, and in this study, the particle dispersion is referenced to $x/M = 15$. As the results for the 57 μm particles in Fig. 4.4 show, the crossing-trajectories effect significantly influences dispersion with the different particle terminal settling velocities considered.

Figure 4.5 compares the evolution of eddy time scale $\beta_p \tau_e$ with $\beta_p = 0.05$ to different particle relaxation time scales τ_p. The plotted evolution time is relative to the particle dispersion reference location (time zero). The eddy time scale is roughly lognormally distributed, varying over orders of magnitude as expected, and particles in ODT experience the full spectrum of time scales. Other characteristics of lognormally distributed variables are that the mean is larger than the most typical value and that the RMS is comparable to the mean value, both of which are plotted in

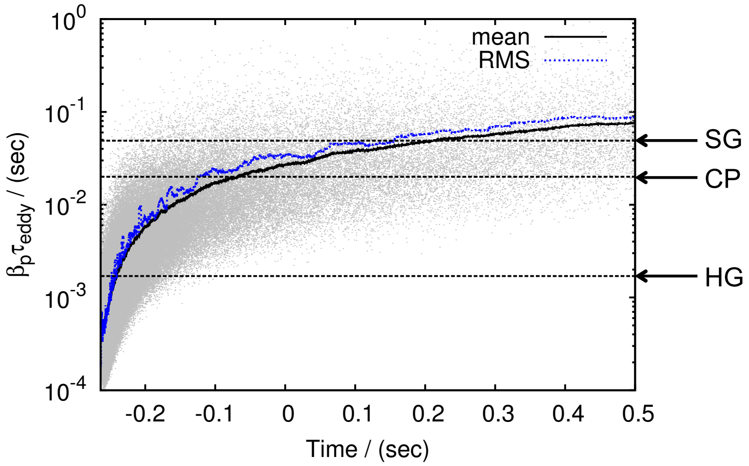

Figure 4.5: Scatter plot of eddy time scales with the corresponding mean and RMS along with particle time scales. Time zero is the dispersion reference time. Eddy information is collected from 10 representative realizations.

Fig. 4.5. The Snyder and Lumley particle time scales, τ_p are plotted as horizontal lines in Fig. 4.5. It is seen that a large number of eddies have time scales, $\beta_p\tau_e$, smaller than the particle time scales. Initially, most eddies are small and the corn pollen and solid glass particle timescales are greater than the mean eddy timescales. At positive times the corn pollen and solid glass particles have particle time scales similar to the eddy timescales, though the eddy timescales are generally above the corn pollen timescale, while for the solid glass the mean eddy timescale transitions from above to below the solid glass timescale at around 0.2 s. Conversely, the hollow glass timescale is much smaller than the eddy timescales at positive times.

Particle inertial effect and the crossing trajectory effect are the two most significant features in understanding particle dispersion for configurations studied here. The dispersion coefficient relative to that of a fluid tracer is plotted in Fig. 4.6 as a function of a dimensionless particle settling velocity analogous to a particle Froude number. The velocity fluctuation used in the normalization is $u' = 0.1$ m/s. The particle terminal settling velocity is normalized by the fluid RMS velocity fluctuations so that this normalization is equivalent to a normalized particle time constant if the body forces are all equal. The review of Loth [84] shows similar results of finite τ_p dispersion coefficients normalized by the tracer dispersion coefficient. For given fixed gravity shown in Fig. 4.6 (a), $\gamma = V_d/u' = g\tau_p/u'$ is varied by varying τ_p. In that figure, small light particles disperse at similar rates to fluid elements, and large heavy particles disperse much less as expected. Figure 4.6 (b) shows results varying the terminal velocity through the externally imposed electric field, for the two particle sizes (separated by the vertical dotted line) measured by Wells and Stock. When the terminal velocity, V_d, approaches zero, the crossing trajectory effect becomes trivial and particles remain trapped inside an eddy and behave like fluid particles. However, as V_d increases, particle traversal of the eddy takes over the interaction and reduces particle dispersion. ODT predictions in those plots are shown for multiple values of the parameter β_p with the chosen value of $\beta_p = 0.05$ matching the data well. Further discussion of the effect of β_p is given in Sec. 4.4. Experimental results are also shown in Fig. 4.6 for comparison.

4.3.3 Derived statistics

While the Type-I particle-eddy interaction model provides instantaneous displacements as in the Einsteinian approach, it is possible to determine the particle velocity statistics that lead to those displacements. This velocity profile is termed the particle velocity history V_{ph}, and is computed by modifying the particle velocity computed during the continuous diffusive advancement to account for the advection. For a given PEI, the particle velocity profile for a time θ_{ixn} before the eddy occurrence time t_{eo} is modified so that the particle displacement due to the resulting velocity history is what results from the instantaneous triplet map. That is,

$$V_{ph}(t) = \begin{cases} V_p + V_g(1 - e^{-(t_{eo}-t)/\tau_p}) & \text{if } t_{eo} - \theta_{ixn} \leq t \leq t_{eo}, \\ V_p & \text{otherwise.} \end{cases}$$

This effectively maps the advective velocity in the Type-I PEI time coordinate to the real coordinate so that particle velocity statistics may be computed. Note that V_{ph} does not affect the actual particle evolution during the simulation but is computed for comparison of ODT results with traditional velocity-fluctuation and correlation-time models.

Given these particle velocity histories, particle velocity statistics are computed for the conditions of the comparisons in the following discussion. Since the velocity fluctuations decay as shown in Fig. 4.2, statistics are taken 0.2 s after the particle injection reference point ($x/M = 68$). To smooth the velocity statistics, we take advantage of the fact that the inverse particle kinetic

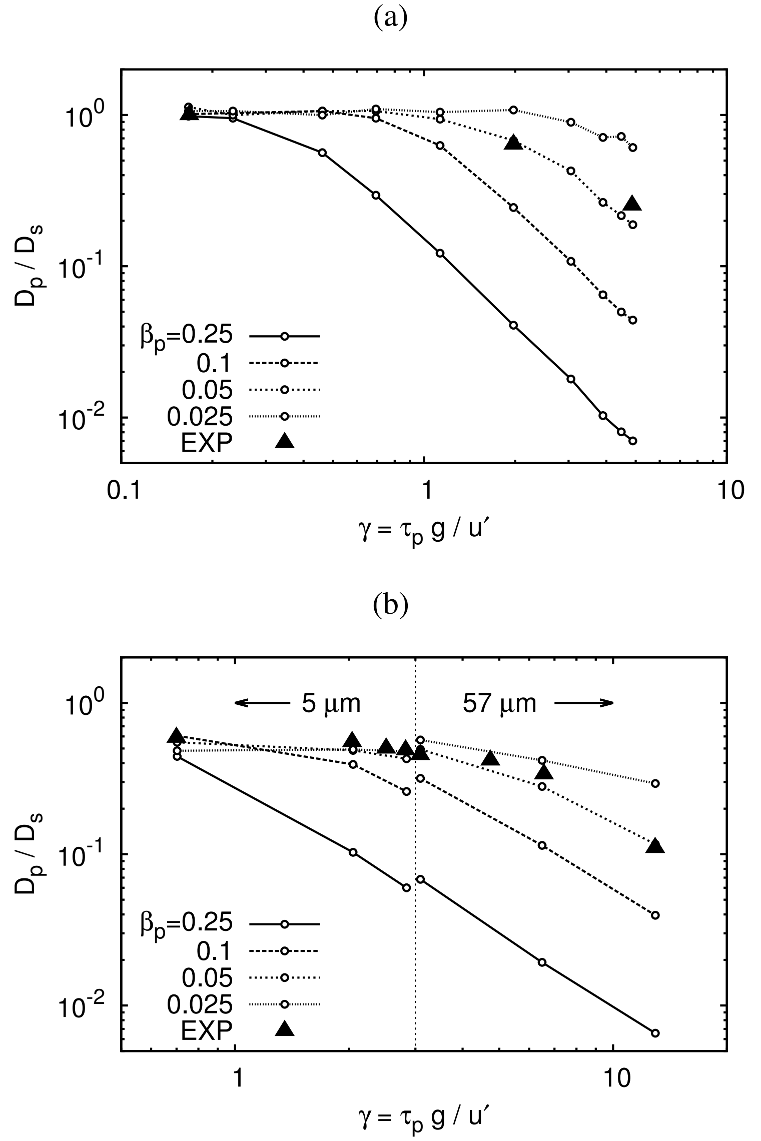

Figure 4.6: Normalized particle dispersion versus normalized particle terminal velocity for various β_p (shown in the legends). Plot (a) shows simulation results versus γ where γ is varied by varying τ_p (with $V_d = g\tau_p$), and compares to measurements of Snyder and Lumley [2]. Plot (b) shows results versus γ where γ is varied by varying particle acceleration for two particle sizes (5 μm, and 57 μm to the left and right, respectively, of the vertical dotted line), compared to measurements of Wells and Stock [3].

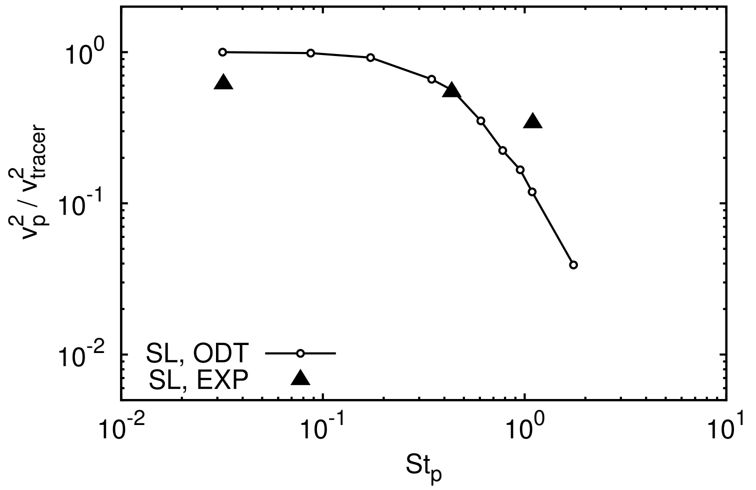

Figure 4.7: Particle velocity fluctuation as a function of particle Stokes number.

energy decay $(1/\overline{V_{ph}^2})$ is essentially linear with respect to the fluid evolution time, and we compute a linear fit over the simulation time 0.2 ± 0.1 s and interpolate to the statistic of interest at 0.2 s.

The particle velocity fluctuations normalized by the fluid tracer velocity fluctuations are plotted in Fig. 4.7 as a function of the particle Stokes number, $St = \tau_p / (\beta_p \overline{\tau_e})$ where $\beta_p \overline{\tau_e} = 0.053$ is the average eddy time scale at 0.2 s plotted in Fig. 4.5. The fluid tracer velocity fluctuations are computed similarly to the particles by fluid element displacements by triplet maps. The experimental data [2] is also shown normalized by the reported gas turbulence velocities. As expected, particles with larger Stokes numbers experience reduced fluctuations. This is a direct consequence of the dependence of the ratio θ_{ixn}/τ_p appearing in Eq. 4.7, but two effects contribute to this. Larger τ_p or larger Stokes number particles have a reduced response to rapid turbulence fluctuations; that is, the particles act as a low-pass filter because of the ratio of fluid to particle time scales. Also, larger τ_p particles have larger terminal velocities under the influence of body forces leading to a reduction in θ_{ixn}/τ_p through the crossing trajectory effect. These effects will be further discussed in Sec. 4.4.

The particle velocity histories can also be used to determine the particle Lagrangian integral time scale, or the autocorrelation time. These results have been computed and will be shown as a function of both τ_p and β_p in the Sec. 4.4. The product of this particle time scale and the velocity fluctuations in Fig. 4.7 gives the dispersion coefficient following Taylor's approach. Here we note that the derived particle velocity history statistics suggest that reduced dispersion at larger τ_p (Fig. 4.6) can be attributed more to variations in the particle velocity fluctuations (Fig. 4.7) than the integral time scale given the β_p selected here for the ODT model. This will be described further below.

4.4 Discussion

The implementation of particles into ODT introduces a single parameter, β_p, that relates the turbulence characteristics to the particle-eddy interaction time by scaling the turbulent time scales. This type of parameter is common to other particle-turbulence interaction models [37, 74, 75]. To allow the model to match the tracer particle limit, β_p plays an additional role in the context of ODT since the triplet-map driven fluid velocities are determined by $V_g = \triangle Y_{TM}/(\beta_p \tau_e)$. In this section we discuss the variation in predictions associated with different values of β_p.

In Fig. 4.6 the predictions of relative particle dispersion coefficients for several values of β_p were given. In the regime where crossing trajectory effects are important (large particle Stokes or Froude numbers), larger β_p results in reduced dispersion. This arises because of the influence that β_p has on the interaction time θ_{ixn} together with the eddy velocity V_g.

The total displacement associated with an eddy is determined by the combination of the displacement during the eddy event given by Eq. 4.8 and the resulting drift during a deceleration when the particle leaves the eddy with the velocity increment given by Eq. 4.7, $V_g(1-\exp(-\theta_{ixn}/\tau_p))$. For $V_{p0,i} = 0$ and a post-eddy relaxation time much greater than τ_p the total displacement per eddy is $\theta_{ixn}\triangle Y_{TM}/(\beta_p \tau_e)$ (here deterministic displacement due to body forces is not counted). When eddy-crossing is not occurring ($\theta_c > \beta_p \tau_e$), the interaction time is simply $\beta_p \tau_e$ and the displacement per eddy reduces to $\triangle Y_{TM}$. This is appropriately equivalent to the fluid dispersion and corresponds to the horizontal asymptote in Fig. 4.6.

Eddy crossing is typically associated with a body-force driven settling velocity. Assuming the particle has reached its terminal velocity, the expected crossing time is $\theta_c \approx l/(2g\tau_p)$ where the factor of two assumes the eddy length to be crossed is $l/2$ on average. With this as the interaction time, when $\theta_c < \beta_p \tau_e$ the displacement per eddy is $l\triangle Y_{TM}/(2g\beta_p \tau_e \tau_p)$ leading to the reduced dispersion in this limit seen in Fig. 4.6.

To better understand the ODT dispersion predictions, it is instructive to identify the scaling present in the model. The particle dispersion coefficient may be written as $D_p = \Delta y_{PEI}^2/\Delta t_{PEI}$, where Δy_{PEI} is the particle displacement associated with an eddy and Δt_{PEI} is the time between eddy interactions. Taking $\Delta y_{PEI} = l\triangle Y_{TM}/(2g\beta_p\tau_e\tau_p)$, and $\Delta t_{PEI} = \tau_e$ gives

$$D_p = \left(\frac{l\triangle Y_{TM}}{2g\beta_p\tau_e\tau_p}\right)^2 \frac{1}{\tau_e}, \tag{4.9}$$

that is, $D_p \sim 1/\tau_p^2$ in the trajectory-crossing dominated regime. This result is consistent with Fig. 4.6 (a), where the slope of all the simulation curves on the log-log plot is -2 at large τ_p.

In the high drift velocity trajectory crossing limit, the rate of eddy interactions is more appropriately $1/\theta_{ixn}$. This yields $D_p \sim 1/\tau_p$, and gives D_p essentially the same as that presented by Csanady [41] in the trajectory crossing limit. The $1/\tau_p^2$ dependence of D_p in the Type-I model is a consequence of the ODT eddy rate determining the frequency of dispersion events instead of being dominated by the motion of particles from one eddy to another, which would give the rate $1/\theta_{ixn} = 2g\tau_p/l$. In cases of high trajectory crossing, a rigorous and physically consistent treatment of the fluid-particle interactions would be to use the spatial formulation of ODT in which the ODT line is advanced in the streamwise direction from one spatial location (perpendicular to the ODT line) to another using boundary layer-type equations [16]. In advancing the ODT line, particles or fluid parcels with higher streamwise velocities have lower implied residence times. Nevertheless, the ODT captures the dispersion well for the range of particles studied here.

Besides scaling the eddy interaction time, the parameter β_p also directly influences the particle velocity by scaling the eddy velocity $V_g = \triangle Y_{TM}/(\beta_p\tau_e)$ in Eqs. 4.5 through 4.8. These dual effects complicate the effect of β_p on the particle velocity. Figure 4.8 shows the particle kinetic energy normalized by that of the tracer particles as a function of β_p. Results are shown with and without gravitational body forces. Values are computed at 0.2 s as in Fig. 4.7. Particles are known to act as a low-pass filter [41], following to a lesser degree those motions where $\theta_{ixn} \ll \tau_p$. This suggests that for small fluid time scales corresponding to small $\theta_{ixn} = \beta_p\tau_e$ (or small β_p) particle fluctuations will be reduced with respect to fluid tracer fluctuations. This behavior is observed in Fig. 4.8, where the kinetic energy ratio is small for small β_p and rises toward unity with increasing β_p in the no-gravity simulations.

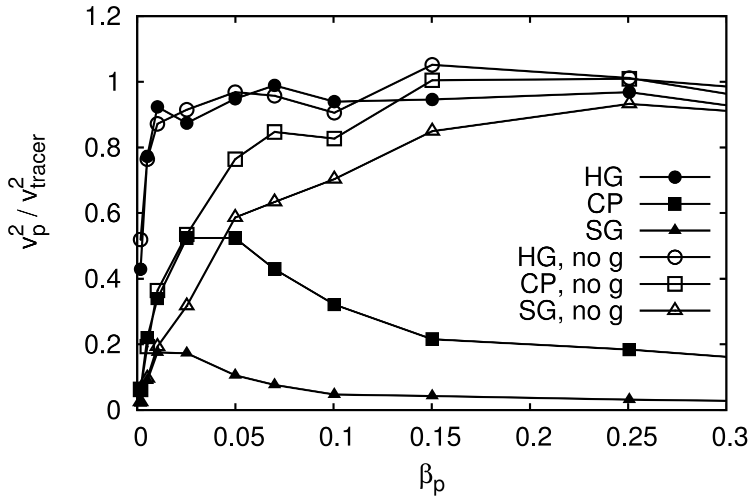

Figure 4.8: Prediction of turbulent kinetic energy of particles in the study of Snyder and Lumley [2] with and without gravitational body forces.

With gravity effects included, similar behavior occurs at small β_p, where the eddy time $(\beta_p \tau_e)$ is small so that increasing β_p increases the interaction time, and hence the kinetic energy ratio. Trajectory crossing is minimal for the smallest β_p, but as β_p further increases trajectory crossing occurs, which limits the interaction time to $\theta_{ixn} = \theta_c = l/2g\tau_p$ even as the eddy time $(\beta_p \tau_e)$ increases. Particles interacting with these longer fluid time scales will see reduced fluctuations because of the reduced interaction time leading to the decay in V_p^2/V_{tracer}^2 for corn pollen and solid glass particles observed in Fig. 4.8 for large β_p. β_p also affects the point where $\theta_c = l/(2g\tau_p) < \beta_p \tau_e$. The peak in the curves (indicating the transition to trajectory crossing) moves to smaller β_b for larger τ_p particles. Note that trajectory crossing is minimal for the HG particles, and the HG curves with and without gravity effects are essentially the same. For $\beta_p = 0.05$ v_p^2/v_{tracer}^2 is significantly reduced for the corn pollen and solid glass as shown in Fig. 4.7.

In the approach of Taylor to fluid and particle dispersion, the product of the velocity fluctuations and the autocorrelation time determine the dispersion. In Fig. 4.9 we plot the Lagrangian particle integral time scale defined from the integral of the particle velocity autocorrelation, computed using V_{ph}, at the dispersion reference time. Figure 4.9 (a) shows predictions plotted versus β_p for hollow glass, corn pollen, and solid glass particles, both with and without body forces. Figure 4.9 (b) shows similar predictions for the autocorrelation versus τ_p for several values of β_p. In

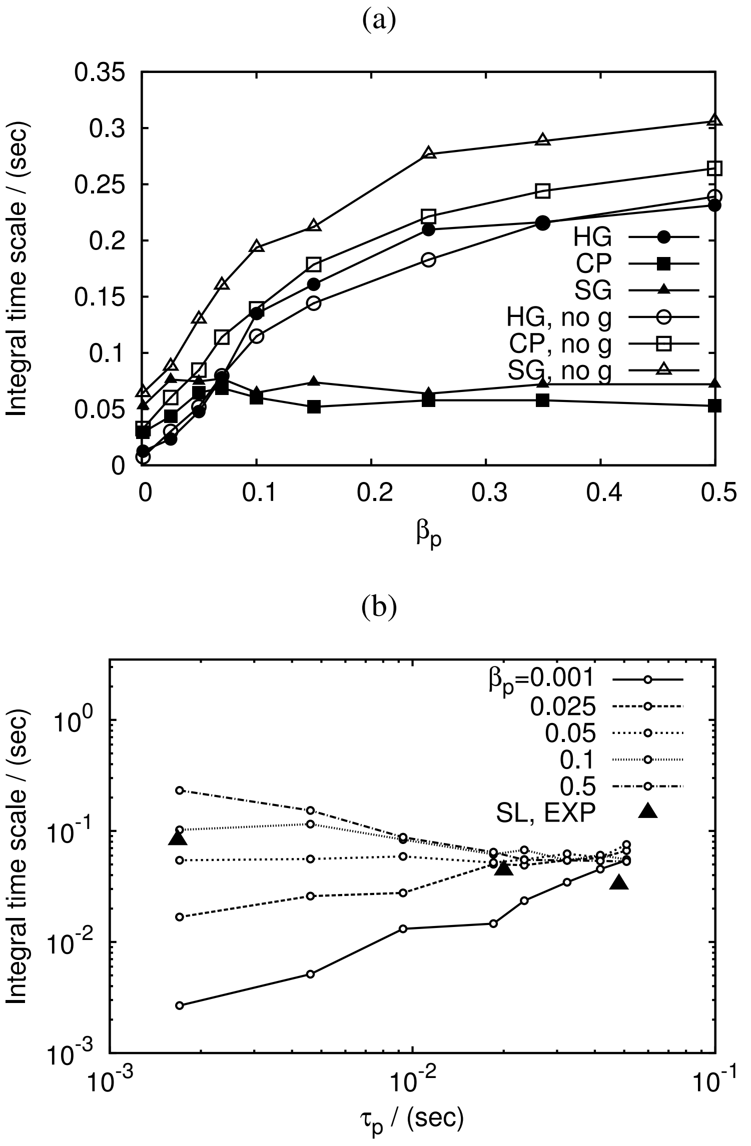

Figure 4.9: Prediction of particle autocorrelation integral time scale as a function of β_p with and without body forces (a), and as a function of τ_p for hollow glass, corn pollen, and solid glass particles with and without body forces at several β_p (b).

the regime where experimental measurements are made, analysis of those measurements suggest that the trajectory crossing effect plays a strong role in reducing the autocorrelation time as the particle time constant increases. Here we show that this behavior depends on the value selected for β_p in ODT particle dispersion.

It is helpful to first refer to the autocorrelation time in the absence of body forces (Fig. 4.9 (a) no-g results). In that case, trajectory crossing is minimal, and it is seen that the autocorrelation time increases with τ_p due to the increased inertia of the particles. Due to the discrete nature of the eddy velocities, when β_p is small this effect is strong: the relative change in the autocorrelation time is dominated by this inertial effect for small β_p. This is true even when body forces are present. Without body forces, Fig. 4.9 (a), when β_p is large, the discrete changes in the eddy velocity are smaller and the fractional change in the interaction time $\beta_p \tau_e$ with β_p is smaller so the relative effects are not as large and the integral timescale changes more slowly with β_p.

With body forces present, at small β_p trajectory crossing is still not significant. In this case, Fig. 4.9 (b) with $\beta_p = 0.001$ shows a clear increase in the autocorrelation time with increasing τ_p due to the inertial effect. At high β_p, the eddy duration $\beta_p \tau_e$ is longer and trajectory crossing may occur when, as noted previously, $\theta_c < \beta_p \tau_e$. As τ_p increases for large β_p (e.g. $\beta_p = 0.5$), the terminal velocity increases, resulting in a shorter interaction time as particles transition from one eddy to another; this causes the observed reduced autocorrelation and integral time scale.

The crossing trajectory dependence on β_p and τ_p is highlighted in Fig. 4.10 (a), which shows the fraction of all eddy interactions that result in particles crossing out of the eddy before the eddy is complete (before $\beta_p \tau_e$). This data is computed for times between 0 and 0.5 relative to the dispersion reference time. In smaller time windows the curve shapes are the same, but slightly shifted as the eddy sizes change relative to the particle timescales (see Fig. 4.5). At low β_p, almost no eddy crossings occur for any particle τ_p. At the highest β_p, particles with $\tau_p > 0.005$ s nearly always cross the eddies. $\beta_p = 0.05$ is strongly transitional, and accounts for the relatively little change in the integral time scale for that β_p in Fig. 4.9 (b). That is, as τ_p increases, there is an approximate cancellation between the inertial effect tending to increase the integral time scale, and the increasing trajectory crossing tending to decrease the integral time scale.

Figure 4.10 (b) shows the crossing fraction versus the quantity $R_{pei,ec} = 2g\tau_e(\beta_p \tau_p)/l$, which is the ratio of the maximum particle-eddy interaction time $\beta_p \tau_e$ to the eddy crossing time

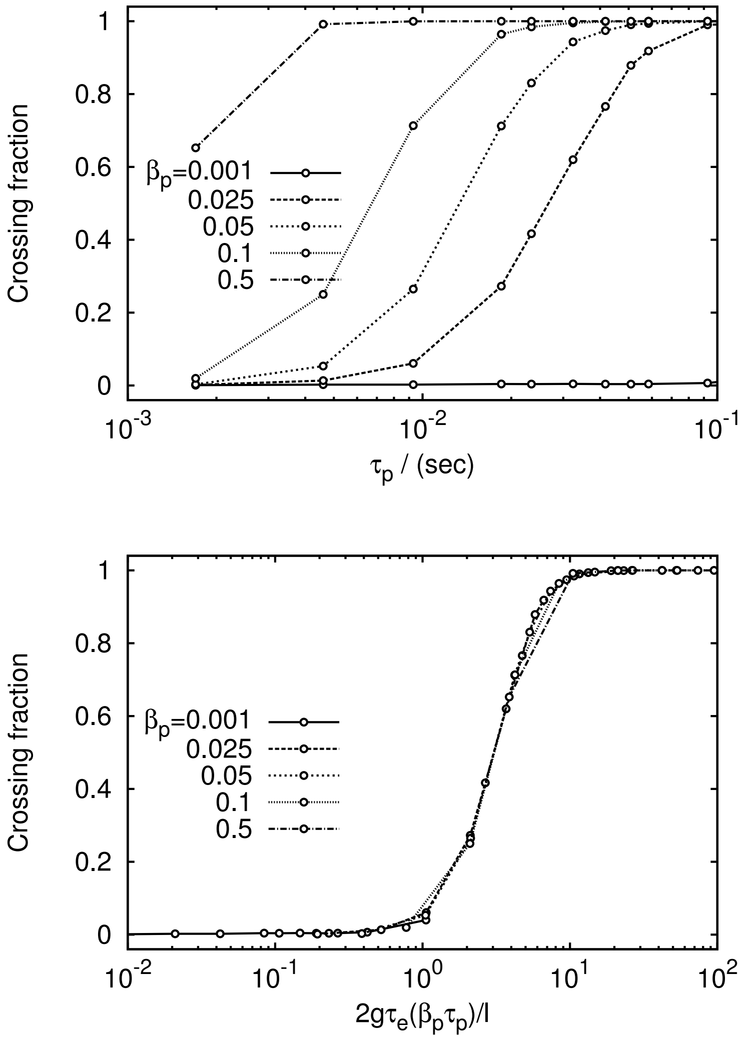

Figure 4.10: Fraction of particle eddy interactions that result in particle crossing before the eddy duration $\beta_p\tau_e$, for several values of β_p.

at the terminal velocity, $\theta_c = l/(2g\tau_p)$, given previously. When the crossing fraction is plotted versus this ratio, the predicted crossing fraction versus time ratio collapses onto a single curve. Here, $\tau_e = 0.95$ s and $l = 4.1$ mm are taken as the average values in time interval from 0 to 0.5 s. Note that the crossing fraction begins to increase sharply when the time ratio is unity, with nearly all particles crossing eddies when the time ratio exceeds ten. Similar to the crossing fraction, the dispersion coefficients shown in Fig. 4.6 (a) depend on the ratio $R_{pei,ec}$ and collapse to a single curve when D_p/D_s plotted versus this ratio. In Fig. 4.6 the abcsissa $\gamma = \tau_p g/u'$ is equivalent to $R_{pei,ec}$ if u' is taken as $l/2\beta_p\tau_e$.

4.5 Conclusions

A Lagrangian particle model, termed a Type-I model, has been implemented and tested using the one-dimensional turbulence model in decaying homogeneous turbulence configurations. ODT has been widely and successfully applied to a number of nonreacting and reacting flows, but only a few studies of multi-phase flows with Lagrangian particles have been attempted. The Type-I model has the advantage of matching the tracer and ballistic particle limits, as well as predicting dispersion for intermediately-sized inertial particles. A single model parameter β_p is introduced in relating the particle interactions to the stochastic ODT eddy events that model turbulent advection. Results were compared to the experiments of Snyder and Lumely [2], and Wells and Stock [3] for a range of particle time constants and body forces. Particle dispersion, dispersion coefficients, velocity statistics, and integral time scales were presented. The ODT model generally performs well and is able to capture the particle inertial effects as well as the trajectory crossing effect. The model parameter β_p scales the eddy time and the eddy gas velocity. The sensitivity of results to this model parameter were presented. The optimal value of β_p was found to be 0.05 in the present study. The particle model was limited to one-way coupling: that is particles affected by the fluid, but not vice-versa. The model has been extended to two-way coupling during both eddy events and gas diffusion processes, allowing for higher particle loadings as will be reported in Chapter 6. The results presented here represent an important validation case for the ODT model from which extensions to other configurations such as jets and reacting flows may be performed.

CHAPTER 5. PARTICLE DISPERSION IN JET FLOW

ODT (one-dimensional turbulence) simulations of particle-carrier gas interactions are performed in the jet flow configuration. The particles with different diameters are injected onto the centerline of a turbulent air jet. Their radial dispersion and axial velocities are obtained as functions of axial position. The time and length scales of the jet are varied through the control of the jet exit velocity and nozzle diameter. Dispersion data at long times of flight for the nozzle diameter ($7\,mm$), particle diameters (60 and 90 μm) and Reynolds numbers ($10,000$ to $30,000$) are analyzed to obtain the Lagrangian particle dispersivity. The above flow statistics of the ODT particle model are compared to experimental measurements. It is shown that the particle tracking method is capable of yielding Lagrangian prediction of the dispersive transport of particles in a round jet. In this chapter, three particle models (Type-I, -C, and -IC) introduced in Chapter 3 are presented to examine the details of particle dispersion and particle-eddy interaction in jet flow. These results appear in much the same form as the recent paper submitted to *Physics of Fluid* by G. Sun et al in 2015.

5.1 Introduction

Particle and droplet dispersion in turbulent jet flows is an essential part of many important industrial processes. Typical examples include the dispersion of liquid fuel droplets in gas combustors and the mixing of coal particles by the input jets of coal-fired power plants. The dispersion of the particles largely determines the efficiency and the stability of these processes.

Many computational studies on gas-particle turbulent round jets have been performed. Direct numerical simulations (DNS) have been used to study gas-particle jets at low Reynolds numbers [24, 96]. However, DNS for a high Reynolds number flow is not computationally efficient. Therefore, simulation approaches are required that do not resolve all flow scales in three dimensions. Many gas-particle flows have been studied in which the subgrid-scale turbulence is calculated using large eddy simulation (LES) [34, 97]. Those LES provide good means to capture unsteady physical features in the turbulence. The accuracy and the reliability of LES predictions depend on several factors, such as the accurate modeling of the subgrid-scale phase interactions.

A promising alternative approach is the one-dimensional turbulence (ODT) model, which is able to resolve the full range of length scales on a one-dimensional domain that is evolved at the finest time scales [7, 8]. ODT has been applied in flow configurations such as homogeneous turbulent flow, shear-driven flow (channels, jets), and buoyancy-driven flow (plumes), etc. It has been proven to be a successful model of many different kinds of shear-dominated nonreacting [7–9] and reacting flows [10–12, 14, 16, 72].

John Schmidt et al. extended ODT model to the prediction of particle velocity statistics in turbulent channel flow [4]. In Chapter 3, one version of the ODT multiphase interaction model using an instantaneous (referred to as Type-I) particle-eddy interaction (PEI) model was presented to investigate particle transport and crossing trajectory effects in homogeneous turbulence [5]. Here, as an extension of the study, two new PEI models are used in the present ODT multiphase model to analyze the behavior of individual particles in round jets at high Reynolds numbers (*Re*). One of the models applies continuous PEI (referred to as Type-C) and the other combines instantaneous and continuous interaction features (referred to as Type-IC).

The remainder of this chapter is organized as follow: first, some details of of the model used are presented for the present work followed by a detailed discussion of the prediction results of Type-I, -C and -IC models, including the experimental validations. Finally, the paper is completed by a summary and some concluding remarks.

5.2 Numerical description

The transverse y-direction, which is the direction of the main significant gradients, is considered here as the ODT domain. The parameter values used in this chapter are 16 and 50 for C and Z, respectively. The elapsed time method for large eddy suppression is incorporated with $\beta = 0.4$. The same set of equations described in Sec. 3.1.1 are solved with the transformation procedure of turbulent advection described in Sec. 3.1.2. In the jet flow, the particle motion is determined by the drag force and gravity, which are expressed in Eq. 3.29. The particle-eddy interactions of Type-I, -C, and -IC are described in detail in Sec. 3.2.2, 3.2.3, and 3.2.5.

5.3 Turbulent jet configuration

5.3.1 Experimental details

In this chapter the turbulent dispersion of particles in shear-dominated turbulent flows is studied. Measurements of particle dispersion in round turbulent jets was studied by Kennedy and Moody [98]. These measurements span a range of Reynolds and Stokes, which were obtained by varying the jet velocity, nozzle diameter, and particle diameter. Reynolds numbers based on the jet velocity (air) range from $10,000$ to $30,000$. Fully developed turbulent flow conditions at the nozzle exit are used. Hexadecane droplets with number average diameters of 60 and 90 μm are used for the study. Mean particle density is 4990 kg/m^3. Monodisperse particles were generated in the experiments with a size uncertainty of ± 2 μm [98]. The air used in the jet is at room temperature and pressure and thus the particles are essentially non-vaporizing. The particle loading is small with more than 1000 droplet diameters separating particles so that particles do not alter the fluid velocity, nor do they modulate the turbulence; this was verified by the measurements of Kennedy et al [98].

5.3.2 Simulation details

The ODT simulations are carried out in a temporally evolving planar shear layer configuration. This configuration has characteristics similar to those of a spatially evolving round jet [99]. To compare the temporal evolution with the spatial experimental measurements, a convective velocity, $U_m(t)$, is required to transform the evolution time (t) to the streamwise spatial coordinate (x), which is obtained from the ratio of the momentum flux, $\dot{M}$, to the mass flux, $\dot{m}$,

$$U_m(t) - U_\infty = \frac{\dot{M}}{\dot{m}} = \frac{\int_{-\infty}^{\infty} \rho (u(y,t) - U_\infty)^2 dy}{\int_{-\infty}^{\infty} \rho (u(y,t) - U_\infty) dy}, \tag{5.1}$$

where U_∞ is axial velocity of gas phase far from the jet (0 in this study) [11]. In particular, the Reynolds number is constant since the length scale increases in proportion to the velocity fluctuation decay. The similarity scaling of temporal turbulent planar and round jets is illustrated by constant-density momentum scaling [100]. It suggests that the temporal planar jet is comparable to spatial round jet in that both exhibit a constant Reynolds number as the flow evolves.

Table 5.1: Initial conditions of gas phase and particle phase (60 and 90 μm) and particle Stokes number in the 7 mm jet.

	$Re = 10,000$	$Re = 20,000$	$Re = 30,000$
U_{g0}	21.5 m/s	43 m/s	64.5 m/s
U_{p0} $(60\,\mu m)$	17.5 m/s	30 m/s	46 m/s
St $(60\,\mu m)$	26	53	77
U_{p0} $(90\,\mu m)$	15 m/s	32 m/s	51.5 m/s
St $(90\,\mu m)$	61	122	178

The initial gas velocity conditions for the turbulent planar jet, U_{g0}, are given in Table 5.1 as a function of the Reynolds number and the jet exit diameter, D. The streamwise velocity at the inlet is specified using the following hyperbolic tangent function to smoothly transition the velocity in the radial direction and is shown schematically in Fig. 5.1,

$$U_g(y) = \frac{A}{2}\left(1+\tanh\left(\frac{y-L_1}{w_l}\right)\left(1-\frac{1}{2}\left(1+\tanh\left(\frac{y-L_2}{w_l}\right)\right)\right)\right), \tag{5.2}$$

where A is the velocity amplitude, w_l is the transition boundary layer width, and L_1 and L_2 are the middle position of the transitions. Particles with different diameters are injected into the centerline of the jets. The simulation domain width is $40D$ and the ODT model evolves for 0.11 s for all the cases; this is approximately 70 x/D. The initial temporal resolution is 0.2 μs, the initial spatial resolution is 50 μm, and an adaptive meshing algorithm is used, which refines the mesh as fluctuations cascade to smaller length scales and reduces resolution as these fluctuations are dissipated. The initial conditions for the dispersed phase are given in Table 5.1, in which the initial particle axial velocity along the centerline is extrapolated from experimental results. The results reported here are collected over 512 ODT realizations, which is enough to provide stationary statistics.

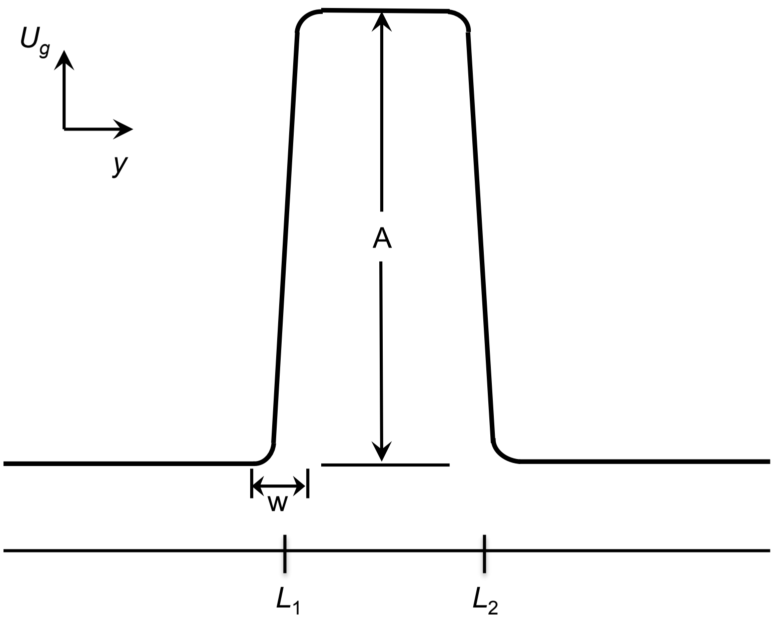

Figure 5.1: Schematic of the tanh profile used to specify the initial streamwise velocity profile.

5.4 Results and discussion

5.4.1 Jet evolution

In order to compare particle results between our ODT results and experimental data, it is first necessary to compare the gas-phase flow characteristics. The ODT-predicted streamwise velocity evolution at the centerline is compared with experimental measurements in Fig. 5.2. The mean axial velocities, U_c, are normalized by the jet exit velocity U_{g0}; the turbulence intensities, U_{crms}, are normalized by U_c; and the position is normalized by the jet exit diameter D. The decay of U_c and the asymptotic level of U_{crms} are typical of free turbulent jets. Overall, the numerical results agree well with experimental data. The ODT exhibits a Reynolds number similarity while the measurements exhibit some Reynolds number dependence as shown in the figure. This may be indicative of some differences in the development of turbulence and boundary layers within the jet nozzle; we have not attempted to correct for this in the ODT simulations.

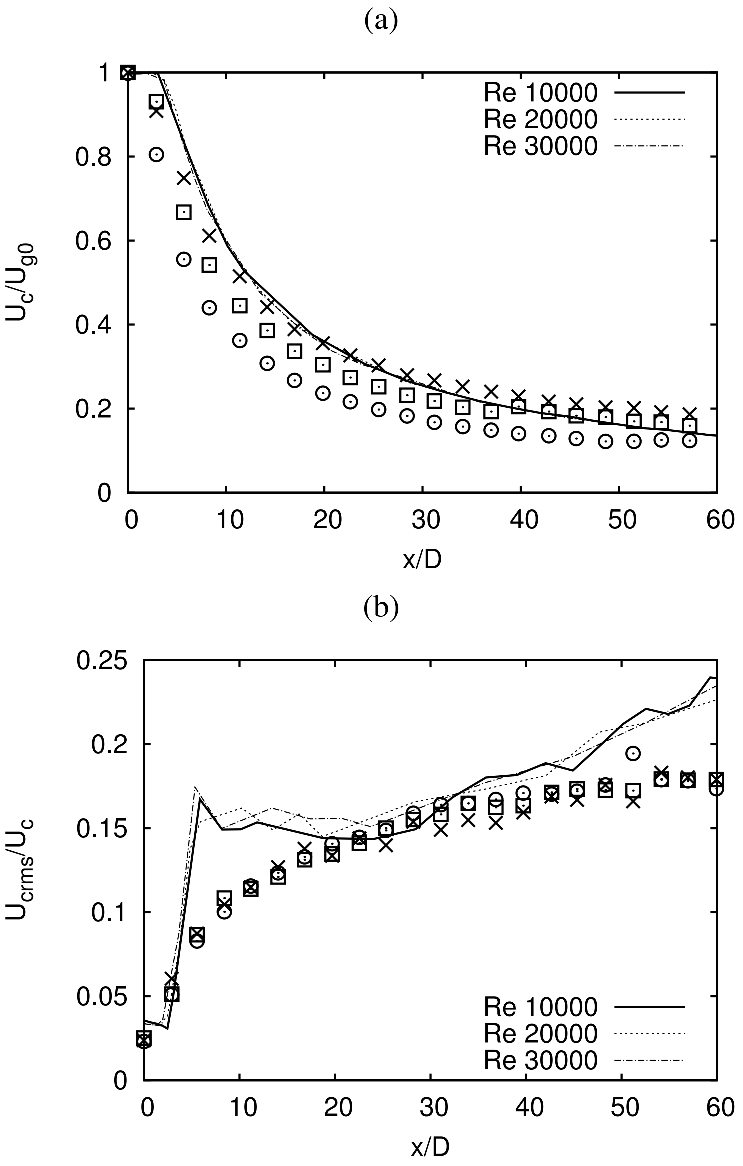

Figure 5.2: Normalized mean axial velocity (a) and turbulence intensity (b) along the jet centerline. Lines represent ODT predictions. Experimental measurements are represented by Cross points ($Re = 10,000$), square points ($Re = 20,000$), circular points ($Re = 30,000$).

5.4.2 Particle phase

The results of particle transport are presented in this section, specifically, ODT and experimental results for a turbulent multiphase round jet are compared. A detailed analysis is conducted to assess the performance of the three ODT multiphase interaction models described in Sec. 3.2. In this chapter, the β_p value used in the jet flow for all the interaction models is 0.08.

The particles have instantaneous displacements during the Type-I interaction with the eddies. The dispersion of particles is predicted for nonzero gravity ($g = 9.8m/s^2$) as a function of normalized axial location x/D. Figure 5.3 compares the dispersion data for ODT cases of 60 μm and 90 μm particles to experimental measurements for $Re = 10,000$, $20,000$ and $30,000$ using Type-I interaction model. The particle dispersion increases with the jet evolution. Heavy particles disperse less, which ODT Type-I interaction model provides good qualitative predictions to. In the upstream part of jet ($x/D = 0 - 30$), the particles are scarcely affected by the fluid flow, due to a lack of large eddy structure. As the large eddies that account for the bulk of the spreading appear later, the particles are transported away from the center of the jet, resulting in non-uniform particle dispersion patterns. The particle movement in the jet is strongly influenced by the size of eddies and consequently the response time of the particles. The representative eddy map of the flow field is shown in Fig. 5.4(a). The particles in the low *Re* case have high dispersions because they travel slowly through the jet and thereby interact with more eddies due to low initial velocities of particles. This is related to the crossing trajectory effect, that arises when the particle are not acted upon for as long as a given eddy lifetime [5, 37, 40]. The difference of the dispersions of 60 and 90 μm particles is greater in the low *Re* jet compared to the high *Re* jet at a given axial location. The Stokes number of the large particles is big so that it takes a long time to adjust to the flow and hence leads to less dispersion. As shown in Table 5.1, the particles of given size have high Stokes number in high *Re* jet, and their dispersion is small. Table 5.1 also shows that for two particle sizes, their relative difference in Stokes number is nearly the same in the different jets. However, this similarity does not result in the similarity in the dispersion as noted above. This is because in spite of similar relative difference, the magnitude of the particle Stokes number is large in the high *Re* jet that leads to less overall dispersion. Thus, less difference in the dispersion of two particles exists in the faster jet.

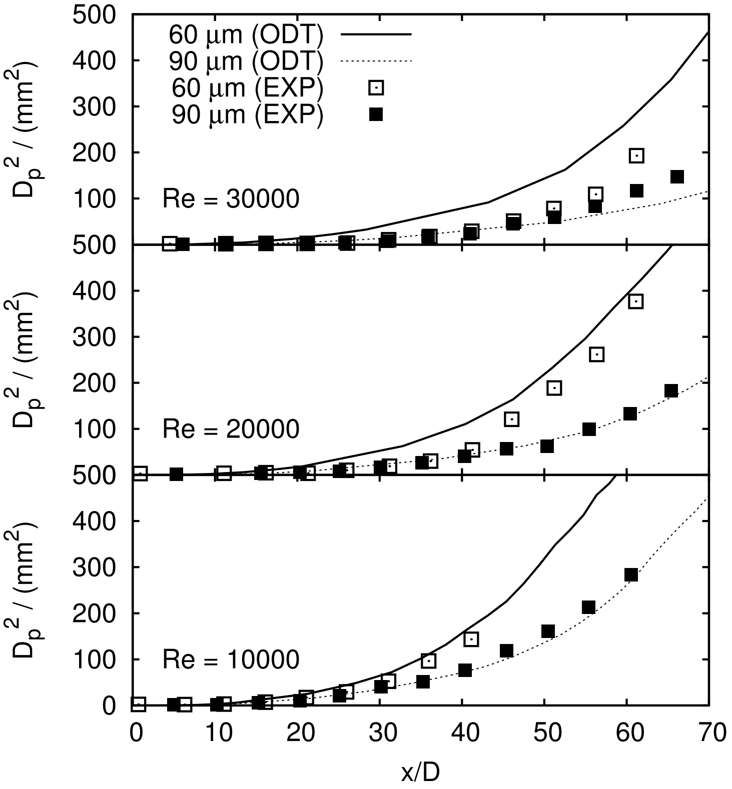

Figure 5.3: Type-I dispersion of $60\,\mu m$ and $90\,\mu m$ particles in the $7\,mm$ jet with $Re = 10{,}000$, $20{,}000$ and $30{,}000$.

Figure 5.5 shows the mean axial velocity along the centerline of particles of two sizes in the three different *Re* jet at different axial positions. Overall, there is a good agreement between numerical and experimental results. Initially the particles are injected at a lower velocity than the fluid. At the nozzle exit the particles tend to accelerate to catch up to the air and then their velocity decreases due to momentum exchange as the particles relax to the decaying gas velocity. The differences between ODT and experimental results are due to the combination of modeling deviation and the uncertainty in the inlet gas conditions related to turbulence development. Another possible reason is that in the experiment, the particles might be injected early and have equilibrated with the fluid before they reach the nozzle exit. If so, the extrapolated initial particle velocities used in the simulations are likely to introduce some deviation.

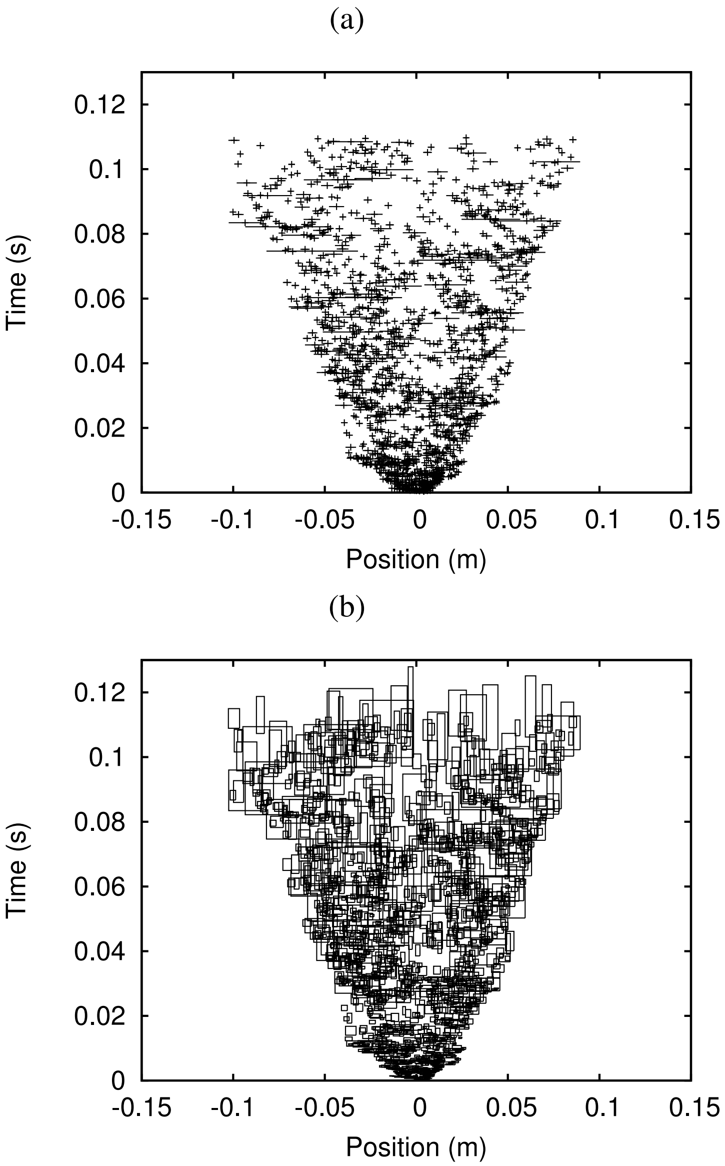

Figure 5.4: Maps of eddy sizes, locations, and occurrence times for representative ODT realizations for jet flow. Plot (a) shows instantaneous eddy locations for a Type-I interaction; plot (b) shows eddy “box” extents for a Type-C interaction.

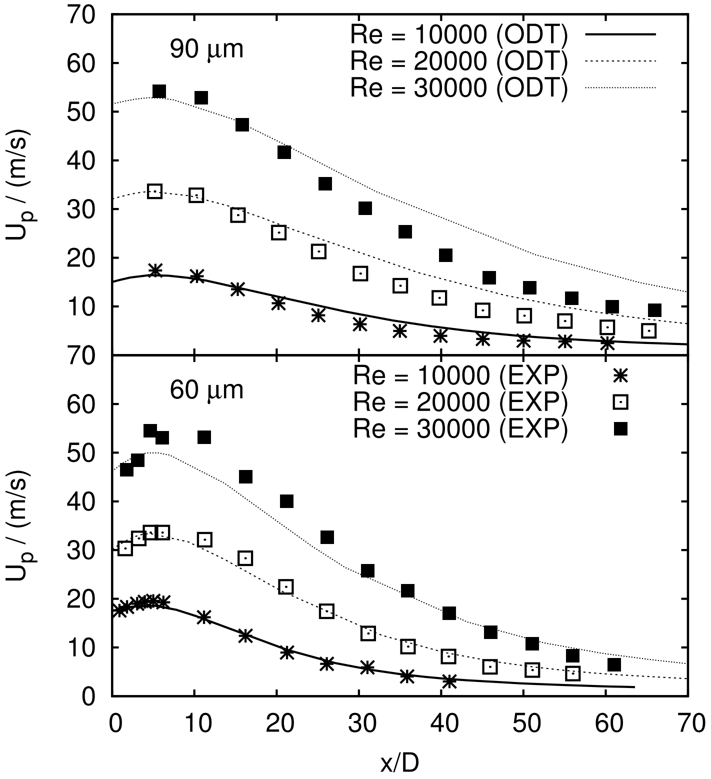

Figure 5.5: Type-I mean streamwise velocities of $60\,\mu m$ and $90\,\mu m$ particles in the $7\,mm$ jet.

In generally, the particle dispersion is largely determined by the inertial response time of the particles, which is measured by the Stokes number. The particles of small Stokes number ($St < 1$) are carried by the fluid around the flow field. Since small particles respond quickly to the change of fluid motions, they can follow the fluid closely, which lead to particle dispersion patterns closely resembling the fluid eddy structures. In other words, particles with very small Stokes numbers are in a quasi-equilibrium with the fluid, as were the hollow glass particles studied in the previous homogeneous turbulence case in Chapter 4 [5]. In contrast, particles with moderate Stokes number (e.g. $60\,\mu m$ and $90\,\mu m$ particles in current study) tend to move around the eddy edges because of the effects of flow field strain. For the high Stokes number case ($St > 100$, not shown here), the general dispersion pattern is similar to that of the medium Stokes number cases. However, since the particles are so slow to respond and follow the fluid motion, even the motion of large eddy structures does not disturb the particles. Consequently, the particles could even cross the eddy regions due to their large inertia.

The particles interact with the eddies in the continuous way in the Type-C model. The eddies in the Type-C interactions are not instantaneous, but exists for the finite time as shown in Fig. 5.4(b). The overlapping regions of eddy boxes in the figure suggest the possibility of particle interactions with multiple active eddies simultaneously. Figure 5.6 shows the comparison of the particle dispersion predicted by the Type-C interaction model to experimental measurement, in which the model provides decent quantitative prediction in the jet of $Re = 10,000$, $20,000$, and $30,000$. It is important to note that the Type-C model is shown to be able to predict the moderate and high Stokes particles (e.g. 90 μm particles in $Re = 20,000$ and $30,000$ jet); however, it underpredicts the dispersion of small Stokes particles (e.g. 60 μm particles and even 90 μm particles in $Re = 10,000$ jet) due to “real-time” interaction as described in Sec. 3.2. The numerical results of axial velocities of the particles simulated by the Type-C model shown in Fig. 5.7 and are similar to Fig. 5.5 within a 5% difference.

Here we go beyond the experiment and further examine the Type-C interactions. Figure 5.8 compares the dispersion of tracer fluid particles to “quasi” tracer particle in the case of $Re = 30,000$. The “quasi” tracer particle is defined to have the same properties as hollow glass particle in previous homogeneous turbulence study in Chapter 4 [5]. It turns out that the Type-C model underpredicts the tracer limit because of the “delayed” dispersive motion of small Stokes particles in contrast to tracer or fluid particle. Figure 5.9 shows the comparison of the Type-I and Type-C interaction models for the dispersion of $60\,\mu m$ and $90\,\mu m$ particles in the $Re = 10,000$ jet. The Type-I model gives higher prediction to particle dispersion than the Type-C interaction in that the interactions merely occur at the birth of the eddies and disperse the particles, thus enabling the particles to move earlier. This is consistent with the interaction nature introduced in Fig. 3.5. The large particles tend to keep their velocity and therefore their dispersions are independent of PEI type during the early stage of jet evolution in which the eddy time scales τ_e are small. With the increase of τ_e to the order of magnitude of the inertial response time of large particles, the large particles show different dispersive behaviors in the two different interaction models. In contrast, the small particles adjust to local jet velocities quickly, which leads to significantly different dispersions since they are inserted in the jet.

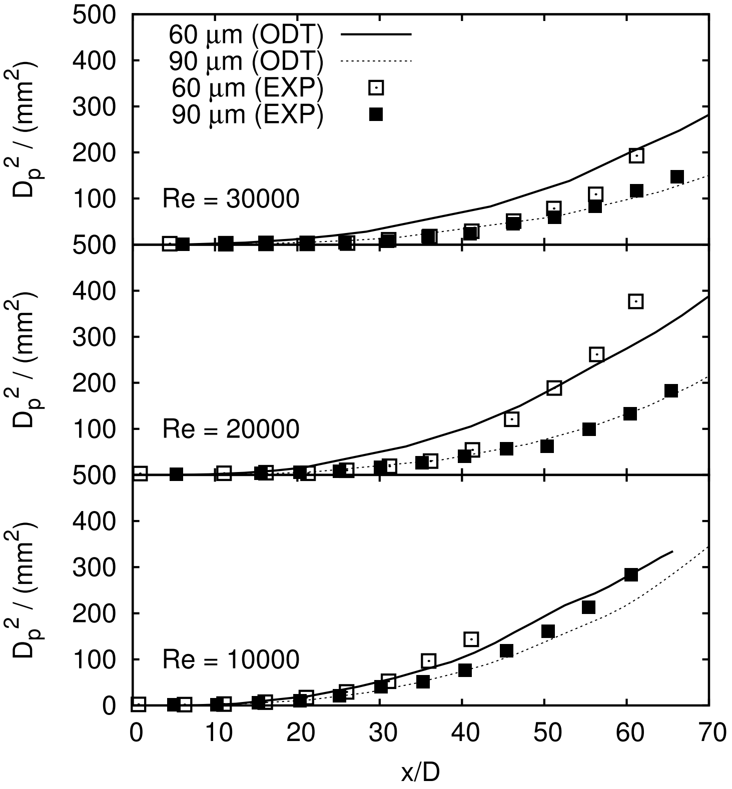

Figure 5.6: Type-C dispersion of $60\,\mu m$ and $90\,\mu m$ particles in the $7\,mm$ jet with $Re = 10,000$, $20,000$ and $30,000$.

As described in Sec. 3.2, the Type-IC is considered to be the most robust PEI model in that it not only allows the particles to interact with multiple eddies at the same time but also matches the tracer limit. Figure 5.10 shows the comparison between experimental and simulation values of particle dispersion in the $7\,mm$ jet using the Type-IC model that reproduces the experimental results. The prediction of particle axial velocities by the Type-IC model will not be shown here because its comparison to experimental measurements is within 5% difference of the results of the Type-I model, shown in Fig. 5.5. The similarity between the Type-I and Type-IC models is due to the relatively low line-directed particle velocity. The line directed particle velocity is due to the turbulent advection, precluding strong transverse eddy trajectory crossing effects. The tracer dispersion is also well predicted by the Type-IC model with the combined instantaneous and

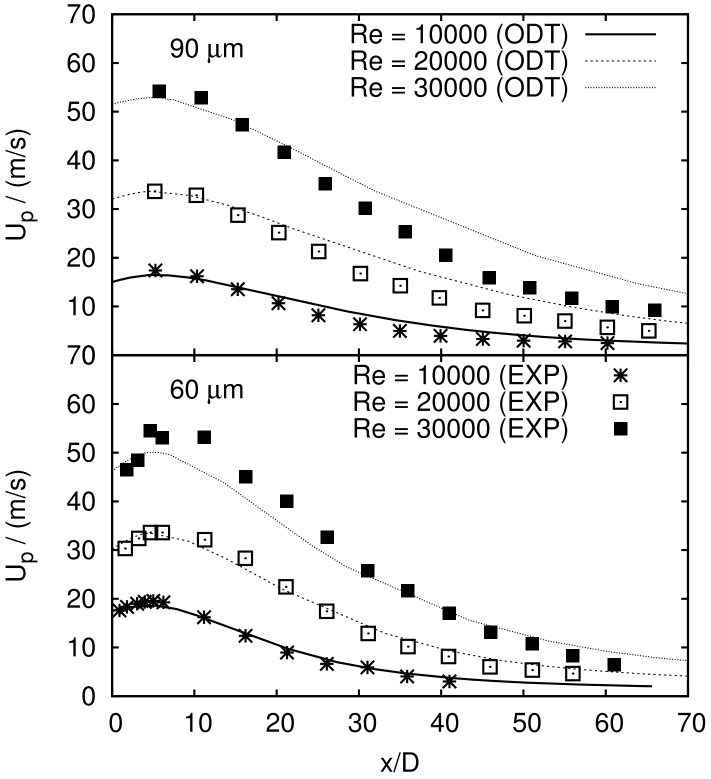

Figure 5.7: Type-C mean streamwise velocities of 60μm and 90μm particles in the 7mm jet.

continuous interactions. This is shown in Fig. 5.11, where the comparison of the radial dispersion of "quasi" tracer particles and tracer particles in the 7mm jet for $Re = 10,000$ are plotted. This comparison represents a validation of the correct model behavior.

The ODT simulation results for particle dispersion predicted by three PEI models are presented in Lagrangian form in Fig. 5.12, 5.13 and 5.14. For the short times-of-flight, the particle dispersion behaves as a quadratic function; it becomes linear with time for long times-of-flight [101]. Similar to the previous Eulerian predictions, small particles respond to the fluid quickly and reach high velocities in shorter times than large particles, thereby dispersing faster in the jet flow of given *Re*. The Type-I and Type-IC models give similar reasonable predictions, while the Type-C model underpredicts the turbulent dispersions of the $Re = 10,000$ and $20,000$ cases because of the poor prediction of the low Stokes particles. It can be observed that at low *Re* number, the exit velocities

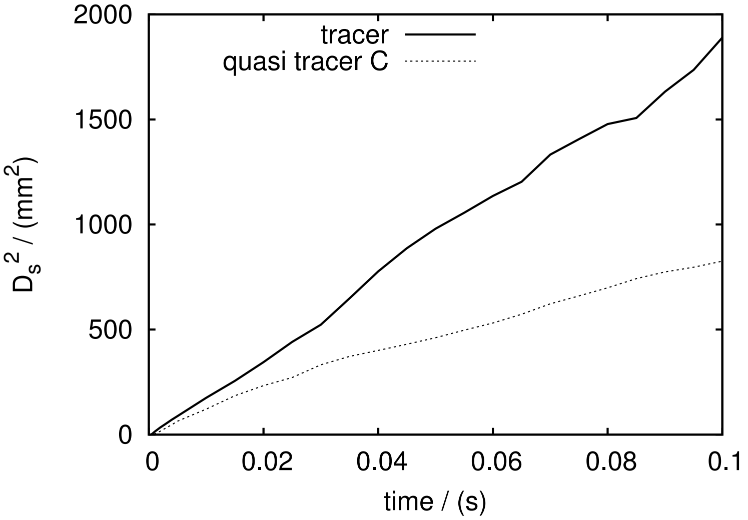

Figure 5.8: Comparison of Lagrangian dispersion of tracer particle and “quasi” tracer predicted by the Type-C model in the $7\,mm$ jet and $Re = 30,000$.

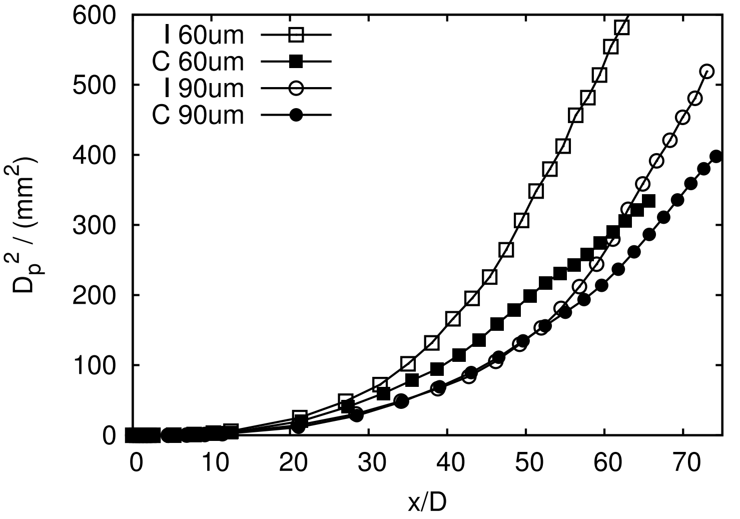

Figure 5.9: Comparison between the dispersion of $60\,\mu m$ and $90\,\mu m$ particles in the $7\,mm$ jet for $Re = 10,000$ predicted by the Type-I and Type-C models.

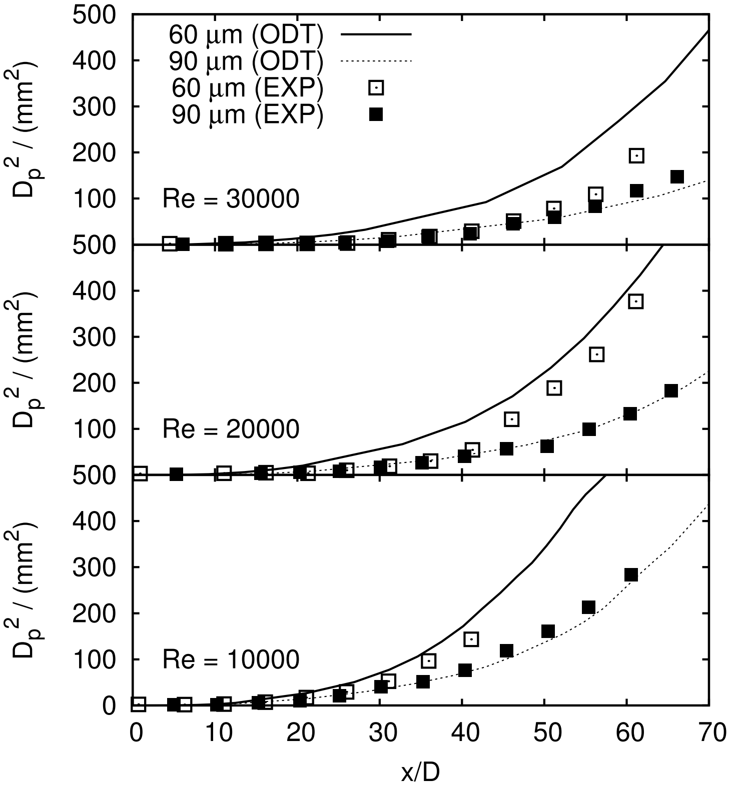

Figure 5.10: Type-IC dispersion of $60\,\mu m$ and $90\,\mu m$ particles in the $7\,mm$ jet with $Re = 10,000$, $20,000$ and $Re = 30,000$.

of the particles are relatively low, whereas in the high *Re* jet, the particles experience the short quadratic region and behave like the ballistic-limit due to high local Stokes number even if the velocities of the surrounding gas phase drops. Lagrangian particle dispersivity, D_L, can be defined as

$$D_L = \frac{1}{2}\frac{dD_p^2}{dt} = \frac{1}{2}\frac{d}{dt}\langle D_p(t)D_p(t)\rangle, \tag{5.3}$$

where D_p is the radial particle displacement. The particle dispersivity is estimated in the linear portion of the Lagrangian dispersion curves by using a least-squares fit. Table 5.2 compares ODT simulation results of D_L to the values reported in Kennedy's study [98] at $Re = 20,000$ and $30,000$. D_L increases with increasing Reynolds number. Taylor's theory [101] shows that the mean-square dispersion of fluid particle in a stationary homogeneous turbulence is a quadratic function of evo-

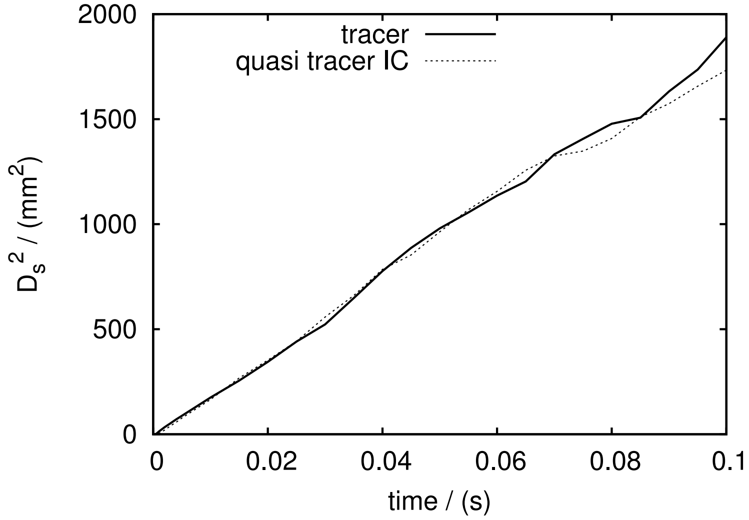

Figure 5.11: Comparison of Lagrangian dispersion of tracer particle and "quasi" tracer predicted by the Type-IC model in the $7\,mm$ jet and $Re = 30,000$.

Table 5.2: Particle dispersivity ($60\,\mu m$ and $90\,\mu m$) in the $7\,mm$ jet.

	Re	Exp	Type-I	Type-C	Type-IC
$60\ \mu m$	20,000	0.0079	0.0067	0.0039	0.0069
	30,000	0.010	0.0095	0.0053	0.0111
$90\ \mu m$	20,000		0.0066	0.0037	0.0068
	30,000		0.0106	0.0063	0.0103

lution time and behaves linear with time for long times-of-flight. Batchelor [102] analyzed the transport of the fluid particle in the shear flow and showed that the dispersion increases linearly with time and the diffusivity keeps constant. However, a Stokes number particle is not expected to have the similar behavior as a fluid particle due to its finite inertia. As discussed before, the Stokes number of inertial particles determined whether they respond to the fluctuations of the surrounding flows. The particle would eventually tend to respond to all the velocity fluctuation of the gas phase when the local particle Stokes number is $O(1)$. Both ODT simulations and experimental measurements suggest that the 60 μm and 90 μm particles have the apparent linear region after about 0.02 and 0.03 seconds, respectively, since then they achieve a Stokes number of $O(1)$.

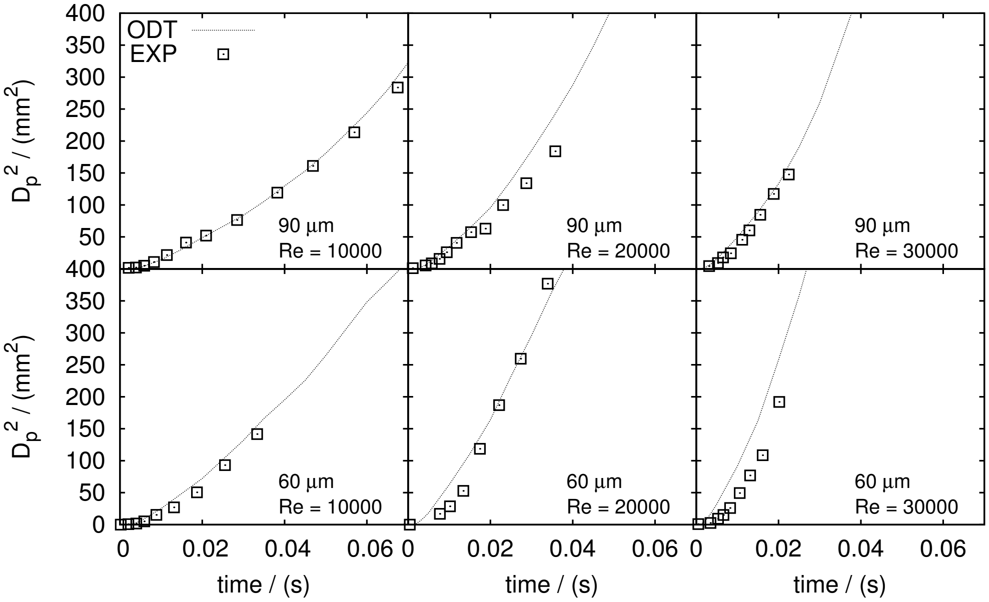

Figure 5.12: Lagrangian dispersion of 60 μm and 90 μm particles predicted by the Type-I model in the 7 mm jet.

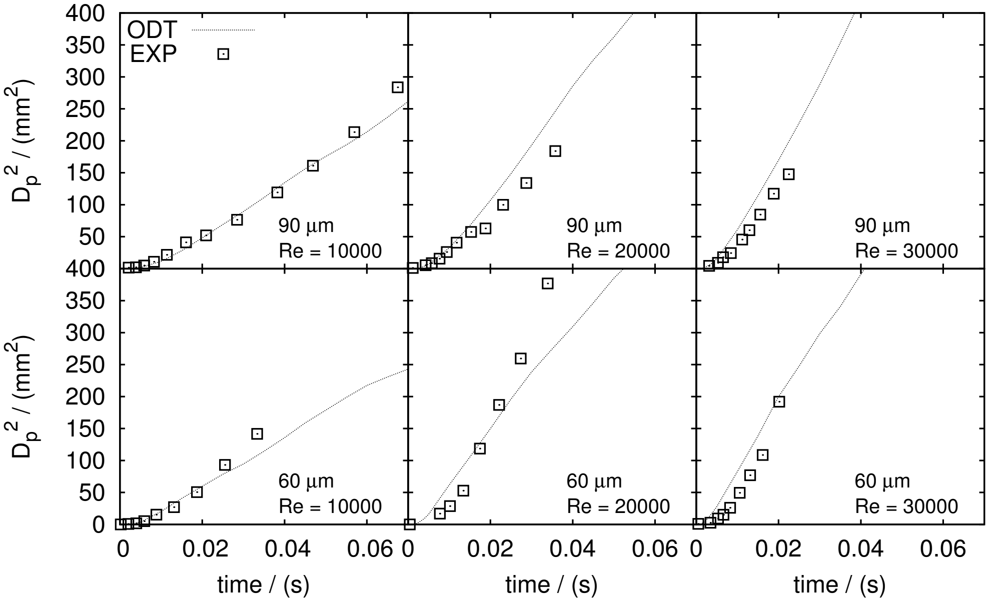

Figure 5.13: Lagrangian dispersion of 60 μm and 90 μm particles predicted by the Type-C model in the 7 mm jet.

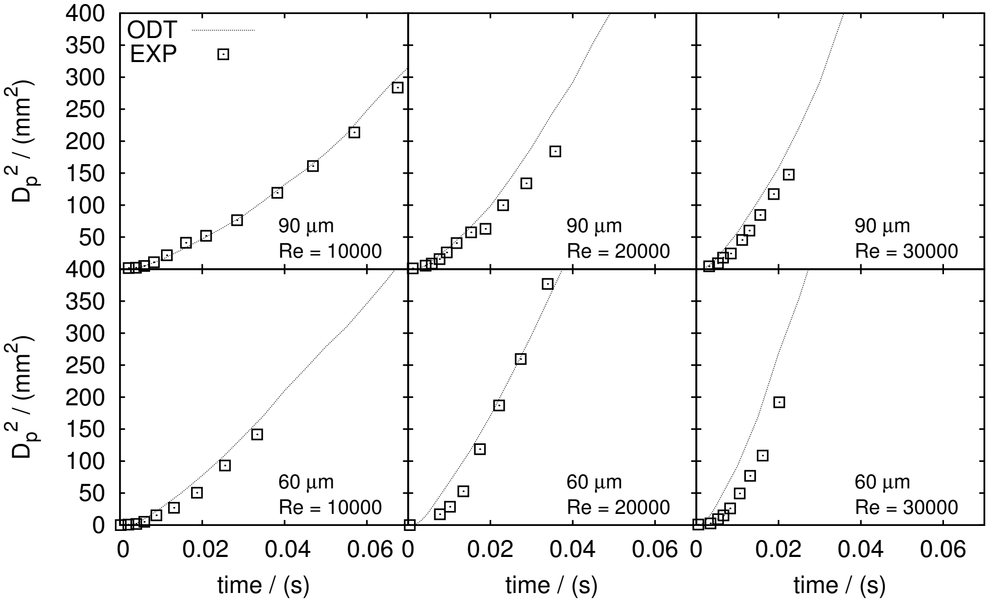

Figure 5.14: Lagrangian dispersion of $60\,\mu m$ and $90\,\mu m$ particles predicted by the Type-IC model in the $7\,mm$ jet.

5.4.3 Parameter sensitivity analysis

Previous studies [11, 16] of parameter sensitivity of ODT parameters C, Z and β have formed the basis for parameter selection. In order to investigate the crossing trajectory effect of the particles in the homogeneous turbulence, we conducted parameter analysis of β_p that relates the turbulence characteristics to the particle-eddy interaction time [5].

In this section, the sensitivity analysis is performed to establish a common basis on which β_p can be estimated for particle behavior in shear flow. The analysis is important to guide the future developments and extended applications of the ODT multiphase models. The particle parameter β_p determines the magnitude of the particle-eddy interaction in the ODT turbulence. High values of β_p lead to possibly high interaction time by increasing the maximum interaction time scale $\beta_p \tau_e$ and reducing the eddy velocity, $\triangle Y_{TM}/(\beta_p \tau_e)$, felt by the particles during interactions. On the other hand, when β_p is low, the particles are more likely to interact with "fast" eddies for shorter times. Thus, two competing interaction effects on the particles are controlled by β_p simultaneously.

Figure 5.15, 5.16 and 5.17 show β_p sensitivity on the dispersions of 60 μm and 90 μm particles in the $7\,mm$ jet for $Re = 10,000$, $20,000$ and $30,000$ predicted by the Type-I, -C and -IC interaction models. Five β_p values are chosen, that is, 0.02, 0.04, 0.06, 0.08 and 0.1, which are in similar range to ones used in the homogeneous turbulence study in Chapter 4 [5]. Apparently, the simulations using $\beta_p = 0.08$ give the best predictions to experimental data. The ODT parameters values are $C = 16$, $Z = 50$ and $\beta = 0.4$ for all the ODT simulations, each of which consists of 512 realizations.

All eighteen cases show the same β_p sensitivity on particle dispersion in the shear flow. The particle dispersion decreases as β_p increases. That suggests that even though the eddy time scale $t_e = \beta_p \tau_e$ increases, the crossing trajectory effect plays a role in limiting the interaction time $T_{ixn} = l/2g\tau_p$, that is less than t_e. However, because of their short relaxation times, the small light particles easily adapt to the fluid fluctuations and tend to interact with the eddies for a longer time. It turns out that their dispersions are not largly subject to the crossing trajectory effect. Therefore, altough the crossing trajectory effect is still dominant in the particle-eddy interactions, the large β_p enhances the overall interaction time for small particles. In contrast to the large heavy particles, the dispersion of the small light particles reduces less with the increase of β_p. For the given particle size, the particle dispersions in the high Re case tend to decrease faster when the value of β_p becomes larger. This is attribute to the fact that fast fluid helps the particles cross out the eddies early.

In order to illustrate the comparison of the β_p sensitivity in a direct way, a spreading parameter S_β at given x/D is defined as

$$S_\beta(\beta_{p,1}, \beta_{p,2}) = \frac{D_{p,\beta_{p,1}} - D_{p,\beta_{p,2}}}{D_{p,\beta_{p,3}}} / \frac{\beta_{p,2} - \beta_{p,1}}{\beta_{p,3}}, \tag{5.4}$$

where D_p represents the particle dispersion, and $\beta_{p,3}$ is the average value of $\beta_{p,1}$ and $\beta_{p,2}$. Large S_β indicates high sensitivity of particle dispersion to β_p. Figure 5.18 shows $S(0.02, 0.1)$ spreading at $x/D = 50$ as a function of Re for three different interaction models. The dispersion is more sensitive to β_p in that the crossing trajectory effect is important. The similar effect has been observed in the previous study of multiphase homogeneous turbulence in Chapter 4 as well [5]. In addition, the findings of the β_p effect on particle disperison discussed in the last paragraph are

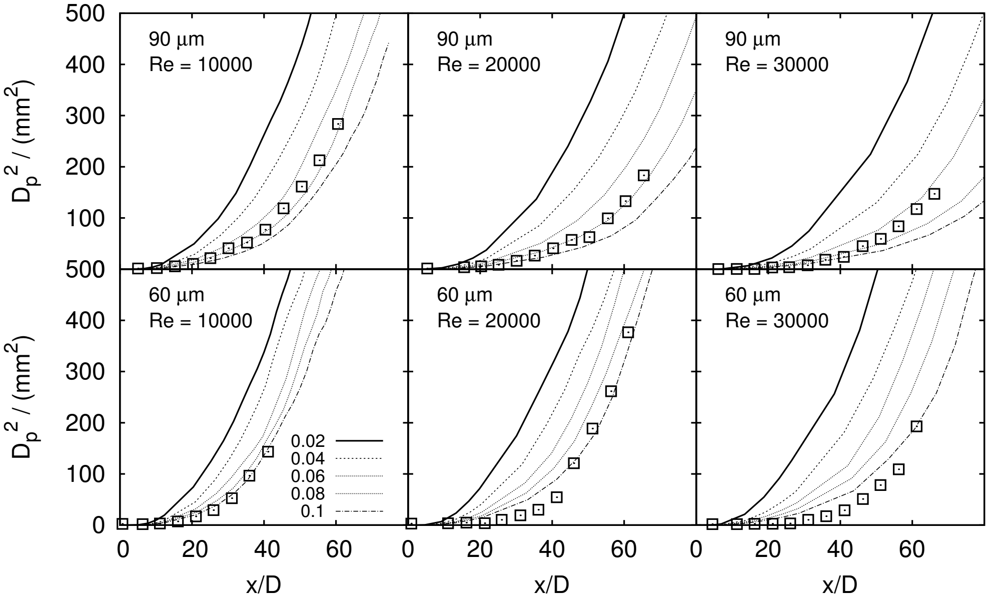

Figure 5.15: β_p sensitivity on the Type-I dispersion of 60 μm and 90 μm particles in the 7 mm jet with Re = 10,000, 20,000 and 30,000. Square symbols represent experimental measurements.

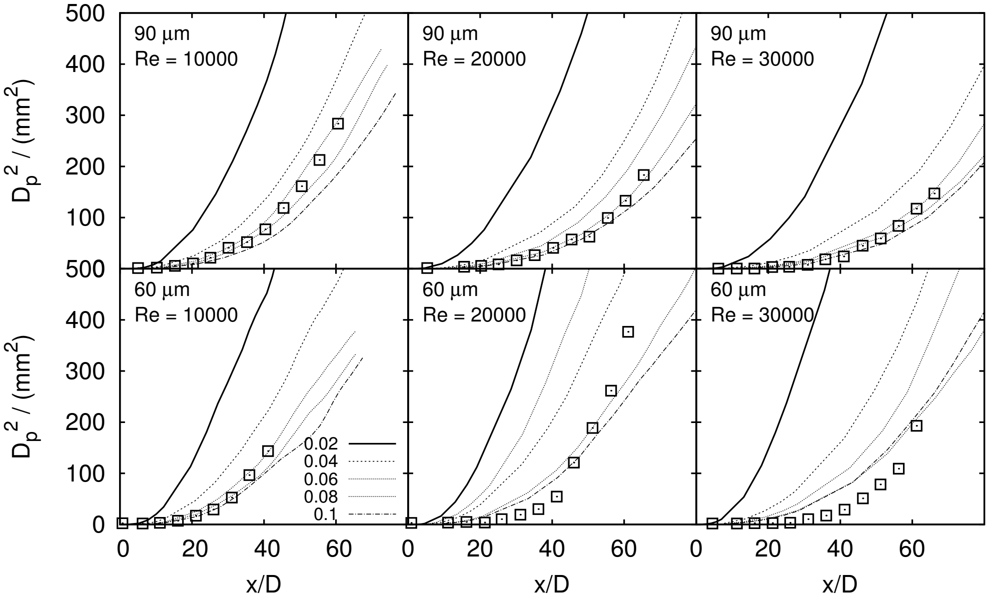

Figure 5.16: β_p sensitivity on the Type-C dispersion of 60 μm and 90 μm particles in the 7 mm jet with Re = 10,000, 20,000 and 30,000. Square symbols represent experimental measurements.

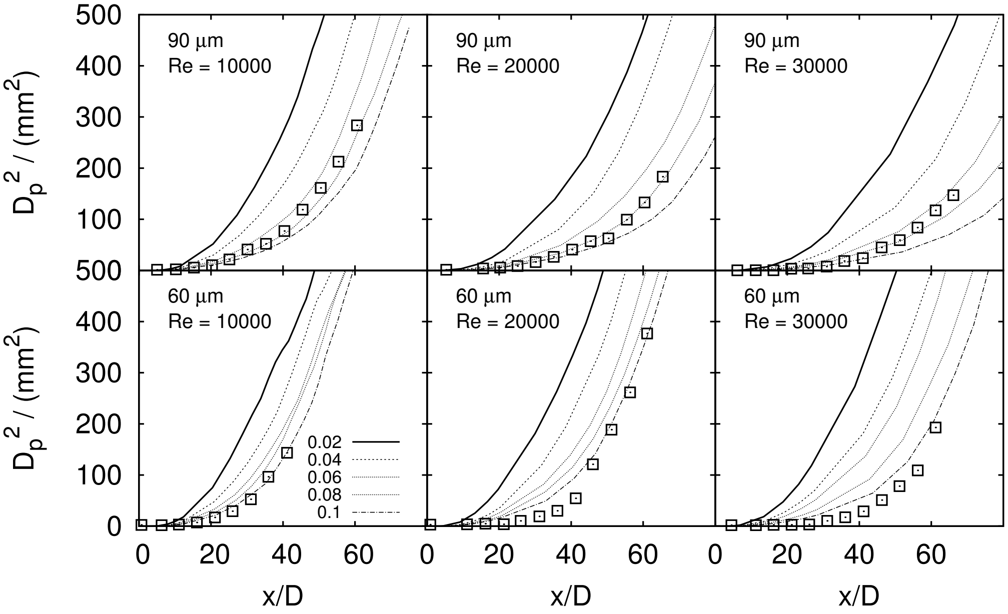

Figure 5.17: β_p sensitivity on the Type-IC dispersion of $60\,\mu m$ and $90\,\mu m$ particles in the $7\,mm$ jet with $Re = 10,000$, $20,000$ and $30,000$. Square symbols represent experimental measurements.

clearly observable in the figure. That is, the dispersion of the small light particles in the slow shear flow is less sensitive to β_p. The Type-C interaction model is shown to be more sensitive to β_p than the two other models. This is because the Type-C model allows the particles to interact with multiple eddies simultaneously that leads to more trajectory crossings.

5.5 Conclusions

This chapter has been concerned with the development of ODT multiphase models (Type-I, -C, and -IC) to predict the transport of individual particle in a turbulent round jet flow. The challenge in this work is to properly account for the particle-eddy interaction.

The ODT multiphase model uses a Lagrangian framework to solve the trajectory equations of a particle as it interacts with a succession of discrete turbulent eddies. The Lagrangian framework treats the particles as distinct entities within the fluid phase. The Type-I PEI model uses instantaneous particle-eddy interactions and provides good predictions to particle dispersion, but could not allow the particles to interact with multiple eddies at the same time. The Type-C PEI

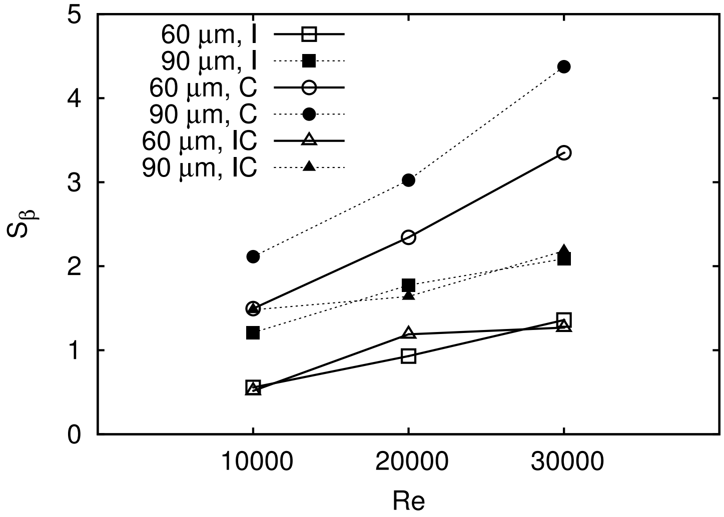

Figure 5.18: β_p sensitivity spread on dispersion of $60\,\mu m$ and $90\,\mu m$ particles at $x/D = 50$ in the $7\,mm$ jet with $Re = 10,000$, $20,000$ and $30,000$.

model resolves the above drawback of the Type-I PEI model by using continuous PEI(s) for the finite evolution time. However, it is not able to capture tracer limit and therefore only accurately predicts the high Stokes number particles. The Type-IC PEI model combines the features of the Type-I and -C PEI models, which is considered as the most robust PEI model among the three.

The models have been validated for a range of characteristic particle response times and jet exit velocities. The particle dispersion in Lagrangian form is initially quadratic for short times-of-flight; the function becomes linear for long times-of-flight as the particle Stokes number becomes $O(1)$ and the particles behave more like tracer particles. The only model parameter β_p introduced in the models is used to scale the interaction time and fluid velocities felt by particles during the interactions. Apparently, even though the eddy time scale $t_e = \beta_p \tau_e$ increases, the crossing trajectory effect plays a role in limiting the interaction time $T_{ixn} = l/2g\tau_p$, that is less than t_e.

CHAPTER 6. TURBULENT PARTICLE-LADEN JETS

6.1 Introduction

The effect of particles on fluid-phase turbulence is known as turbulence modulation. The extent of turbulence modulation is influenced strongly by particle concentration. In the previous two chapters, the dynamics of the single particle is investigated in homogeneous turbulence and jet flow. Those flow scenarios have extremely dilute particle volume fraction ($< 10^{-5}$), and, therefore, the turbulence modulation is weak and can be neglected (one-way coupling in Sec. 2.2.1). On the opposite limit of very dense particle volume fraction near the state of the fluidized bed, fluid turbulence is attenuated by large viscous force associated with Reynolds number based on the inter-particle spacing (four-way coupling in Sec. 2.2.1). As the current implementation of ODT model does not consider the inter-particle collision, this very dense gas-solid flow is not in the scope of this study. In the intermediate range of particle volume fraction ($> 10^{-5}$) (two-way coupling in Sec. 2.2.1), turbulence modulation is very important. The addition of particles in the intermediate range can either enhance or reduce the gas turbulence, affecting the overall flow behavior of gas-solid flow.

The main objective of the present study in this chapter is to perform Lagrangian ODT multiphase simulations for a temporally developing turbulent particle-laden planar jet and to compare the model prediction with experimental measurements [103]. This work uses the Type-I particle interaction model to compare directly with experimental data for the turbulent particle-laden jet and also demonstrates the richness of numerical data the model can provide.

This chapter is organized as follows. Section 6.2 presents some details of the model used for the present work followed by the description of the computational configuration in Section 6.3. Then in Section 6.4, the model's capability is evaluated to predict the important statistics of the turbulent particle-laden jet. The profiles of mean velocities, velocity variance modulated by particles, particle velocities, and particle distributions are presented.

6.2 Numerical description

The temporally developing ODT model for gas-solid flows, as formulated, solves the conservation equation set of Eqs. 3.3-3.5. $S_{p,u}$, $S_{p,v}$, and $S_{p,w}$ are the gas-phase momentum source terms from particles in three directions for two-way coupling, respectively, which are defined in Eq. 3.33. To ensure conservation of momentum and kinetic energy, the triplet map is implemented by two kernel functions, $K(y)$ and $J(y)$ when applied to the scalar fields in the two-way coupling implementation. For the nonreacting flow of constant density, a detailed implementation of kernel transformation of a triplet map is described in Sec. 3.2.6. The values of ODT parameters in the present work are 16, 50 and 0.4 for C, Z and β, respectively, which are consistent with the parameters used in Chapter 5. The particle parameter, β_p, is 0.08 that is the value used in the study of particle dispersion in the nonreacting jet flow in Chapter 5. The particle motion is determined by the drag force and gravity, which can be expressed in Eq. 3.29.

6.3 Computational configuration

The experimental study has been performed on turbulent particle-laden flows in coaxial jet configuration by Budilarto [103]. Reynolds number corresponding to the total flow rate of the gas-phase is $8,400$ for all experimental investigations. Fully developed turbulent flow conditions at the nozzle exit are used. The centerline velocity of the single-phase flow, U_0, is $11.7 m/s$ and used to normalize the velocity data. The nozzle diameter, D, is 0.56 inchs and is used to normalize the distances. The fluid gas used here is air at room temperature.

Glass bead particles of number average diameter of 25 and 70 μm are used for the study, and the mean particle density is $2,500 kg/m^3$. Solid loadings of the particles, SL, are set at 0.25, 0.5 and 1.0 and the particles are distributed in the monodisperse suspension. Simulation initial conditions for monodisperse suspensions of 25 and 70 μm particles are listed in Table 6.1. Here U_{p0} is initial particle velocity, n_p is the number of particles in the simulation, and N_p is the number of particles represented by each pseudo particle introduced in Eq. 3.33.

Table 6.1: Simulation initialization details of particle properties in the gas solid jet.

diameter (μm)	solid loading	ρ_p (kg/m^3)	U_{p0} (m/s)	n_p	N_p
25	0.5	2,500	11.326	430	1,000,000
	1.0	2,500	11.205	425	2,000,000
70	0.25	2,500	9.728	456	25,000
	0.5	2,500	9.664	453	50,000
	1.0	2,500	9.474	433	100,000

6.4 Results and discussion

The ODT simulations in the study are performed for a planar jet configuration, whereas the experimental data considered here are collected from a round jet configuration. As mentioned in the previous chapter, the temporal planar jet is comparable to the spatial round jet when both have the same constant Reynolds number, which is illustrated by constant-density momentum similarity scaling [100]. To compare the temporal simulation results with the spatial experimental data, the evolution transformation is necessary and given in Eq. 5.1. The transverse or line- (y) and streamwise (x) directions in the planar jet correspond to the radial (r) and axial (x) direction in the spatial round jet, respectively. The velocity and location data presented below are normalized by the initial gas velocity, U_{g0}, and jet diameter, D, respectively. The experimental measurements are denoted as EXP whereas the results generated from ODT simulations are denoted as ODT. This type of nomenclature is used in the following discussion and related plots. Statistics from all the simulations here are collected over 512 realizations.

6.4.1 Single phase flow

Considering the comparison between the ODT results and the experimental data, it is vitally important first to do some direct comparisons to validate the single-phase ODT code. As mentioned before, the same ODT parameters as in Chapter 5 are used in this study for the consistency.

The streamwise evolution of the mean axial velocity and turbulence intensity along the jet centerline is shown in Fig. 6.1. Overall, the numerical results agree well with experimental data. For the single-phase unladen jet, there are two development regions in the flow evolution.

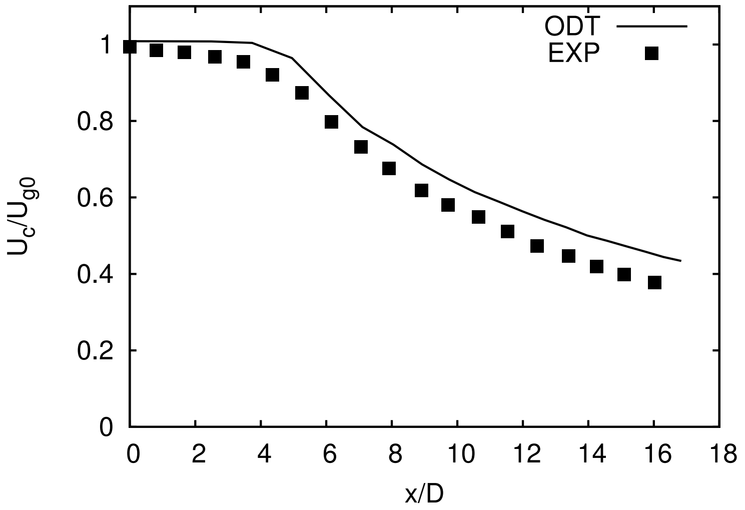

(a) Mean axial velocity

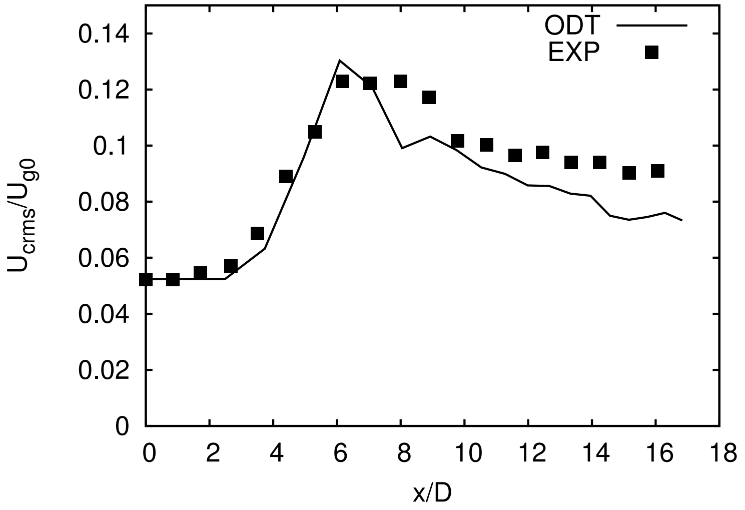

(b) Turbulence intensity

Figure 6.1: Normalized mean axial velocity (a) and turbulence intensity (b) of single phase flow along the jet centerline.

In the initial region of $x/D < 5$, the mean axial velocity along the centerline tends to decrease at a relatively slow rate and the turbulent intensity in the axial direction increase from 5% up to 13%. The region is known as the potential core region. The second flow region begins to develop a significant decaying rate of mean centerline axial velocity. Most of the eddies occur in the shear layer and mix the ambient fluid of low velocity into the jet to affect the jet decay. The turbulence intensity along the centerline decreases and then is almost constant at the level of 10% in the far-fields.

Figure 6.2 compares the radial profiles of the gas mean velocity normalized by the initial jet velocity at streamwise locations of x = 5D, 10D, and 15D. As the jet decays and spreads, the mean velocity profiles change and become flat as shown in both the simulation and experiment. Eventually, the jet develops to the region of self-similarity ($x/D > 30$), in which the profiles of normalized mean axial velocity plotted against $y/y_{1/2}$ collapse onto a single curve. $y_{1/2}$ is half of the jet width, which is defined as

$$U\left(x, y_{1/2}\right) = \frac{1}{2} U_{g0}. \tag{6.1}$$

The numerical results in this study are not in the self-similarity region. Compared to the experimental data, the model overpredicts the velocities close to the jet center that is also observed in Fig. 6.3(a), and underpredicts the velocities around the nozzle edge.

6.4.2 Particle-laden flow

Jet evolution

Figure 6.3(a) shows the comparison of the radial profiles of axial mean gas velocity U_c modulated by the presence of 70 μm particles at different solid loadings: 0.25, 0.5 and 1.0. Beyond the initial flattening region ($x/D > 5$), the addition of particles results in a reduction in the decaying rate of the mean gas velocity near the nozzle exit around the jet center. The particles lag behind the fluid and have higher mean velocities than the gas phase beyond $x = 5D$. Therefore, the particles transfer their momentum through the interface drag force to the fluid and lead to the observed modulation in U_c. Also, the modulation in U_c becomes more pronounced with increasing solid loadings. This phenomenon is likely due to the increase in the number of particles added into the

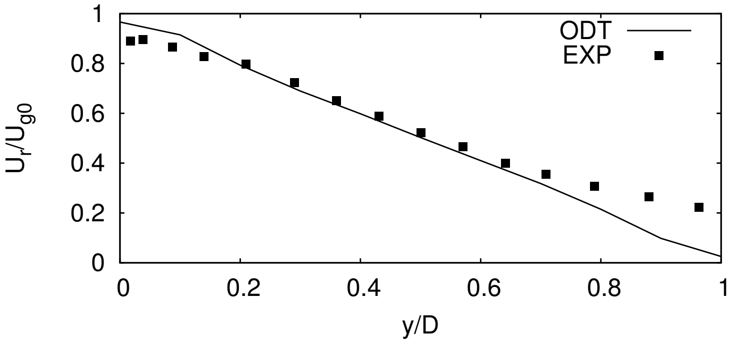

(a) x/D = 5

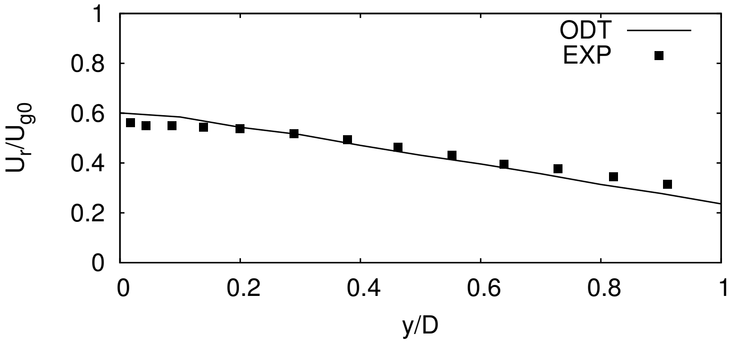

(b) x/D = 10

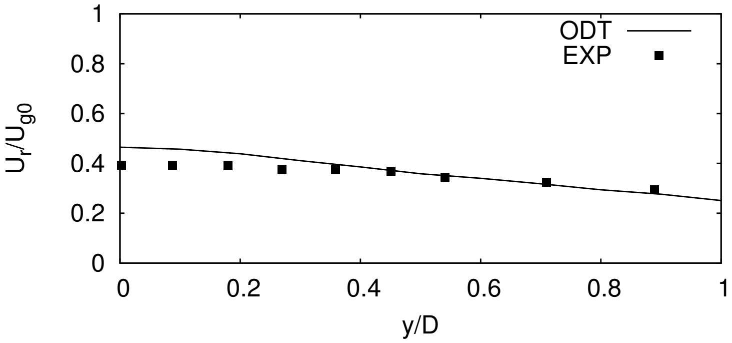

(c) x/D = 15

Figure 6.2: Radial profiles of gas mean velocity normalized by initial jet velocity at different streamwise locations x = 5D, 10D and 15D.

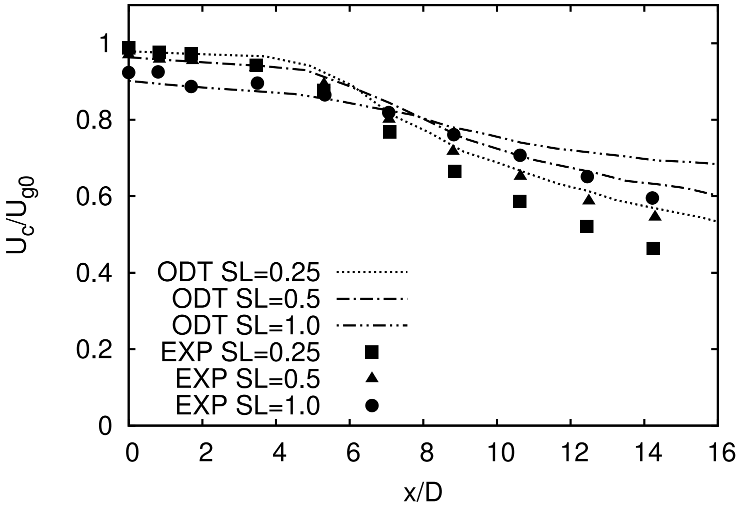

(a) 70 μm particle

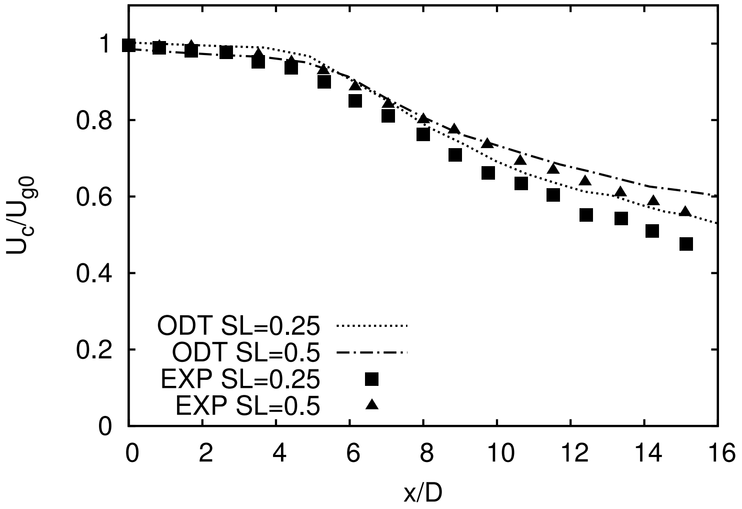

(b) 25 μm particle

Figure 6.3: Streamwise development of axial mean gas velocity along the centerline with different particle solid loading.

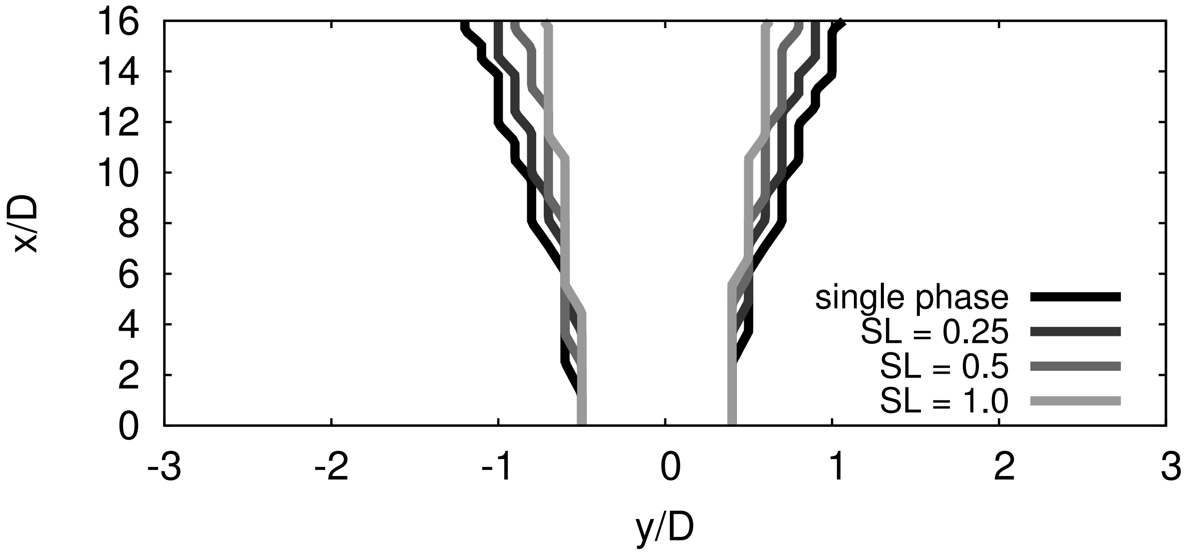

Figure 6.4: Streamwise evolution of jet width with different solid loadings SL = 0.25, 0.5 and 1.0.

flow, which interact with the gas phase. Figure 6.3(b) shows the radial profiles of U_c with the presence of 25 μm particles at different solid loadings. Similar to the jet flow laden by the 70 μm particles, the reduction of U_c due to the addition of particles becomes more pronounced as the solid loading of the 25 μm particles increases.

Figure 6.4 shows the ODT predictions of jet widths of particle-laden jets with different solid loadings of 70 μm particles. Generally, the addition of the particles tends to make the overall jet flow denser and harder to spread towards the sides. In the view of the distribution of particle number density (discuss later in Fig. 6.12), a high percentage of the particles appear in the jet center for the high solid loading case. More particle-turbulence interactions in the center of the jet lead to less dispersion of the fluid parcels away from the jet. So as the figure shows, the particle-laden jets become narrower with the presence of more particles. For the planar jet, the characteristic velocity $\tilde{V}(t)$ and characteristic width $\tilde{W}(t)$ are assumed at time t. Then the global momentum conservation of the jet implies the constant $\tilde{V}\tilde{W}$, hence $\tilde{V} \sim 1/\tilde{W}$. It turns out that the narrow jet width leads to a steep radial velocity profile. This is consistent with ODT predictions of the radial profiles of U_r with different solid loadings in Fig. 6.5. The above simple scaling analysis is introduced in [99].

The turbulence modulation by the addition of the 70 μm particles with different solid loadings is shown by centerline development of axial RMS velocity U_{crms} in Fig. 6.6(a). The particle

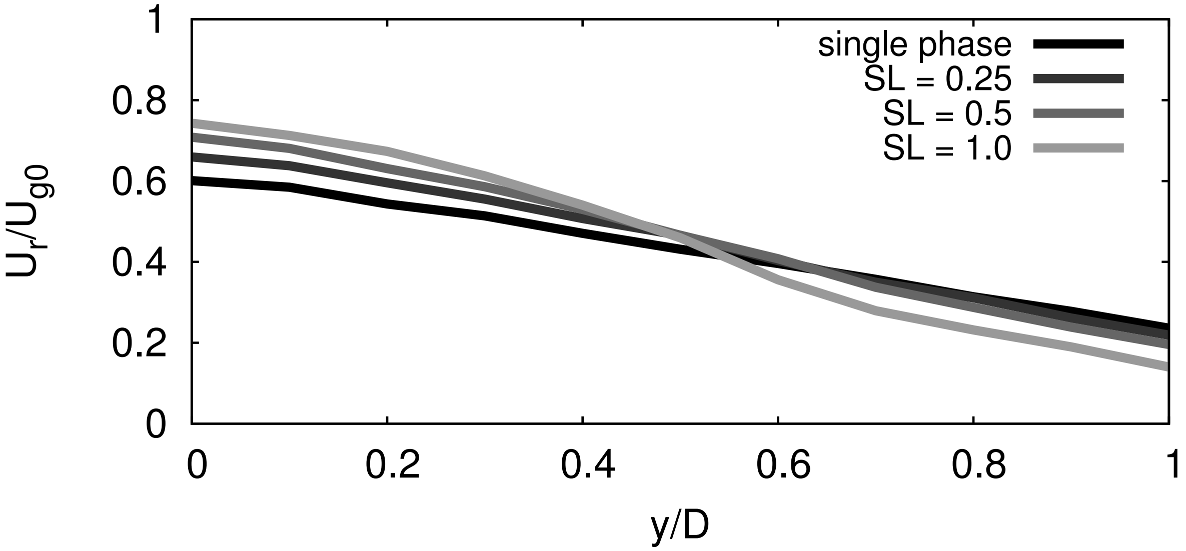

Figure 6.5: Radial profiles of gas mean velocity normalized by initial jet velocity with different solid loadings SL = 0.25, 0.5 and 1.0 of 70μm particles at streamwise location x = 10D.

addition reduces the peak value of U_{crms} and moves the streamwise location corresponding to the maximum U_{crms} further away from the nozzle exit. The downward movement of U_{crms} indicates that the presence of particles dampens the turbulent development of the gas phase. The U_{crms} reduction along the jet centerline occurs because the particles dissipate the turbulent kinetic energy of the gas phase as turbulent eddies transport them via PEIs. It is also observed in Fig. 6.6 that the gas RMS velocities are dampened more as the solid loading increases. This is because more particles interact with the gas as the solid loading increases. Figure 6.6 also shows that with increasing solid loading the streamwise location of the maximum U_{crms} moves further downstream that is followed by a reduction in the decaying rate of U_{crms}. This is related to the narrowing of the jet width in the particle-laden jet (Fig. 6.4) which leads to a steep radial profile in U_r (Fig. 6.5) and thus an increase in the shear strain of gas phase. The increase in the shear strain promotes an increase in the production rate of turbulent kinetic energy that reduces the decaying rate of the RMS velocities. The effect of energy production dominates beyond $x/D > 6$ because there is no significant difference of jet width for different solid loading cases when $x/D < 6$ as shown in Fig. 6.4. The downstream shift of the maximum U_{crms} is attribute to a more pronouced energy dissipation effect of high solid loading in the early stage. Again, the jet width for different solid

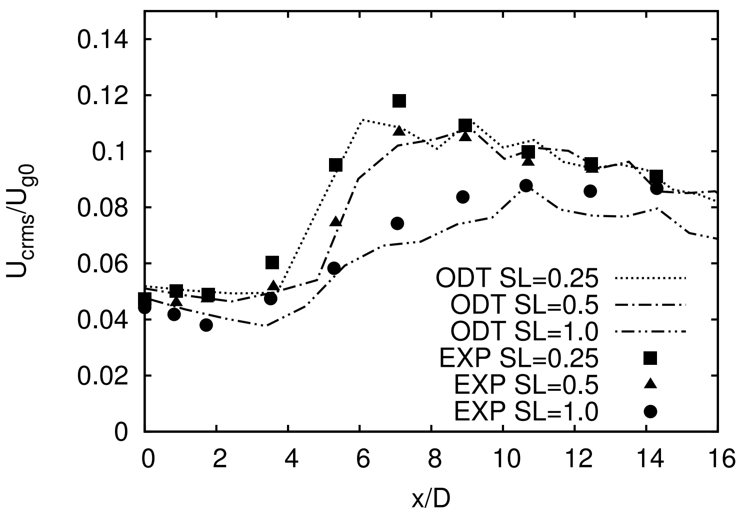

(a) 70 μm particle

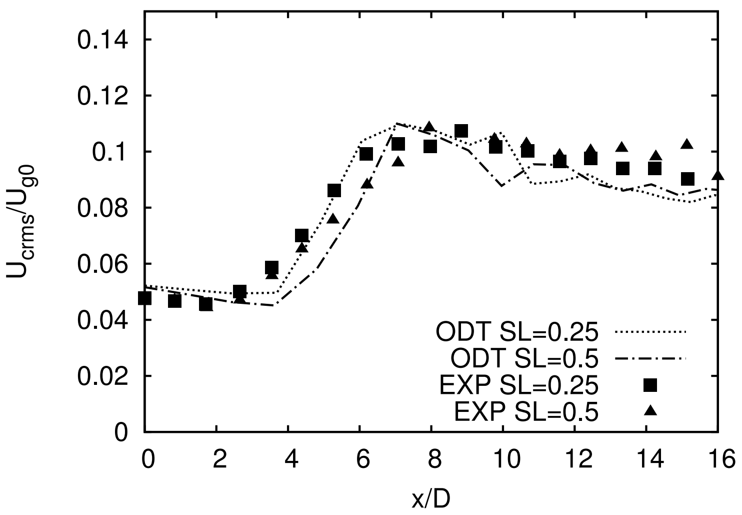

(b) 25 μm particle

Figure 6.6: Streamwise development of axial RMS gas velocity along the centerline with different particle solid loading.

loading cases is almost the same at $x/D < 6$, indicating the effect of energy production is similar in this region. However, due to the dissipation of more energy by more particles, the turbulence takes longer to develop to the same intensity in the jet flow of high solid loading. In sum, two competing mechanisms govern the turbulence modulation in a particle-laden jet flow. First, the turbulence is suppressed by the energy dissipation effect of particle addition on gas-phase turbulence, which is dominant in the early development of the turbulent flow. Secondly, the turbulence is promoted due to the modification of the shear strain that tends to produce the kinetic energy, which is dominant in the late evolution of the turbulence.

Figure 6.6(b) shows the streamwise development of axial RMS gas velocity along the centerline of the jet flow laden by the $25\,\mu m$ particles. The turbulence modulation in the particle-laden jet with $25\,\mu m$ particles follows the trend as that with $70\,\mu m$ particles shown in Fig. 6.6(a).

Particle evolution

Figure 6.7 displays the centerline development of the axial mean velocities, U_{pc}, for $70\,\mu m$ and $25\,\mu m$ particles with different solid loadings. Both experimental measurements and simulation results show that there are two development regions in terms of the mean relative velocity between the particle and gas phases.

The locations of the first region are about $x < 6D$ and $x < 5D$ of the flow field laden by $70\,\mu m$ and $25\,\mu m$ particles, respectively. In these regions, the particles' velocities are lower than the gas velocities, and the gas accelerates the particle velocity that leads to a decrease in the mean axial velocity of gas phase as shown in Fig. 6.3. The relative velocity between particles and gas at the nozzle inlet determines the length of the first development region. Small particles have the smaller relative mean velocity to the gas phase in this study and also respond to turbulence fluctuation faster than large particles. Thus, the length of this region for the small particles is shorter than for the larger particles.

The second development regions are located at $x > 6D$ and $x > 5D$ for the flow with the addition of $70\,\mu m$ and $25\,\mu m$ particles. In these regions, the mean axial particle velocity is higher than the mean gas velocity, and the particles start to accelerate the gas velocity via PEIs. This leads to the reduction of the decaying rate of axial gas mean velocity, and also the decaying of the particle mean velocity. Figure 6.7 shows that the decaying rate of mean particle velocity along

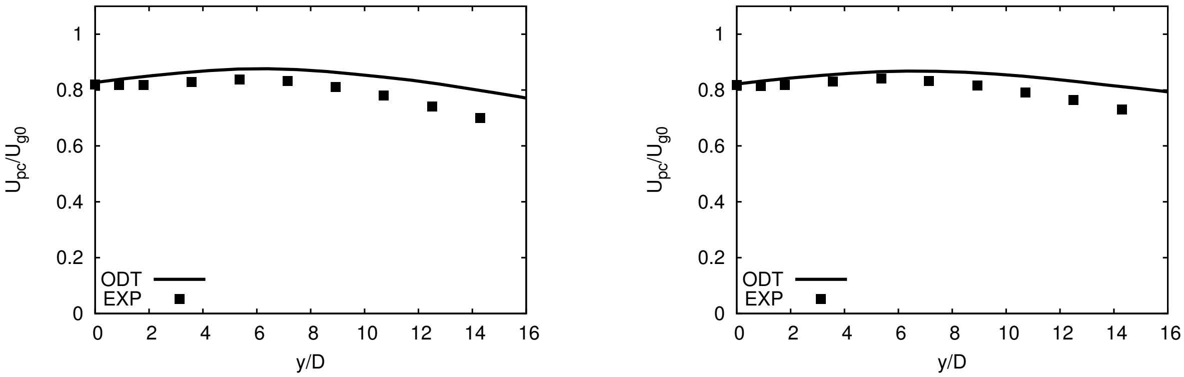

(a) 70 μm particle, SL = 0.25

(b) 70 μm particle, SL = 0.5

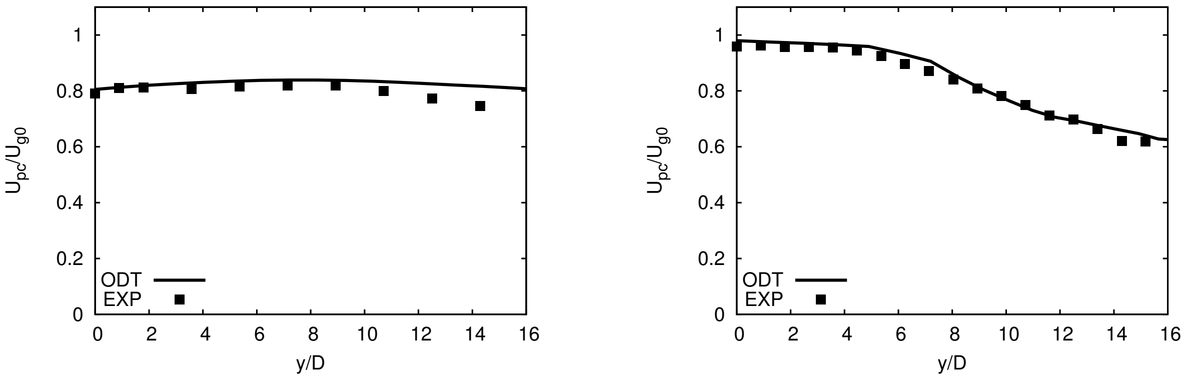

(c) 70 μm particle, SL = 1.0

(d) 25 μm particle, SL = 0.5

Figure 6.7: Mean axial centerline particle velocity at different streamwise locations.

the jet centerline depends on the particle size and solid loading. For the same particle size (for example, 70 μm particles in Fig. 6.7(a) - 6.7(c)), increasing solid loading results in a high transfer rate of the momentum from the particle phase to the gas fluid as discussed in Fig. 6.3(a). The fast momentum transfer between two phases leads to a strong reduction of the decaying rate of mean gas velocity. This suggests that an increase in solid loading would reduce the mean relative velocity between two phases, thereby reducing the decaying rate of the particles. Thus, both the gas and particle velocities increase with increasing solid loading, as the interaction between two phases is two-way. Comparison of Fig. 6.7(b) and Fig. 6.7(d) reveals that for the same solid loading, the mean velocity of the small particles decreases much faster than the large particles. This is because the small particles have shorter relaxation time than the large particles. The simulation overpredicts the mean axial particle velocities in the second region that are consistent with the overpredicted mean axial gas velocities observed in Fig. 6.3.

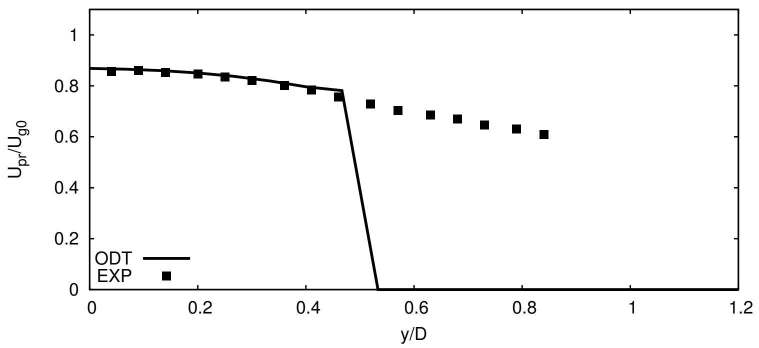

(a) x/D = 5

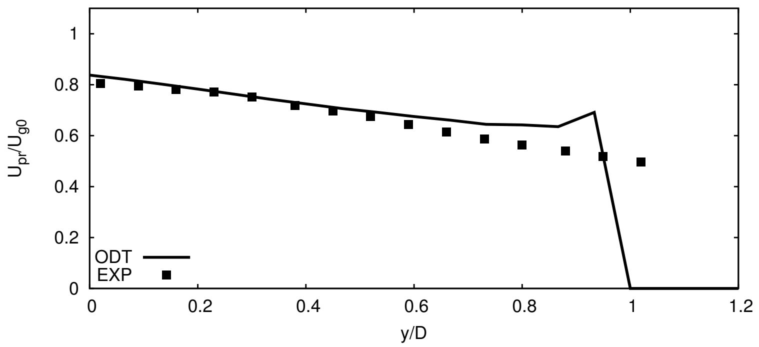

(b) x/D = 10

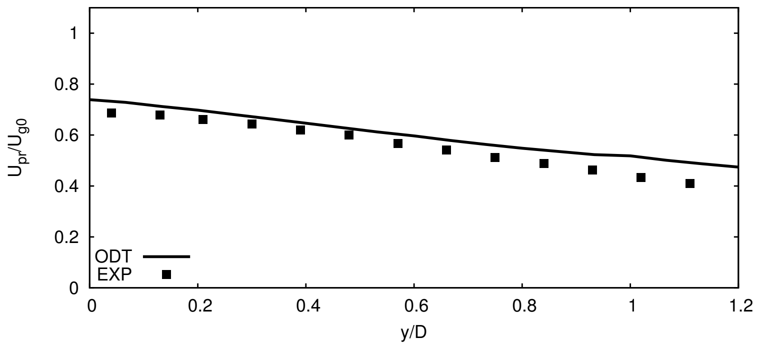

(c) x/D = 15

Figure 6.8: Radial profiles of mean particle velocity for $70\,\mu m$ particle and SL = 0.25 at different streamwise locations x = 5D, 10D and 15D.

Figures 6.8, 6.9, and 6.10 show the radial profiles of mean axial velocity, U_{pr}, for the $70\,\mu m$ particles with different solid loadings of 0.25, 0.5, and 1.0 at streamwise locations of 5D,

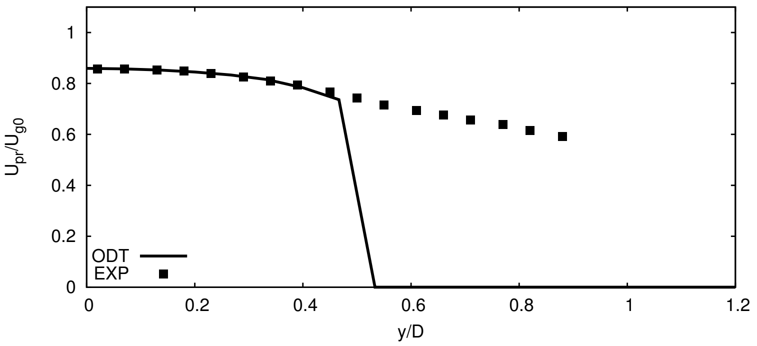

(a) x/D = 5

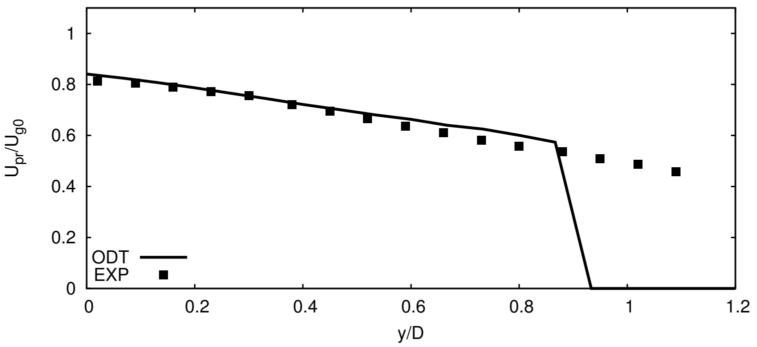

(b) x/D = 10

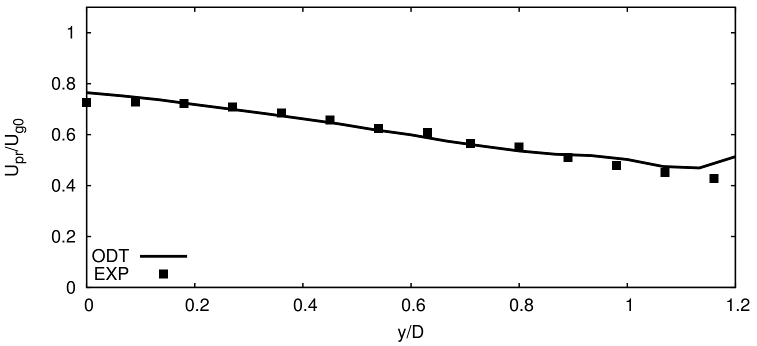

(c) x/D = 15

Figure 6.9: Radial profiles of mean particle velocity for $70\,\mu m$ particle and SL = 0.5 at different streamwise locations x = 5D, 10D and 15D.

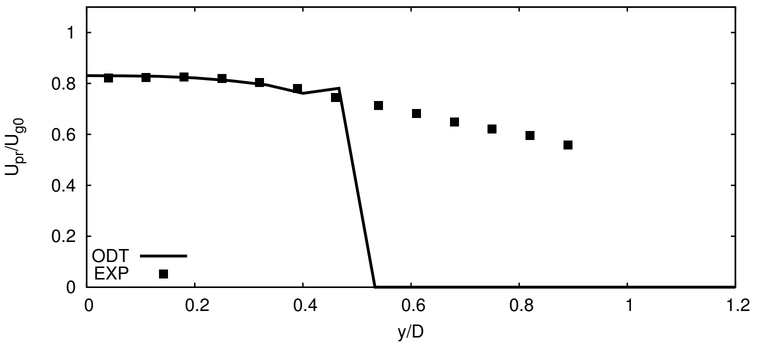

(a) x/D = 5

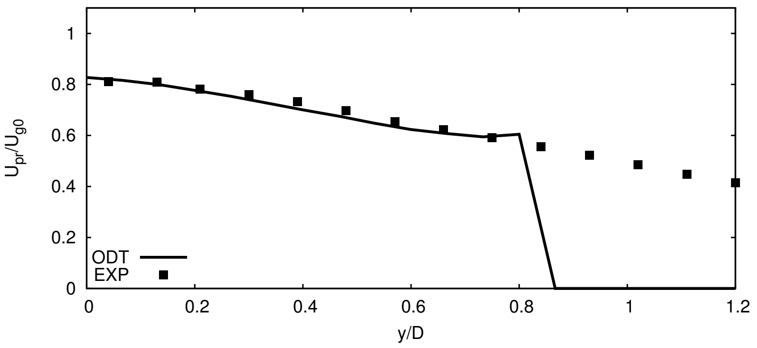

(b) x/D = 10

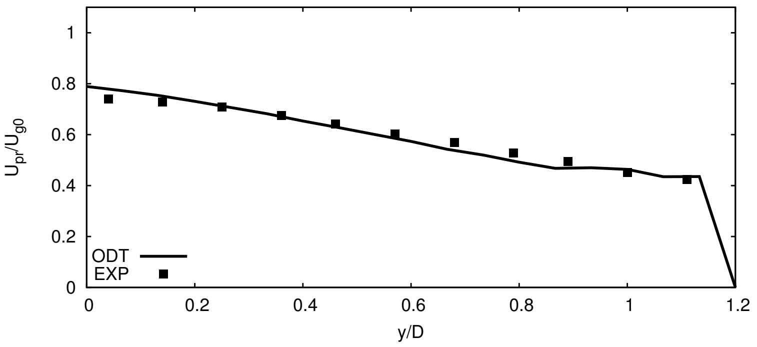

(c) x/D = 15

Figure 6.10: Radial profiles of mean particle velocity for 70 μm particle and SL = 1.0 at different streamwise locations x = 5D, 10D and 15D.

10D, and 15D. Initially, the particles have a flat profile of mean axial velocity at the nozzle inlet. As the particles move downstream, the flat profile of U_{pr} along the radial direction become nonuniform. This indicates that the particles tend to mix with the ambient gas of lower velocity at $y/D > 0.5$ when they disperse towards the nozzle edges. The simulations provide good predictions to particle velocity profiles in the nozzle ($y/D < 0.5$) and at a further axial location from the nozzle exit ($x/D > 10$). However, the simulations do not predict enough radial dispersion of the large particles at the early stage of the development.

The radial profiles of the mean axial velocity, U_{pr}, of the $25\,\mu m$ particles of solid loading of 0.5 at $x = 5D$, $10D$, and $15D$ are presented in Fig. 6.11. Similar to the development of the $70\,\mu m$ particles, the flat profiles of U_{pr} is lost as the particles move further from the nozzle exit. It is also observed that the U_{pr} profiles are more similar to the radial profiles of mean axial gas velocity shown in Fig. 6.2, because the $25\,\mu m$ particles are more responsive to the gas behavior.

Figure 6.12 shows the radial profiles of particle number density normalized by initial particle distribution for $70\,\mu m$ particle and SL = 0.25, 0.5, and 1.0 at different streamwise locations $x = 5D$, $10D$, and $15D$. As the jet evolves, the particles tend to disperse away from the center of the jet and the particle distribution of number density widens. Interestingly, a bimodal distribution of particle number density is observed for all the particle solid loadings. The two peaks of particles distribution are located at shear layers ($x/D = -0.5$ and 0.5) where strong turbulent diffusivity promotes the entrainment of more particles. With high solid loading, a high percentage of the particles are accumulated in the center of the jet. In the flow of high solid loading, more particles interact with the jet and dissipate the kinetic energy of turbulence, thereby reducing the turbulence intensity U_{crms} as presented in Fig. 6.6. Thus, the turbulence suppression due to high solid loading leads to the reduction of the dispersion of the particles. Figure 6.13 compares the radial profiles of particle number density normalized by initial particle distribution for $25\,\mu m$ and $70\,\mu m$ particles of the same solid loading of 0.5 at streamwise locations x = 5D and 15D. For smaller particles, wider distribution of particle number density implies higher dispersion than larger particles.

The bimodal distribution of particle number density observed in this study is an interesting dispersion pattern, which has been named the "preferential concentration" or "clustering" effect [24, 44, 97]. The nonuniformity of the particle number distribution is a function of the particle inertial time scale. It is worth noting that the effect of turbulence on the particle distribution is not

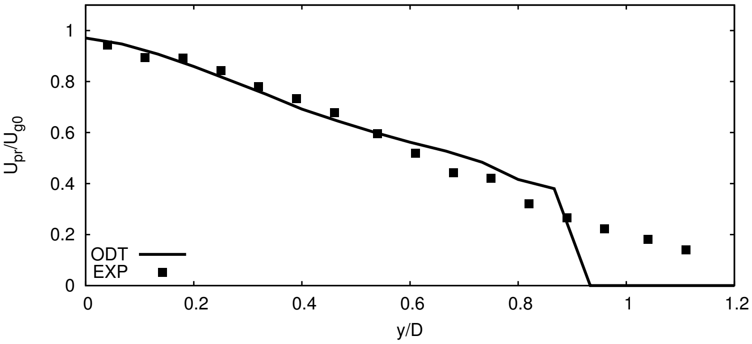

(a) x/D = 5

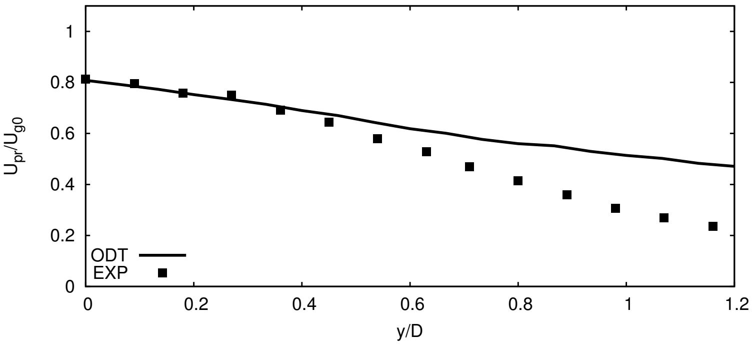

(b) x/D = 10

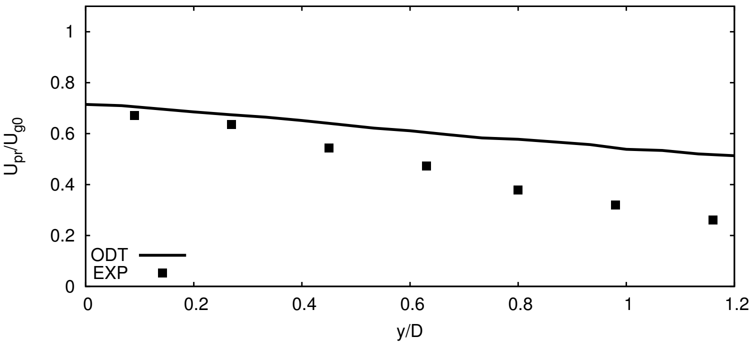

(c) x/D = 15

Figure 6.11: Radial profiles of mean particle velocity for 25 μm particle and SL = 0.5 at different streamwise locations x = 5D, 10D and 15D.

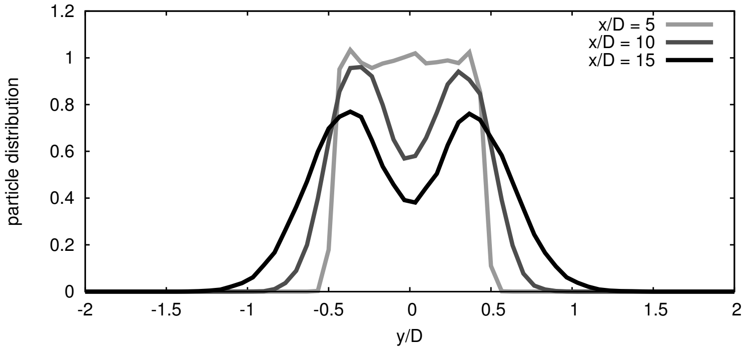

(a) SL = 0.25

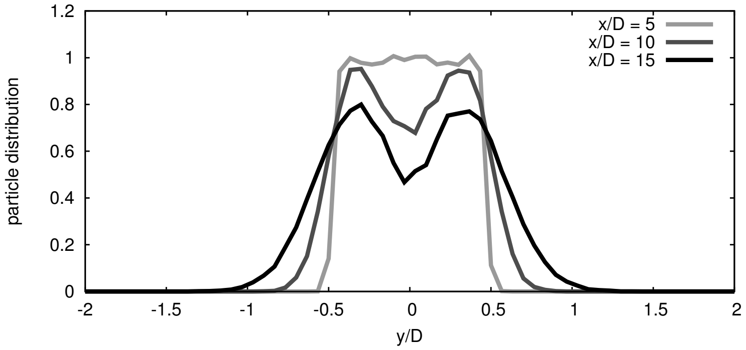

(b) SL = 0.5

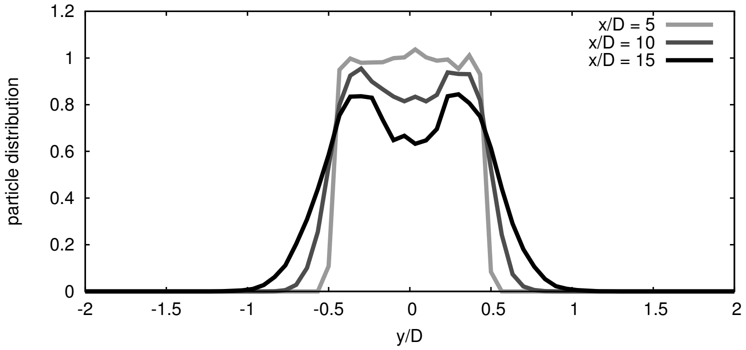

(c) SL = 1.0

Figure 6.12: Radial profiles of normalized particle number density for $70\,\mu m$ particle and SL = 0.25, 0.5 and 1.0 at different streamwise locations x = 5D, 10D and 15D.

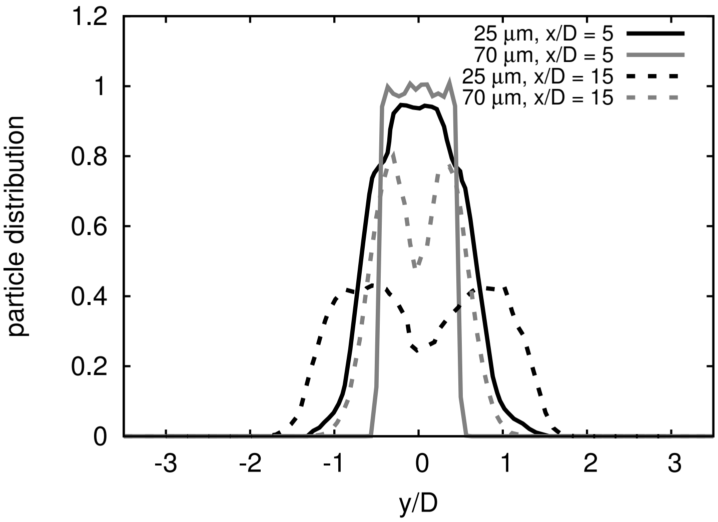

Figure 6.13: Normalized particle number density over the simulation domain for 25 μm and 70 μm particles of solid loading of 0.5 at streamwise locations x = 5D and 15D.

a monotonic function of the particle time scale. For decreasing values of the particle time constant the particles behave more as fluid elements, and therefore, exhibit a decreasing tendency for preferential concentration due to the continuity constraint of fluid particles. This has been verified in a testing case in which the fluid tracer particles and "quasi-tracer" particles of fairly small inertia are initialized at the same locations in the jet flow. As the jet evolves, the particle number density of quasi-tracer and real tracer predicted have good agreement, both of which show no preferential accumulation. Once the particle time scale increases to large enough value, the particles also exhibit less tendency for preferential concentration because they would not be capable of responding to the surrounding fluid velocity. For the intermediate sized particles, such as those studied here, the particles become temporarily "trapped" within the successive eddies in the regions of shear layers and lead to the peak in the particle radial distribution. This implies that the turbulence may inhibit, rather than enhance, the mixing of particles. These findings are consistent with previous experimental measurements and computational research [24, 44, 59, 97, 104]. Experimental measurements of particle dispersion in free shear layers have shown that the particle concentration field is well correlated with the large-scale vortical structures [59]. Maxey [104] and Squires [44] used asymptotic methods and DNS to demonstrate that the effect of inertia was to cause dense particles to accumulate in regions of low vorticity and high strain rate. Recent DNS [24] and LES [97] simulations of particle-laden jet flow illustrate that for only the particles of certain intermediate Stokes number, it is possible that particles exhibits the clustering behavior in the regions of high turbulence intensity and have the more effective preferential concentration effect on the dispersion statistics compared to small and large Stokes number particles. Interestingly, the referenced DNS and LES simulations show the bimodal shape of particle number density distribution in the radial direction as presented in Fig. 6.12 and 6.13.

6.4.3 Parameter sensitivity analysis

In the current implementation, β_p is the only new adjustable parameter introduced into the original ODT model. It relates the turbulence characteristics to the particle-eddy interaction time by scaling the turbulent time scales and observed fluid velocity by the particles through Eq. 3.25 and 3.35. High β_p leads to possibly high interaction time by increasing the maximum interaction timescale $\beta_p \tau_e$ and reducing the eddy moving velocity, $\triangle Y_{TM}/(\beta_p \tau_e)$, felt by the particles during the interactions. Apparently, there are two competing effects associated with β_p on particle dispersion. The fundamental physical details on β_p have been discussed in the previous chapters. The values of β_p used in this section are 0.04, 0.06, and 0.08, in which 0.08 is used in ODT simutlions in previous sections.

Figure 6.14 compares the radial profiles of the number distribution of $70\,\mu m$ particles normalized by initial particle distribution with solid loading of 0.25 and 0.5 at the streamwise locations $x = 10D$ and $15D$ using different β_p. Low β_p leads to a wider distribution of particle number density. This is attributed to larger particle dispersion as low β_p increases the eddy velocity experienced by the particles. This greater dispersion with low β_p is consistent with the effect of β_p on the dispersion of single particle observed in Sec. 5.4.3 of Chapter 5. The various β_p change the two peaks of particle number density in the bimodal distribution, whereas the particle distribution at the center of the jet is nearly independent of β_p. More particles are entrained in the region of shear layers, that is, $y = -0.5D$ and $0.5D$ where there are more eddy occurrences and a higher turbulent intensity. Therefore, β_p plays has a significant effect on the particle dispersion in the region of shear layers.

Figure 6.15(a) and 6.15(b) show the mean axial gas velocity U_c normalized by initial mean gas velocity U_{g0} along the centerline with the presence of $70\,\mu m$ particles with different β_p. For low

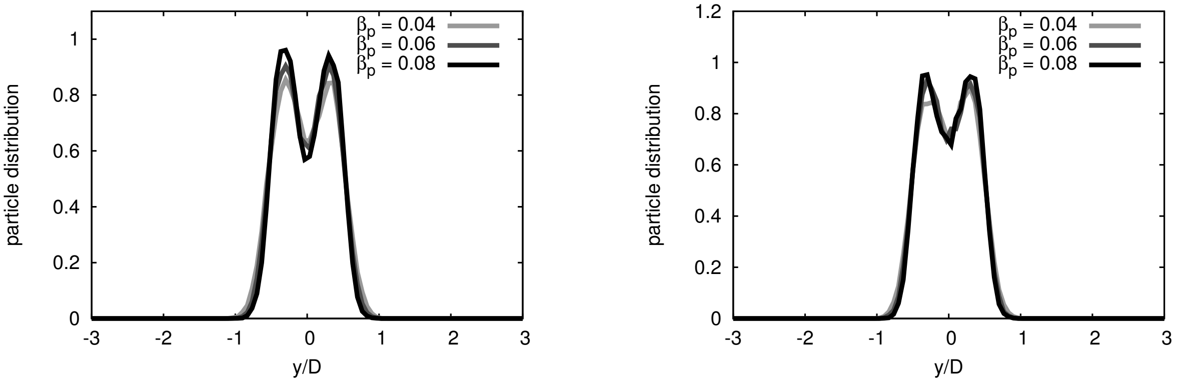

(a) SL = 0.25 (b) SL = 0.5

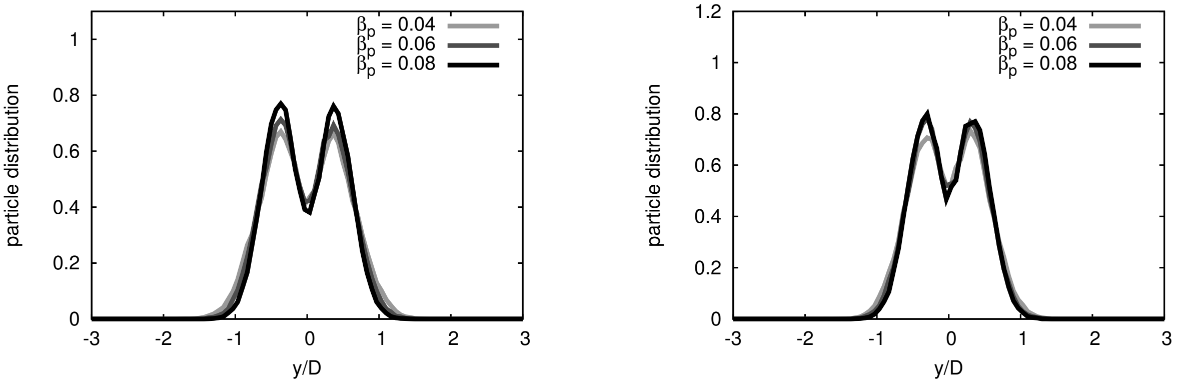

(c) SL = 0.25 (d) SL = 0.5

Figure 6.14: Radial profiles of normalized particle number density for 70 μm particles at streamwise location x = 10D (top) and 15D (bottom) with different β_p.

β_p, there is a reduction of the decaying rate of mean axial gas velocity along the jet centerline. Low β_p allows the particles to undergo high eddy velocity that accelerate the particles. Beyond $x = 6D$, the particles have a higher velocity than the gas phase, and they start to transfer the momentum to the gas. This momentum transfer is promoted by the acceleration of particle velocity due to low β_p, which leads to a reduction of the decaying rate of U_c.

The comparison of the RMS axial gas velocity U_{crms} normalized by initial mean gas velocity U_{g0} along the centerline with the presence of 70 μm particles with different β_p is displayed in Fig. 6.15(c) and 6.15(d). The addition of the particles with low β_p has a more pronounced effect of reducing the peak value of U_{crms}. As Fig. 6.15 shows, the particles have large dispersion and wide radial distribution of particle number density at low β_p. Large particle dispersion due to low β_p leads to the dissipation of more turbulent kinetic energy of the gas phase by the particles via PEI.

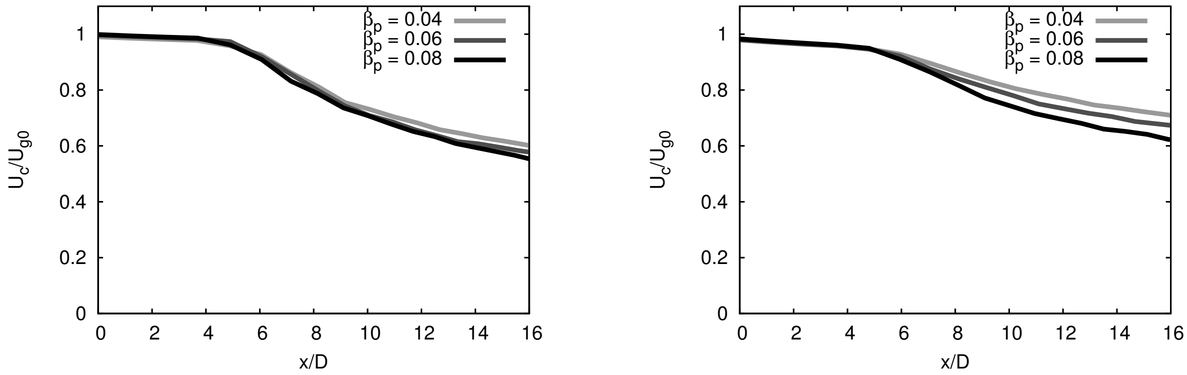

(a) SL = 0.25 (b) SL = 0.5

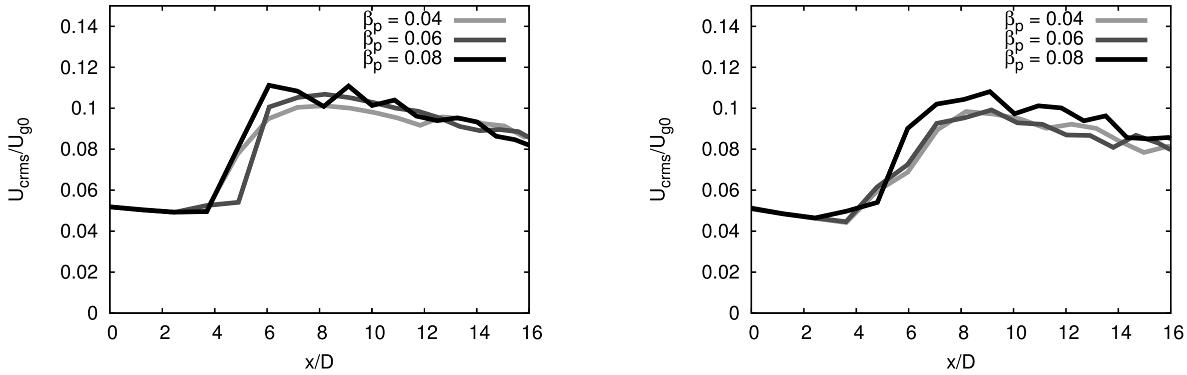

(c) SL = 0.25 (d) SL = 0.5

Figure 6.15: Mean (top) and RMS (bottom) axial gas velocity along centerline with the presence of 70 μm particles with different β_p.

6.5 Conclusions

In this chapter, the ODT multiphase model is extended to simulate a turbulent particle-laden jet in a temporally evolving planar configuration. A two-way momentum coupling mechanism is implemented to allow the gas motion to be modulated by the particles. Momentum transfer between the phases is accounted for through source terms from the particles in the diffusion equations. To couple with eddy motions, the source term is also implemented in the kernel transformation and an iterative procedure for eddy selection.

The ODT simulations for the single-phase flow and particle-laden jet flow compare well with experimental data. The same ODT parameters and particle parameter are used for consistency with the study of single particle dynamics in the jet flow in Chapter 5. The simulation results of single-phase flow suggests that the ODT model can qualitatively predict the typical fluid behavior of jet flow. For the simulations of the particle-laden jet, two different particle sizes and three different solid loadings are considered. The effect of particle addition on mean and RMS axial velocity of the gas phase is investigated. The development of particle velocity in the axial and radial directions and particle number distribution are illustrated. The simulation results compared to the experimental data show that the model qualitatively captures the flow modulation with the presence of difference particle classes with different solid loadings. Lastly, a parameter study is performed to investigate the effect of the only adjustable particle parameter β_p on two-way coupling jet flow.

CHAPTER 7. STATISTICS OF PARTICLE TEMPERATURE HISTORIES

7.1 Introduction

The spores produced by certain bacteria are known to pose severe threats to human health and safety. Neutralization of these biological agents has been a vital component of many threat reduction scenarios. Past experimental investigations suggest that the spore neutralization can be achieved by heating and chemical corrosion, both of which can be effectively used in multiple bio-agent defeat scenarios. The chemical process that involves water vaporization and structural corrosion of particles is not the scope of interest in this study. The present study addresses the post-blast-phase mixing between biological agent particles, the environment that is intended to neutralize them, and the ambient environment that dilutes the jet flow. The investigation of biological neutralization using experimental methods is challenging, and in some cases not feasible due to the destructive nature of the environment. When experimental investigations are not viable, numerical simulation is necessary to analyze the multiphase flow dynamics.

In the previous chapters, the ODT multiphase model was shown to accurately predict particle-fluid interactions in the isothermal jet flow, especially on the fine scales. In this chapter, the ODT model is used to investigate particle temperature histories in a non-isothermal ethylene jet flow. The high-temperature jet interacts with the particles of varying inertia and thermal relaxation time scales, τ_p and τ_H, which are initially outside the jet. The jet flow is bounded on one side by a wall. This particular configuration, on one hand, has practical interests, i.e., the neutralizaion of biological agents by a thermal and chemical environment of high temperature. On the other hand, the configuration includes much relevant physics that is not studied elsewhere and there are no experimental measurements of such particle heating available. Thus, this highlights the need for the methods to investigate this type of flows as provided by the current ODT multiphase model. The work in this chapter has been included as part of a technical report for this project [105].

Table 7.1: Particle properties in ethylene jet.

case #	1	2	3	4
density (kg/m^3)	972	97.2	9.72	0.972
diameter (μm)	100	100	100	100
τ_p (ms)	30	3	0.3	0.03
τ_H (ms)	30	3	0.3	0.03

7.2 Computational configuration

In carrying out the simulation of non-isothermal jet flow with the ODT model, the density changes associated with the turbulent mixing result in dilatational velocity changes [16]. Due to heat release, the convection velocity along the line occurs through the flow dilatation. Simulation grid cells are either expanded or contracted as required by continuity. The jet Reynolds number and time scale based on the initial velocity and thickness is $225,000$ and 5×10^{-4} s, respectively. The jet is taken to be the products of a stoichiometric ethylene flame, and its initial temperature is roughly 2300 K with an ambient temperature of 300 K. As such, heat release is minor, being associated only with chemical relaxations of the mixture towards the local equilibrium state.

Since there are no particular experiments to compare to, particle time scales are selected based on the estimation of particle heating time scales for single spores that are on the order of 10^{-4} s [106]. Here it is assumed that the particles have no internal temperature gradient due to the small particle size. Particle time scales in this chapter vary from the approximate time scales for a single spore (3×10^{-5} s) up to three orders of magnitude larger. As described above, the fluid time scale has been selected so that small particles essentially follow the gas-phase flow while the largest particles significantly lag behind the gas phase. Since the wide range of relevant particle-flow time scales is covered in this study, it is desirable to extend the results to other parameter regimes with suitable normalization in the future. Table 7.1 shows the particle properties used in the study.

The schematic configuration of the jet flow is shown in Fig. 7.1. The flow is bounded by a wall on the left side of the domain while it is open on the right side of the domain. Four particles are located in the region between the left side of jet and the wall, and four other particles are

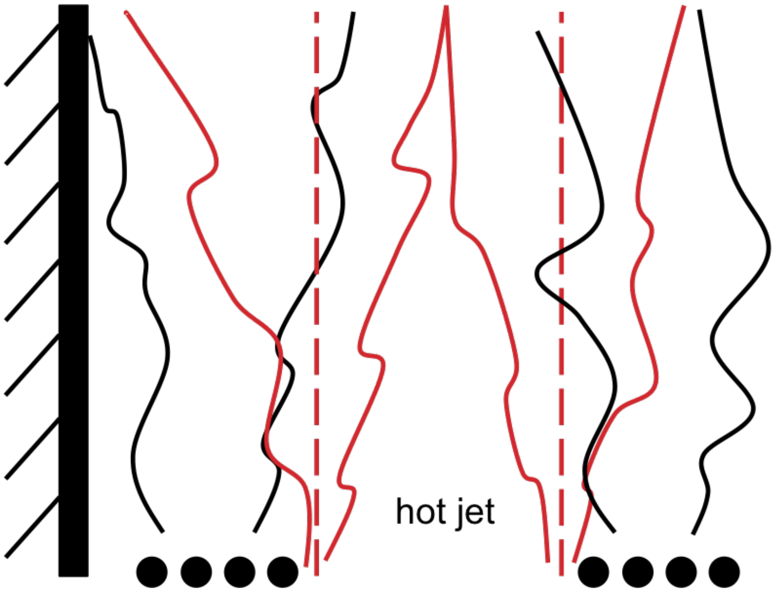

Figure 7.1: Schematic plot of hot jet configuration interacting with eight particles.

placed on the opposite side of the jet where the flow is unbounded. The initial particle locations, y_{p0}, are 0.02, 0.04, 0.06, 0.08, 0.27, 0.29, 0.31, and 0.33 m. The initial jet location is extended from 0.1 to 0.25 m. To better denote particle position relative to the jet, the simulation results use the initial particle positions expressed in terms of the jet radius, R. Thus, the particles on the wall side and open side have negative (left) and positive (right) initial position, respectively. That is, $y_{p0} = -2.07R$, $-1.80R$, $-1.53R$, $-1.27R$, $+1.27R$, $+1.53R$, $+1.80R$, and $+2.07R$. The particles and fluid flow starting from a given location can disperse in either direction leading to converging or non-converging paths as shown in Fig. 7.1. A particle initially closer to the high-temperature jet would be expected to experience more interactions with the jet flow. The instantaneous Type-I particle interaction model with one-way coupling is used with the one-way momentum and energy transfers from the gas phase to the particle phase. Statistical data are collected from 1024 realizations of the ODT simulations.

7.3 Results and discussion

7.3.1 Jet evolution

In common free shear flows the dilatation velocity is nominally centered on the jet, equivalent to matching pressure gradients on each end of the domain. However, in the wall-bounded jet flow, the wall boundary condition fixes the fluid velocity at the left wall so that dilatational velocities tend to increase with increasing distance from the wall. For the present simulation, this becomes significant in the early mixing period where the fast initial mixing leads to rapid dilatation and velocity change. When the jets are reacting flow, the dilatation is very strong, and this dilatational velocity is found to have an effect on the turbulent mixing and fluid dilution.

The high-temperature jet has low density so that the mixing results in a narrowing of the jet in a mass-weighted sense that shows less dispersion in terms of temperature than a jet without the strong density variation; this is a consequence of the differences in the density between the jet and the surrounding ambient air. Also, it is noteworthy that the jet carries less momentum and kinetic energy per volume than a jet at ambient temperatures. In Fig. 7.2, the average temperature field is depicted as it evolves over the duration of the simulation. The jet flow is rapidly mixed in the early evolution when the time scales are shortest. The turbulence time scale is initialized to 5×10^{-4} s based on the initial jet velocity and thickness and is expected to increase in time after an initial transient so that for most of the duration shown here, the time scale is expected to be comparable to, though several times less than, the evolution time.

Figure 7.2 also shows the trajectories of the average particle position in time. Only the trajectories of the nearest and furthest particles to the jet on each side are plotted for clarity because the other particles are bounded in the middle (shown in Sec. 7.3.2). Particle positions are discussed in detail below, but the trajectories here are a consequence of dilatation and inhomogeneous turbulence that leads to inhomogeneous dispersion. The density difference described above will be significant in interpreting the results and is further discussed here. The hot jet is initially seven times less dense than the ambient air. While the initial width of hot jet exceeds the thickness of the wall-side ambient region, the mass of air in the wall-side region is five times greater than the mass of air in the hot jet. As consequence, the mixing of the hot gases into the ambient air results in

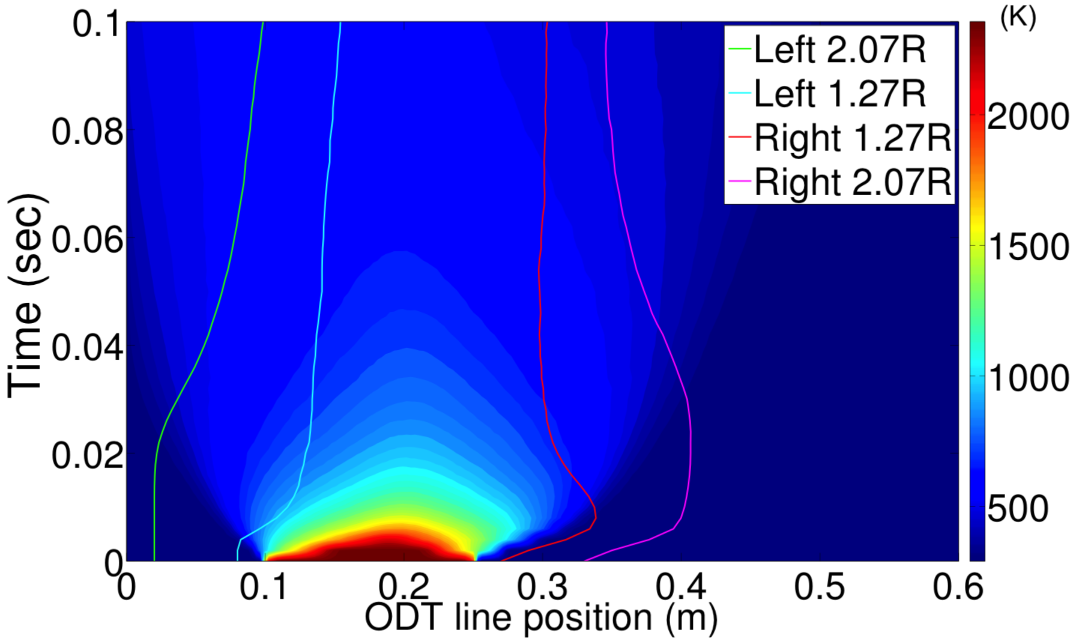

Figure 7.2: Gas temperature contours across the time-space domain simulated by the ODT model and the trajectories of the nearest and furthest particles to the jet on each side ($\tau_p = \tau_H = 0.03$ ms.

substantial and rapid cooling, and the hot jet is gradually diluted as it mixes with successive pairs of particles on each side of the jet.

To further describe the flow field interacting with the particles, the turbulent kinetic energy and its dissipation rate are computed from the statistics of the ODT velocity field. Based on these, the values of the integral time scales and the turbulent diffusivity can be obtained and their contour plots of time evolution are shown in Fig. 7.3. These provide a qualitative overview of the flow field evolution. The integral time scale is initially small as seen in Fig. 7.3, but it increases as turbulent mixing occurs so that the relevant integral time scales for most of the evolution ($10^{-2.5} - 10^{-1.5}\, s$) are a few times less than the evolution time. This is between the time scales of two larger particles ($\tau_p = \tau_H = 3$ ms and $\tau_p = \tau_H = 30$ ms). The spatial variation of the turbulent diffusivity across the domain is also shown in Fig. 7.3 for different evolution times. The inhomogeneity in the turbulent diffusivity plays a significant role in interpreting the results below. Fluid elements in the regions of higher turbulent diffusivity will be more strongly dispersed, and the particle following the fluid elements should be similarly affected and dispersed strongly. There are two turbulent effects related to the dispersion. First, during the development of the jet, there is a strong separation

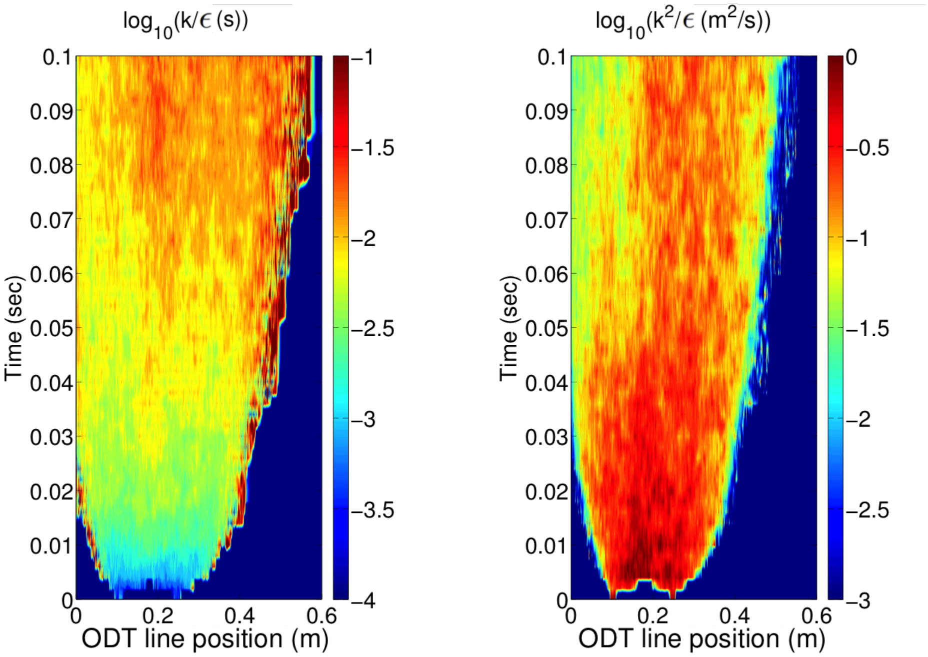

Figure 7.3: Contour plots for the integral time scale (left) and turbulent diffusivity (right) estimated from the turbulent kinetic energy and dissipation rate.

between the turbulent jet region with strong dispersion and the surrounding region with essentially no dispersion. Second, in the later evolution, the characteristics of a boundary layer flow essentially increases turbulent diffusivity farther from the wall associated with greater length scales.

7.3.2 Particle evolution

Figure 7.4 presents a series of instantaneous profiles from a single-realization simulation of the particle time scale $\tau_p = \tau_H = 0.03\ ms$. The results of typical particle trajectories exhibit instantaneous motion characteristic of the Type-I particle interaction in the ODT model. The temperature field felt by the particles and the particle temperature are also shown. These temperature profiles exhibit how the particle response lags behind the high frequency temperature fluctuations, which is particularly clear in Fig. 7.4(c) where the temperature of gas and particle are overlaid on each other. Since multiphase ODT is a stochastic model, single realizations have limited meaning, and the ensemble of these simulations are used to compute statistical properties of the two phases in turbulent flow.

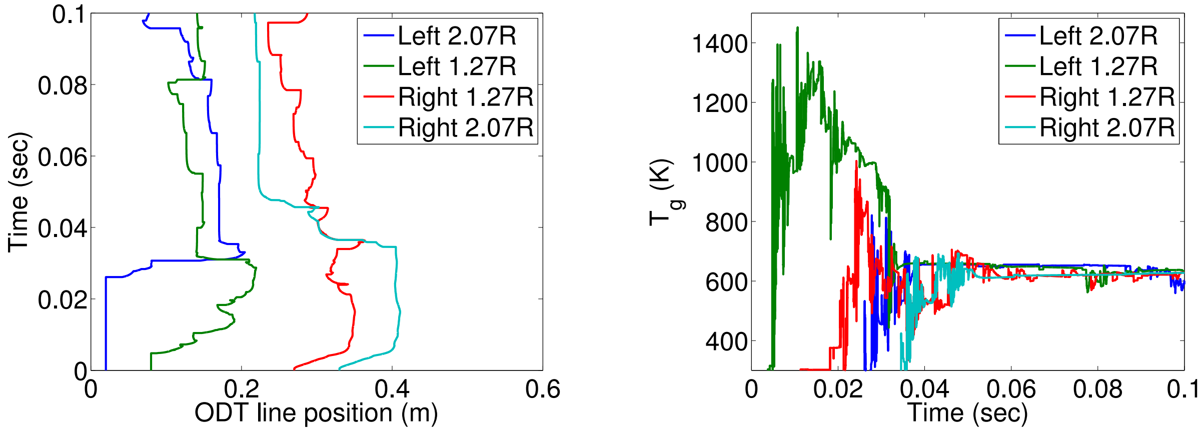

(a) Particle position

(b) Gas temperature environment of particles

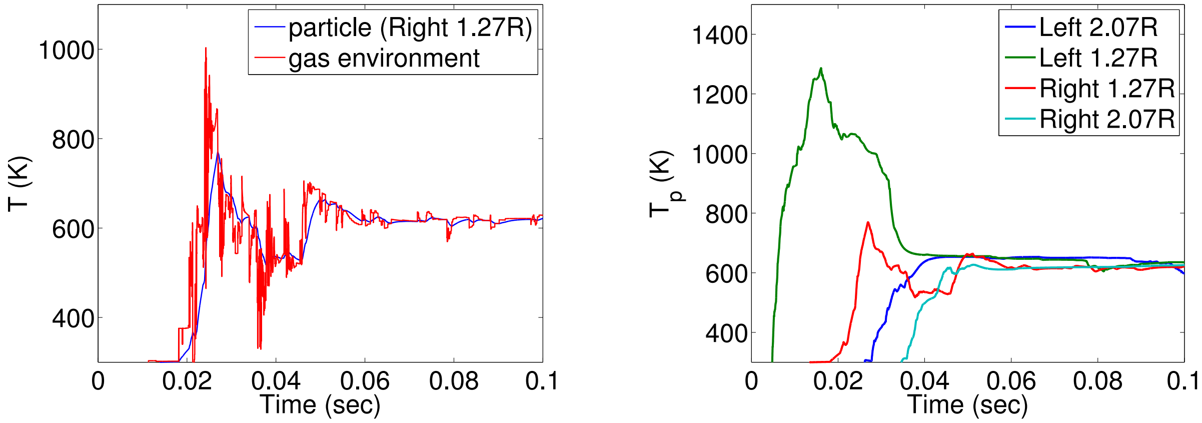

(c) Temperature evolution of a single particle at Right 1.27R and its local gas environment

(d) Particle temperature

Figure 7.4: Instantaneous profiles of particle evolution (single realization).

The particles are initially located either on the "wall side (Left)" or "open side (Right)" of the jet. This nomenclature will be used in the following discussion and plots. As introduced above, four particles are evenly distributed on each side of the jet.

Figure 7.5 shows the trajectories of the particles of different time scales on the "wall side (Left)" and "open side (Right)" of the jet overlaid on the temperature field across the ODT domain. Here, only the nearest and furthest particles to the jet are depicted for legible representation. Generally, the particles are pushed away from the wall because of the gas dilatation in the early evolution while the particles are drawn back into the jet later due to the mixing. Also, the particles with small inertial time scale, τ_p, are more likely to be affected by the turbulent field. More quantitative analysis of the evolution of these particles is discussed next.

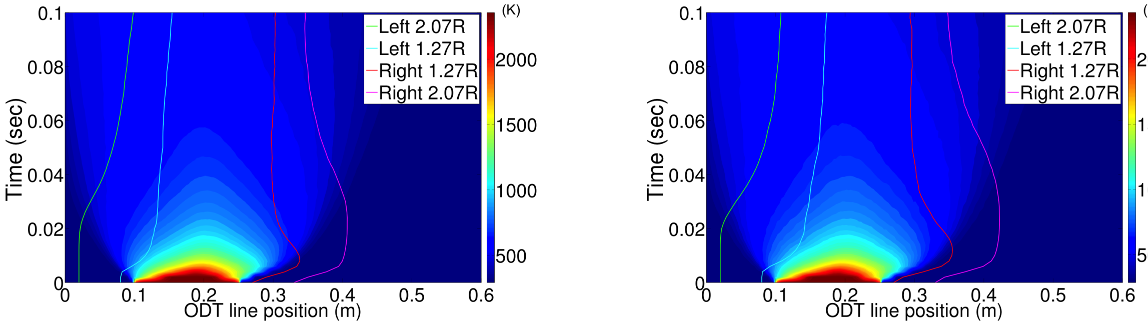

(a) $\tau_p = \tau_H = 0.03\ ms$ (b) $\tau_p = \tau_H = 0.3\ ms$

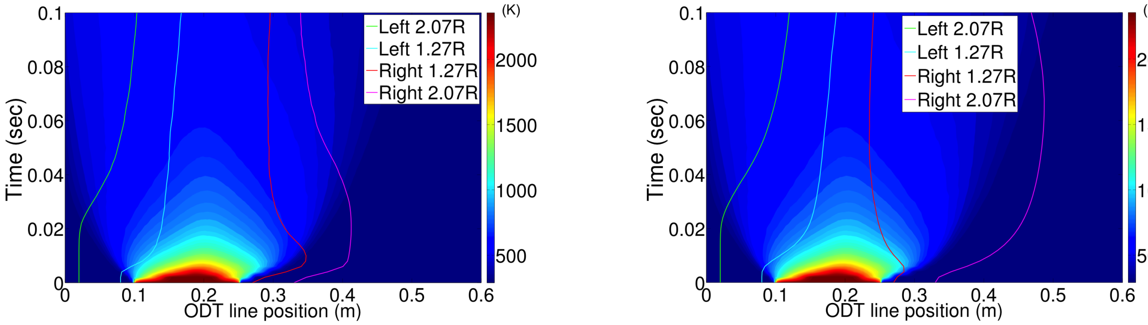

(c) $\tau_p = \tau_H = 3\ ms$ (d) $\tau_p = \tau_H = 30\ ms$

Figure 7.5: Trajectories of the nearest and furthest particles to the jet on each side overlaid on the mean gas temperature contours across the time-space domain simulated by the ODT model.

Particle position

The average positions of wall-side particles are shown in Fig. 7.6(a). The initial delay of particle dispersion appears before the jet interacts with the particles and the particles further from the jet delay longer. As the jet mixes with the successive particles, the particles near the mixing regions of high intensity have higher dispersion rates. The average particle positions also show that the particles tend to be entrained into the center of the jet where the turbulent intensity is high. This phenomenon results from the spatially inhomogeneous characteristic of the turbulence along the ODT domain shown in Fig. 7.3. These inhomogeneities in the turbulence lead to inhomogeneous particle dispersion. Once the jet interacts with the particles, the gradient of the turbulent diffusivity drives the particles towards the center of the jet. It is also noteworthy that the dilated and inhomogeneous turbulence causes an uncommon result, that is, heavy particles have large dispersion. This is attributed to the fact that these heavy particles disperse in the flow region of low turbulence intensity as indicated by their dispersion trajectories in Fig. 7.5. Initially the particles

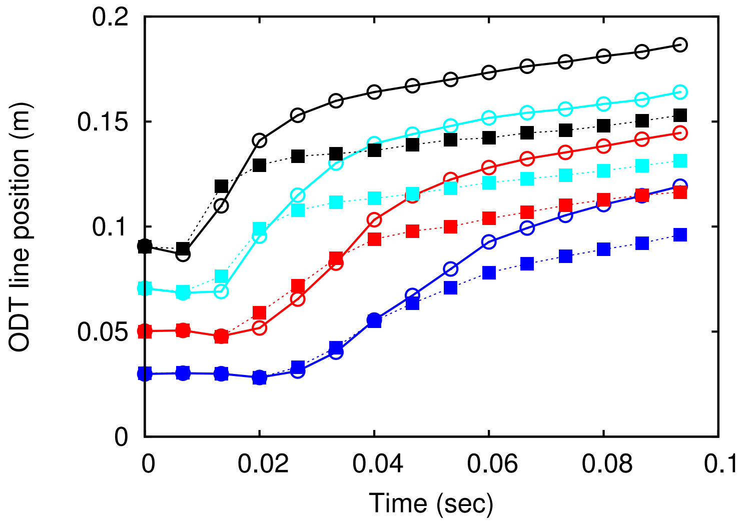

(a) Wall side. Initial particle position $y_{p0} = -2.07R$ (blue), $-1.80R$ (red), $-1.53R$ (cyan), and $-1.27R$ (black).

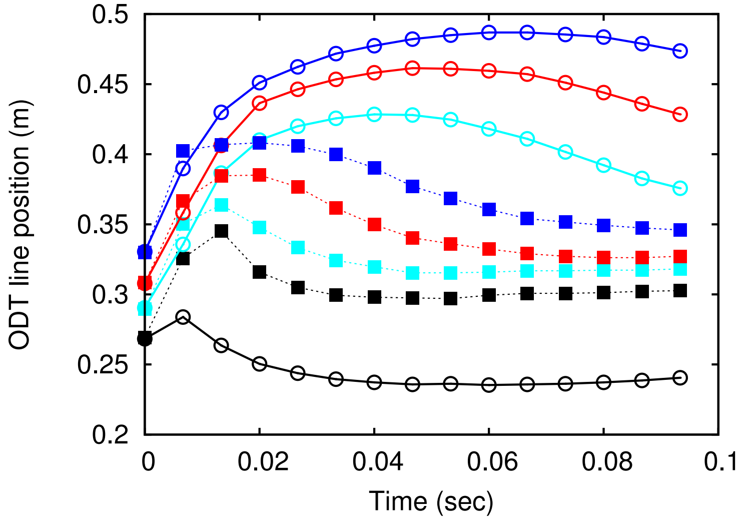

(b) Open side. Initial particle position $y_{p0} = +2.07R$ (blue), $+1.80R$ (red), $+1.53R$ (cyan), and $+1.27R$ (black).

Figure 7.6: Average particle positions. Solid lines represent $\tau_p = \tau_H = 30\ ms$; dash lines represent $\tau_p = \tau_H = 0.03\ ms$.

gain the momentum from the dilatation of flow field and disperse away from the jet. Later on the jet starts to interact with the particles and tends to move them to the jet center. In terms of the long inertial relaxation time, the heavy particles adapt to these interactions with the jet slower than the light particles, and therefore, disperse less towards the jet center.

The average position of open-side particles are shown in Fig. 7.6(b). As evident in their initial average dispersion behavior, the particles on the right side of the jet are pushed away from the jet field until they interact with the jet. This is because the wall position is fixed, and the dilatation effect on open-side increases away from the wall. The particles initially move toward the outside of jet center due to the dilatation. The particles have strong mixing from the jet on the right side. This tends to broaden the "tail" of the particle distribution towards the jet, which causes the mean of the particle distribution (the mean location) to bend inwards the jet center. This occurs since the particles begin as enssentially a delta function (a single location) with mixing concentrated on one side of that location. The mixing then draws the particle inward, which broadens the distribution tail and moves the mean particle locations inward towards the jet.

Figure 7.6(b) also shows that the heavy particles behave differently from the light particles. During the early mixing that leads to rapid dilatation, the nearest heavy particles (black solid line) to the jet lag behind the light particles (black dash line), and, therefore, are entrained to experience more interactions and mixed into the jet. However, later on, as the jet expands, other large particles (other solid lines) start to interact with the hot jet and tend to disperse toward the jet center during the late flow evolution. In summary, the nearest heavy particles mix more rapidly than the light particles because initially they exist in the flow region of high turbulent intensity; the farther heavy particles experience a delayed mixing interaction with the jet that is attributed to their initial positions beyond the majority of the turbulent jet region.

Gas temperature observed by particles

In order to predict the particle temperature, T_p, it is very important to investigate the temperature environment, T_g, of the gas phase to which the particles are exposed. Because of the thermal relaxation time, τ_H in Eq. 3.83, the particle temperature lags behind the observed gas temperature, as shown in Fig. 7.4.

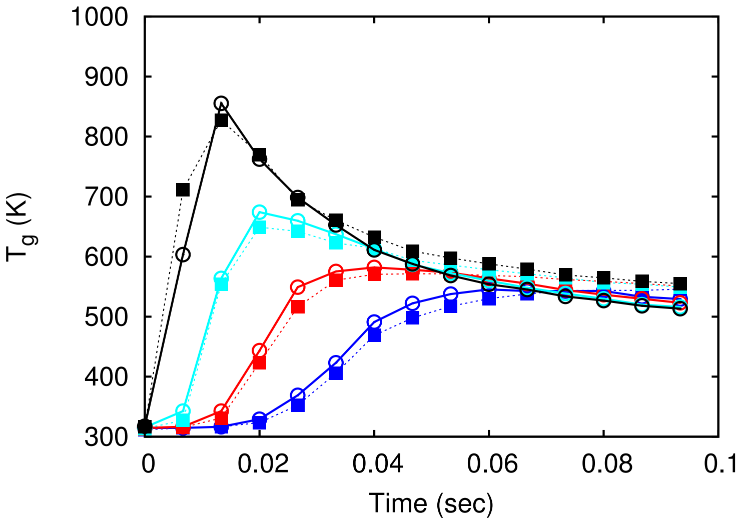

(a) Wall side. Initial particle position $y_{p0} = -2.07R$ (blue), $-1.80R$ (red), $-1.53R$ (cyan), and $-1.27R$ (black).

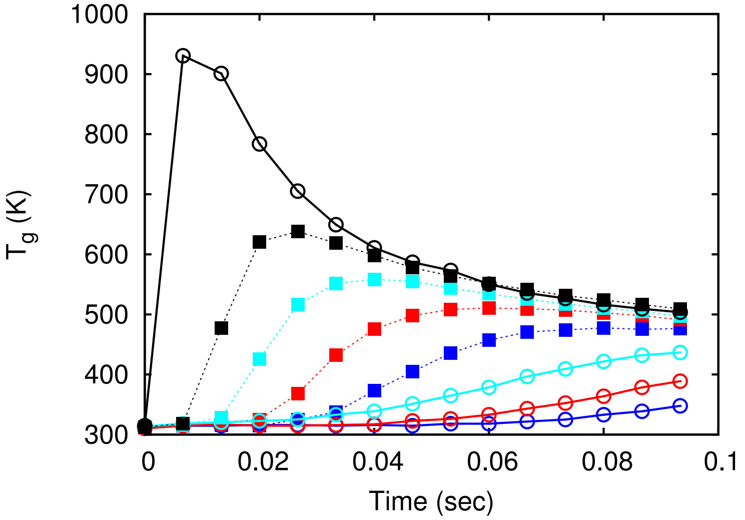

(b) Open side. Initial particle position $y_{p0} = +2.07R$ (blue), $+1.80R$ (red), $+1.53R$ (cyan), and $+1.27R$ (black).

Figure 7.7: Average gas temperature environment experienced by particles. Solid lines represent $\tau_p = \tau_H = 30\ ms$; dash lines represent $\tau_p = \tau_H = 0.03\ ms$.

The development of the temperature environment shows certain characteristics that are common to all the particles. The particles investigated here find themselves initially at ambient temperature. As the jet mixes with the surrounding air, the particles are entrained and heated by a hot gas environment. The highest temperatures undergone by the particles tend to be reached in the early stage because the hot jet is subsequently diluted so that the maximum temperature significant reduces.

The average gas temperatures observed by wall-side particles are plotted in Fig. 7.7(a). The average temperature is calculated by statistically collecting the environmental temperature experienced by each particle over its history. As expected, the particles near the jet are entrained into the jet earlier and experience higher temperatures. For the particles on the wall-side of the jet, there is little difference in the temperature environment observed by heavy and light particles. This is because heavy particles mix well with the jet and have a similar dispersion rate as light particles in the early period of jet evolution. Further downstream, the temperature gradient across the jet becomes smaller as the jet is cooled via turbulent mixing.

Figure 7.7(b) shows the mean gas temperature observed by open-side particles of different initial positions and different time scales. In contrast to the wall-side particles, there are significant differences in observed gas temperature for the heavy and small particles on the open side of the jet. The heavy particles nearest to the jet center (black solid line) lag the fluid elements and thus lag the dilatation of the jet, and are entrained in the jet first. So, compared to the light particles initialized at the same position (black dashed line), the heavy particles experience the high-temperature environment of the jet in the early stage of the jet evolution. For the other heavy particles (other solid lines), their delayed mixing with the hot jet lead to less interaction with the hot gas phase.

Particle temperature

The previous two subsections have addressed the particle dispersion and the temperature fields associated with the particles. In this section, the time evolution of particle temperature is investigated, which can be obtained by integration of Eq. 3.83.

Figure 7.8 shows the average temperatures of the wall-side and open-side particles. The particles near the jet region are entrained into the jet earlier, and, therefore, undergo the interactions with the gases of high temperature and are heated up rapidly. While the particle temperature

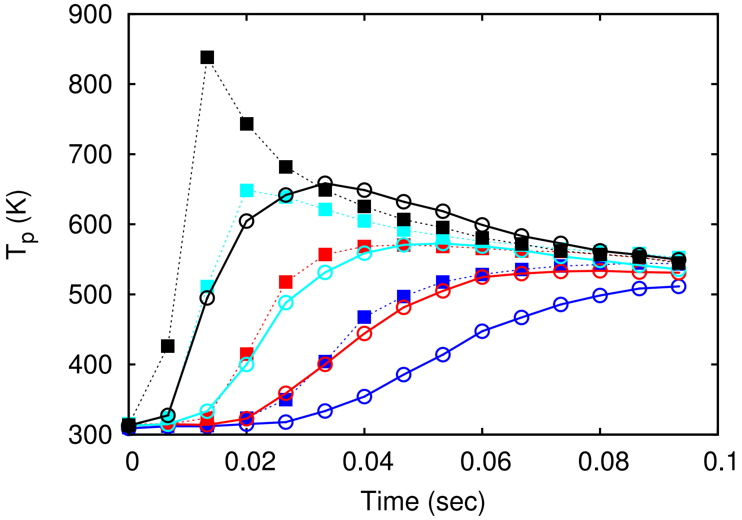

(a) Wall side. Initial particle position $y_{p0} = -2.07R$ (blue), $-1.80R$ (red), $-1.53R$ (cyan), and $-1.27R$ (black).

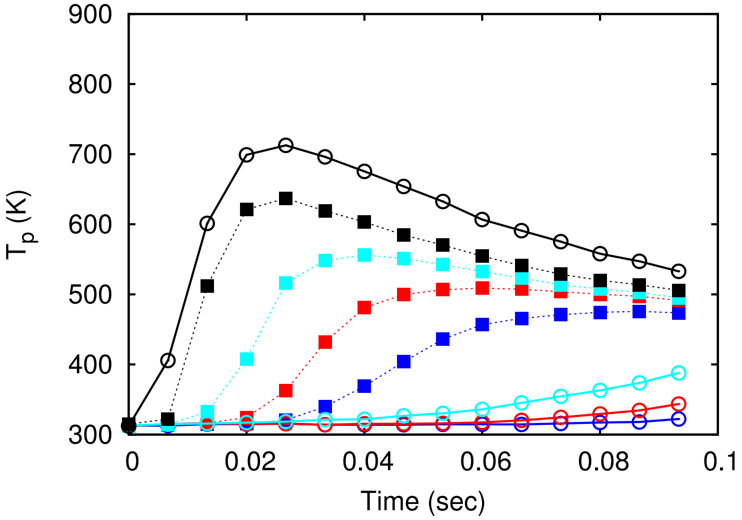

(b) Open side. Initial particle position $y_{p0} = +2.07R$ (blue), $+1.80R$ (red), $+1.53R$ (cyan), and $+1.27R$ (black).

Figure 7.8: Average particle temperature. Solid lines represent $\tau_p = \tau_H = 30$ *ms*; dash lines represent $\tau_p = \tau_H = 0.03$ *ms*.

lags behind the gas temperature of high fluctuations as shown in Fig. 7.4, both temperatures statistically look quite similar. For the particles of small τ_p and τ_H (dashed lines), their temperature follows the observed temperature of the gas environment as seen in Sec. 7.3.2. For the particles with a time scale relatively large compared to the turbulence time scales, the particle temperature significantly lags behind the gas temperature as shown with solid lines in Fig. 7.8. Take the light and heavy particles initially positioned at $-1.27R$ as an example. The light particles and the gas environmental temperature reach the maximum temperature of $850K$ at the same time of 0.01 s. In contrast, the heavy particles are heated up to the maximum temperature of $650K$ at 0.03 s that lag behind the evolution of their surrounding gas temperature which reach the maximum temeprature of $850K$ at 0.01 s. These comparisons are shown in Figs. 7.7 and 7.8.

Another primary objective of the study in this chapter is to develop the capability to help understand the statistical probability that the particles exposed to the elevated gas temperature environment are neutralized. Although the deactivation mechanism is not clear so far, the experimental work to study the effects on spores in a high-temperature gas environment provide evidence of the deactivation [106]. The present work does not try to include any chemical effect associated with the neutralization. Instead, the statistics of the maximum particle temperature are obtained as a representative measure of neutralization.

The probability distributions of the maximum temperature of the particles of different initial positions and different time scales are shown in Fig. 7.9. The heavy particles (dark blue distribution) reach relatively reduced maximum temperature because they tend to move away from the region of high temperature as shown with solid lines in Fig. 7.6. As an exception, the particles of the largest $\tau_p = \tau_H = 30\ ms$ on the open-side of the jet reach a high maximum temperature as well. Because when they are mixed with hot gases in the early evolution, these particles experience much more interactions with the jet than other heavy particles initialized with different locations. The light particles near the jet center (the blue distribution in the rightmost panel on the top row and the leftmost panel on the bottom row) have wide distributions, as they are more likely to move around and gradually spread the distribution away from the hot region. It is also seen that heavy particles far away from the jet on the open-side (dark blue distribution in the two rightmost panels on bottom row) have little opportunity to interact with the hot jet, most of which stay near ambient temperature during the entire evolution.

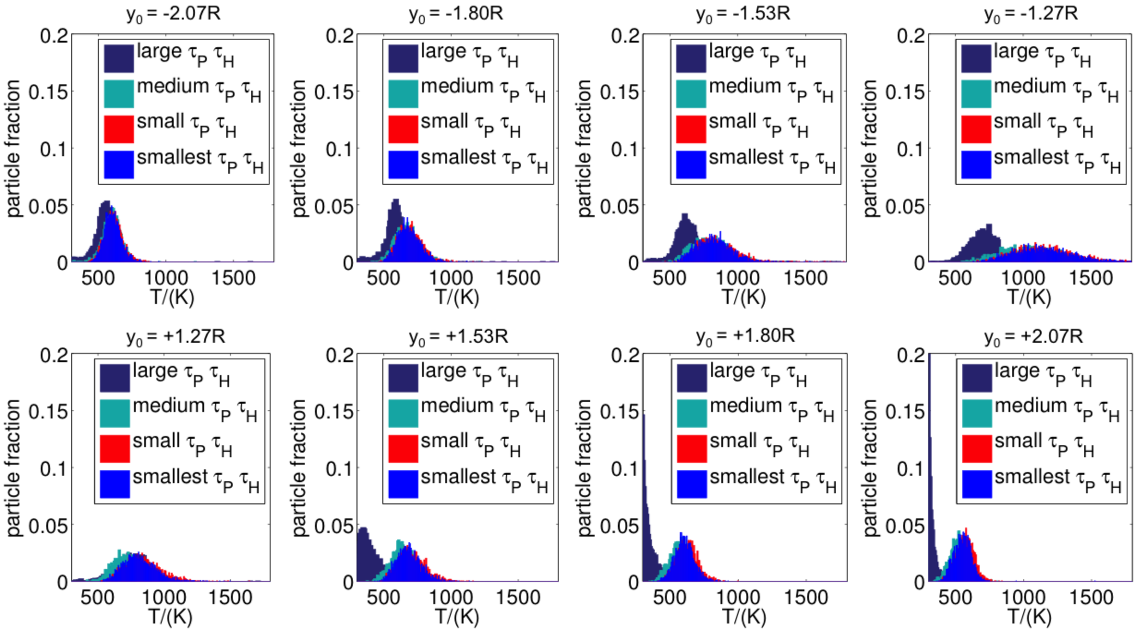

Figure 7.9: Maximum temperature PDF of particles. Particle time scales are represented by smallest $\tau_p = \tau_H = 0.03$ ms, small $\tau_p = \tau_H = 0.3$ ms, medium $\tau_p = \tau_H = 3$ ms, and large $\tau_p = \tau_H = 30$ ms.

7.4 Conclusions

In this chapter, the ODT multiphase model is extended to a nonisothermal hot jet configuration. This study is first of its kind where the turbulent jet is bounded by the wall on one side that includes the physics of interest and practical applications (e.g. neutralization of biological spores achieved by heating of post-detonation combustion). The present study focused on evaluating the model's ability to capture important statistics of the temperature history of the particles involving the jet evolution. Four simulation cases of the particles of different τ_p and τ_H are considered in this study, each of which has eight different initial particle positions y_{p0} outside the jet region. The largest particle class significantly lags behind the flow evolution, while the intermediate and small particle classes do not follow the high fluctuations of jet flow but do follow the evolution of the average gas velocity and temperature.

The simulations are performed using one-way momentum and energy coupling. It is observed that for the particles near the hot jet, they respond less to the dilatation effect and are entrained into the jet and heated rapidly. However, the particles farther away from the jet follow the inertial trajectories that delay the interactions with the jet. Interestingly, the dilatation and inhomogeneous nature of the turbulence lead to an uncommon result of large dispersion of heavy particles. The highest temperature experienced by the particles is reached in the early stage of the jet evolution. The light particles near the jet region are able to reach the high temperature and have the wide distribution of the maximum temperature. The results presented here indicate that the model can qualitatively predict the important particle statistics in the jet.

CHAPTER 8. SUMMARY AND RECOMMENDATIONS

This chapter summarizes the work presented in the dissertation and recommends the future work that can be continued based on the present work.

8.1 Summary of results

The comprehensive ODT multiphase model is developed and validated in different flow configurations to understand the particles dynamics in turbulent flow. The ODT multiphase models are formulated in a Lagrangian reference frame that is common for particle trajectory models. One of the unique advantages of the model is that it resolves the full range of time and length scales, with detailed particle transport as well as particle-turbulence interactions in the flow evolution. This work tends to form a sound physical and numerical basis for model formulations and provides an improved numerical understanding of the interactions between particles and a turbulent fluid phase. The following paragraphs highlight the main findings of the projects discussed in this dissertation. A more detailed summary can be found at the end of each chapter.

In the ODT formulation of the gas phase, the turbulent advection is implemented by instantaneous events of scalar rearrangement through eddy triplet maps. Intuitively, an instantaneous (Type-I) multiphase interaction approach originally proposed in [17] is implemented in the current ODT model (Chapter 4). The essential nature of the particle-eddy interaction is best understood under simplified conditions. With a detailed numerical description of particle interactions with the turbulence, the model is used to simulate the particle behavior in homogeneous decaying turbulence. Particle dispersion, dispersion coefficients, velocity statistics, and integral time scales are presented. The ODT model generally performs well and is able to capture two most important fundamental phenomena of the particles, namely, inertial effects and the trajectory crossing effect. In the current implementation, the adjustable particle parameter, β_p, is the only new one introduced into the ODT model. The model parameter β_p scales the eddy time and the eddy gas velocity. The sensitivity of results to this model parameter is presented. The optimal value of β_p is 0.05 in the homogeneous decaying turbulence.

Two new variants of the multiphase interaction model (continuous Type-C and combined Type-IC) are developed in this work (Chapter 5). The model differences are investigated by comparing three different approaches in the predictions of particle transport in a turbulent round jet flow. The models have been validated for a range of characteristic particle response times and jet Reynolds numbers. The Type-I model provides good predictions to particle dispersion, but does not allow the particles to interact with multiple eddies simultaneously. The Type-C model resolves the above drawback of the Type-I model by allowing continuous particle-eddy interactions for the finite evolution time. However, Type-C model is not able to match the tracer limit and therefore only accurately predicts the high Stokes number particles. The Type-IC model combines the features of the Type-I and -C models, which is considered as the most robust PEI model among the three. The optimal value of β_p is found to be 0.08 in the jet flow.

A two-way momentum coupling mechanism is proposed and implemented to allow the gas motion to be modulated by the particles (Chapter 6). Momentum transfer between the phases is accounted for through source terms from the particles in the diffusion equations. To couple with eddy motions, the source term is implemented in a new kernel transformation and an iterative procedure for eddy selection. The two-way coupling mechanism extends the application scope of the ODT multiphase model to the turbulent particle-laden flows. In this work, the methodology is validated in a turbulent particle-laden jet in a temporally evolving planar configuration. The turbulence modulation effect of particle addition on the mean and RMS axial velocity of the gas phase is investigated. The development of particle velocity in the axial and radial directions and particle number distribution are illustrated. The simulation results compared to the experimental data show that the model qualitatively captures the flow modulation with the presence of different particle classes with different solid loadings.

The temperature evolution of the particles along their trajectories is simulated in a hot jet (Chapter 7). This study is the first of its kind where the turbulent jet is bounded by the wall on one side that includes the physics of interest and practical attractions in civilian and commercial fields. The present study addresses the post-blast-phase mixing between biological agent particles, the environment that is intended to neutralize them, and the ambient environment that dilutes the jet flow. The results presented here suggest that the model can qualitatively predict the important particle statistics in jet flames.

8.2 Recommendation for future work

The ODT multiphase models apply the relatively simple representations of the interplay between the diffusion and turbulent advection for the evolution of the particle and gas phases. The ability of the current models to capture a number of important features of turbulent multiphase flows makes them valuable tools for understanding particle-turbulence interactions. The following recommendations are now suggested for future efforts towards making the models more useful in the multiphase fields.

- The current models simulate the particle dispersion in temporal form, and the space-time mapping is made [11] to compare the results with spatial data. The ODT equations of the spatial formulation are mentioned in Chapter 3 and can be used to develop the formulation of spatially evolving particles for the direct comparison. Extension of the particle models to the spatial ODT formulation should be straightforward.
- In the simulations of turbulent jet flow, the initial conditions are specified using a hyperbolic tangent function. However, in the real experimental systems, the turbulence has been fully developed at the nozzle exit. The initial conditions can affect the mixing and evolution of the particles in the near and far fields. Using the conditions that best represent the experimental data are recommended for more accurate simulation predictions.
- For the present work, the ODT multiphase models are developed and implemented in the Cartesian coordinates. ODT has been formulated in cylindrical coordinates [13], where the ODT line is oriented in the radial direction, and the axial velocity is the critical one that drives the turbulence in the model. Hence, the author recommends to implement the particle model in cylindrical coordinates for consistent modeling, especially in round jets. This would allow the model to apply for more interesting validation cases including reactive particle-laden round jet flames and plumes. Our research group has recently completed a cylindrical ans spatial ODT formulation, though particles have not yet been implemented

into the model. However, the methods described in this dissertation can be carried over directly to the cylindrical coordinate system with very minor modifications.

- As demonstrated in Chapter 6, the two-way momentum coupling mechanism has been developed in the Type-I model and validated in a particle-laden jet flow. The author has implemented the two-way momentum coupling mechanism in the two other ODT multiphase models (Type-C and -IC). A similar validation case as that shown in Chapter 6 could be undertaken to compare the performance of the three ODT multiphase models in turbulent particle-laden flows.

REFERENCES

[1] Baxter, L. L., 1989. “Turbulent transport of particles.” PhD thesis, Brigham Young University. vi, 24, 25

[2] Snyder, W. H., and Lumley, J. L., 1971. “Some measurements of particle velocity autocorrelation functions in a turbulent flow.” *Journal of Fluid Mechanics,* **48**, pp. 41–71. vi, viii, ix, 11, 47, 49, 53, 55, 56, 57, 61, 62, 65, 69

[3] Wells, M. R., and Stock, D. E., 1983. “The effects of crossing trajectories on the dispersion of particles in a turbulent flow.” *Journal of Fluid Mechanics,* **136**, pp. 31–62. vi, viii, ix, 11, 47, 53, 55, 56, 58, 61, 69

[4] Schmidt, J. R., Wendt, J. O. L., and Kerstein, A. R., October 2004. “Prediction of particle laden turbulent channel flow using one dimensional turbulence.” In *Proceedins of the IUTAM Symposium on Computational Approaches to Disperse Multiphase Flow, Argonne, IL.* viii, 8, 15, 22, 27, 28, 30, 31, 35, 47, 72

[5] Sun, G., Lignell, D. O., Hewson, J. C., and Gin, C. R., 2014. “Particle dispersion in homogeneous turbulence using the one-dimensional turbulence model.” *Physics of Fluids (1994-present),* **26**(10), p. 103301. viii, 5, 34, 45, 72, 77, 80, 81, 88, 89

[6] Berrouk, A. S., 2011. *Stochastic Lagrangian Modeling for Large Eddy Simulation of Dispersed Turbulent Two-Phase Flows*. Bentham Science Publishers. 2

[7] Kerstein, A. R., 1999. “One-dimensional turbulence: model formulation and application to homogeneous turbulence, shear flows, and buoyant stratified flows.” *Journal of Fluid Mechanics,* **392**, pp. 277–334. 3, 13, 14, 15, 21, 46, 48, 55, 72

[8] Kerstein, A. R., Ashurst, W. T., Wunsch, S., and Nilsen, V., 2001. “One-dimensional turbulence: vector formulation and application to free shear flows.” *Journal of Fluid Mechanics,* **447**, pp. 85–109. 3, 15, 22, 46, 49, 72

[9] Ashurst, W. T., and Kerstein, A. R., 2005. “One-dimensional turbulence: variable density formulation and application to mixing layers.” *Physics of Fluids,* **17-025107**, pp. 1–26. 3, 15, 20, 21, 22, 32, 46, 49, 72

[10] Echekki, T., Kerstein, A. R., and Dreeben, T. D., 2001. “One-dimensional turbulence simulation of turbulent jet diffusion flames: model formulation and illustrative applications.” *Combustion and Flame,* **125**, pp. 1083–1105. 3, 15, 47, 49, 72

[11] Hewson, J. C., and Kerstein, A. R., 2001. “Stochastic simulation of transport and chemical kinetics in turbulent CO/H_2/N_2 flames.” *Combustion Theory and Modelling,* **5**, pp. 669–697. 3, 15, 16, 22, 47, 49, 72, 73, 88, 135

[12] Hewson, J. C., and Kerstein, A. R., 2002. "Local extinction and reignition in nonpremixed turbulent CO/H_2/N_2 jet flames.." *Combustion Science and Technology,* **174**, pp. 35–66. 3, 15, 22, 72

[13] Krishnamoorthy, N., 2008. "Reaction models and reaction state parameterization for turbulent nonpremixed combustion." PhD thesis, The University of Utah. 3, 15, 135

[14] Ricks, A. J., Hewson, J. C., Kerstein, A. R., Gore, J. P., Tieszen, S. R., and Ashurst, W. T., 2010. "A spatially developing one-dimensional turbulence (ODT) study of soot and enthalpy evolution in meter-scale buoyant turbulent flames." *Combustion Science and Technology,* **182**, pp. 60–101. 3, 15, 72

[15] Punati, N., Sutherland, J. C., Kerstein, A. R., Hawkes, E. R., and Chen, J. H., 2011. "An evaluation of the one-dimensional turbulence model: Comparison with direct numerical simulations of CO/H_2 jets with extinction and reignition." *Proceedings of the Combustion Institute,* **33**, pp. 1515–1522. 3, 15

[16] Lignell, D. O., Kerstein, A. R., Sun, G., and Monson, E. I., 2012. "Mesh adaption for efficient multiscale implementation of one-dimensional turbulence." *Theoretical and Computational Fluid Dynamics*. 3, 15, 16, 20, 46, 48, 50, 64, 72, 88, 118

[17] Schmidt, J. R., 2004. "Stochastic models for the prediction of individual particle trajectories in one dimensional turbulence flows." PhD thesis, The University of Arizona. 3, 9, 29, 51, 133

[18] Deardorff, J. W., 1970. "A numerical study of three-dimensional turbulent channel flow at large reynolds numbers." *Journal of Fluid Mechanics,* **41**(02), pp. 453–480. 7

[19] Orzag, S., and Patterson Jr, G., 1972. *Numerical simulation of turbulence, Statistical Models and Turbulence Lecture Notes in Physics 12*. Springer-Verlag. 7

[20] Launder, B. E., and Spalding, D. B., 1972. *Lectures in mathematical models of turbulence*. Academic press. 7

[21] Launder, B., Reece, G. J., and Rodi, W., 1975. "Progress in the development of a reynolds-stress turbulence closure." *Journal of Fluid Mechanics,* **68**(03), pp. 537–566. 7

[22] Moin, P., and Mahesh, K., 1998. "Direct numerical simulation: a tool in turbulence research." *Annual Review of Fluid Mechanics,* **30**(1), pp. 539–578. 7

[23] Rouson, D., and Eaton, J., 1994. "Direct numerical simulation of particles interacting with a turbulent channel flow." In *Proceedings of the 7th Workshop on Two-Phase Flow Predictions, Erlangen, Germany*. 7

[24] Li, D., Fan, J., Luo, K., and Cen, K., 2011. "Direct numerical simulation of a particle-laden low reynolds number turbulent round jet." *International Journal of Multiphase Flow,* **37**(6), pp. 539–554. 7, 71, 108, 111

[25] Schmidt, J. R., Wendt, J. O., and Kerstein, A. R., 2006. "Prediction of particle laden turbulent channel flow using one-dimensional turbulence." In *IUTAM Symposium on Computational Approaches to Multiphase Flow*, Springer, pp. 433–441. 7, 35

[26] Schmidt, J. R., Wendt, J. O., and Kerstein, A. R., 2009. “Non-equilibrium wall deposition of inertial particles in turbulent flow.” *Journal of Statistical Physics,* **137**(2), pp. 233–257. 7, 22, 35, 47

[27] Alfonsi, G., 2009. “Reynolds-averaged navier–stokes equations for turbulence modeling.” *Applied Mechanics Reviews,* **62**(4), p. 040802. 8

[28] Hirsch, C., and Tartinville, B., 2009. “Reynolds-averaged navier-stokes modelling for industrial applications and some challenging issues.” *International Journal of Computational Fluid Dynamics,* **23**(4), pp. 295–303. 8

[29] Young, J., and Leeming, A., 1997. “A theory of particle deposition in turbulent pipe flow.” *Journal of Fluid Mechanics,* **340**, pp. 129–159. 8

[30] Berlemont, A., Desjonqueres, P., and Gouesbet, G., 1990. “Particle lagrangian simulation in turbulent flows.” *International Journal of Multiphase Flow,* **16**(1), pp. 19–34. 8, 23

[31] Mason, P. J., 1994. “Large-eddy simulation: A critical review of the technique.” *Quarterly Journal of the Royal Meteorological Society,* **120**(515), pp. 1–26. 8

[32] Hilbert, R., Tap, F., el Rabii, H., and Thevenin, D., 2004. “Impact of detailed chemistry and transport models on turbulent combustion simulations.” *Progress in Energy and Combustion Science,* **30**, pp. 61–117. 9

[33] Wang, H., Du, D., Sung, C. J., and Law, C. K., 1996. “Experiments and numerical simulation on soot formation in opposed-jet ethylene diffusion flames.” *Proceedings of the Combustion Institute,* **26**, pp. 2359–2368. 9

[34] Yuu, S., Ueno, T., and Umekage, T., 2001. “Numerical simulation of the high reynolds number slit nozzle gas–particle jet using subgrid-scale coupling large eddy simulation.” *Chemical Engineering Science,* **56**(14), pp. 4293–4307. 9, 11, 72

[35] Armenio, V., Piomelli, U., and Fiorotto, V., 1999. “Effect of the subgrid scales on particle motion.” *Physics of Fluids (1994-present),* **11**(10), pp. 3030–3042. 9

[36] Miller, R. S., and Bellan, J., 2000. “Direct numerical simulation and subgrid analysis of a transitional droplet laden mixing layer.” *Physics of Fluids (1994-present),* **12**(3), pp. 650–671. 9

[37] Shirolkar, J., Coimbra, C., and McQuay, M., 1996. “Fundamental aspects of modeling turbulent particle dispersion in dilute flows.” *Progress in Energy and Combustion Science,* **22**, pp. 363–399. 9, 24, 45, 46, 51, 63, 77

[38] Elghobashi, S., 1991. “Particle-laden turbulent flows: direct simulation and closure models.” *Applied Scientific Research,* **48**(3-4), pp. 301–314. 9

[39] Elghobashi, S., 1994. “On predicting particle-laden turbulent flows.” *Applied Scientific Research,* **52**(4), pp. 309–329. 9

[40] Yudine, M., 1959. “Physical consideration on heavy particle diffusion.” *Advances in Geophysics,* **6**, pp. 185–191. 10, 47, 77

[41] Csanady, G., 1963. "Turbulent diffusion of heavy particles in the atmosphere." *Journal of Atmospheric Science,* **20**, pp. 201–208. 10, 23, 47, 58, 64

[42] Hinze, J., 1971. "Turbulent fluid and particle interaction." *Progress in heat and mass transfer,* **6**, pp. 433–452. 10

[43] Reeks, M., 1977. "On the dispersion of small particles suspended in an isotropic turbulent fluid." *Journal of Fluid Mechanics,* **83**(03), pp. 529–546. 10

[44] Squires, K. D., and Eaton, J. K., 1991. "Measurements of particle dispersion obtained from direct numerical simulations of isotropic turbulence." *Journal of Fluid Mechanics,* **226**, pp. 1–35. 10, 11, 108, 111

[45] Wang, L.-P., and Stock, D. E., 1993. "Dispersion of heavy particles by turbulent motion." *Journal of the Atmospheric Sciences,* **50**(13), pp. 1897–1913. 10

[46] Pozorski, J., and Minier, J.-P., 1998. "On the lagrangian turbulent dispersion models based on the langevin equation." *International Journal of Multiphase Flow,* **24**(6), pp. 913–945. 10, 11

[47] He, Z., Liu, Z., Chen, S., Weng, L., and Zheng, C., 2005. "Particle behavior in homogeneous isotropic turbulence." *Acta Mechanica Sinica,* **21**(2), pp. 112–120. 10

[48] Jung, J., Yeo, K., and Lee, C., 2008. "Behavior of heavy particles in isotropic turbulence." *Physical Review E,* **77**(1), p. 016307. 10

[49] Maxey, M., and Riley, J., 1983. "Equation of motion for a small rigid sphere in a nonuniform flow." *Physics of Fluids,* **26**, pp. 883–889. 10, 46

[50] Fung, J., Hunt, J., and Perkins, R., 2003. "Diffusivities and velocity spectra of small inertial particles in turbulent–like flows." In *Proceedings of the Royal Society of London A: Mathematical, Physical and Engineering Sciences*, Vol. 459, The Royal Society, pp. 445–493. 11

[51] Yeh, F., and Lei, U., 1991. "On the motion of small particles in a homogeneous isotropic turbulent flow." *Physics of Fluids A: Fluid Dynamics (1989-1993),* **3**(11), pp. 2571–2586. 11

[52] Lu, Q., 1995. "An approach to modeling particle motion in turbulent flowsi. homogeneous, isotropic turbulence." *Atmospheric Environment,* **29**(3), pp. 423–436. 11

[53] Lightstone, M., and Raithby, G., 1998. "A stochastic model of particle dispersion in a turbulent gaseous environment." *Combustion and flame,* **113**(3), pp. 424–441. 11

[54] Hennick, E. A., and Lightstone, M., 2000. "A comparison of stochastic separated flow models for particle dispersion in turbulent flows." *Energy & fuels,* **14**(1), pp. 95–103. 11

[55] Reynolds, A., and Iacono, G. L., 2004. "On the simulation of particle trajectories in turbulent flows." *Physics of Fluids (1994-present),* **16**(12), pp. 4353–4358. 11

[56] Yuu, S., Yasukouchi, N., Hirosawa, Y., and Jotaki, T., 1978. “Particle turbulent diffusion in a dust laden round jet.” *AIChE Journal,* **24**(3), pp. 509–519. 11, 23

[57] Yuu, S., Ikeda, K., and Umekage, T., 1996. “Flow-field prediction and experimental verification of low reynolds number gas-particle turbulent jets.” *Colloids and Surfaces A: Physicochemical and Engineering Aspects,* **109**, pp. 13–27. 11

[58] Chung, J., and Troutt, T., 1988. “Simulation of particle dispersion in an axisymmetric jet.” *Journal of Fluid Mechanics,* **186**, pp. 199–222. 12

[59] Longmire, E. K., and Eaton, J. K., 1992. “Structure of a particle-laden round jet.” *Journal of Fluid Mechanics,* **236**, pp. 217–257. 12, 111

[60] Sbrizzai, F., Verzicco, R., Pidria, M. F., and Soldati, A., 2004. “Mechanisms for selective radial dispersion of microparticles in the transitional region of a confined turbulent round jet.” *International Journal of Multiphase Flow,* **30**(11), pp. 1389–1417. 12

[61] Hansell, D., Kennedy, I., and Kollmann, W., 1992. “A simulation of particle dispersion in a turbulent jet.” *International Journal of Multiphase Flow,* **18**(4), pp. 559–576. 12

[62] Barlow, R., and Morrison, C., 1990. “Two-phase velocity measurements in dense particle-laden jets.” *Experiments in Fluids,* **9**(1-2), pp. 93–104. 12

[63] Shuen, J.-S., Solomon, A., Faeth, G., and Zhang, Q.-F., 1985. “Structure of particle-laden jets-measurements and predictions.” *AIAA journal,* **23**(3), pp. 396–404. 12

[64] Jou, B.-H., Sheen, H.-J., and Lee, Y.-T., 1993. “Particle mass loading effect on a two-phase turbulent downward jet flow.” *Particle & particle systems characterization,* **10**(4), pp. 173–181. 12

[65] Tsuji, and Nagano, 1989. “Velocity and temperature measurements in a natural convection boundary layer along a vertical flat plate.” *Experimental Thermal and Fluid Science,* **2**, pp. 208–215. 12

[66] Sheen, H., Jou, B., and Lee, Y., 1994. “Effect of particle size on a two-phase turbulent jet.” *Experimental Thermal and Fluid Science,* **8**(4), pp. 315–327. 12

[67] Modarress, D., Elghobashi, S., and Tan, H., 1984. “Two-component lda measurement in a two-phase turbulent jet.” *AIAA Journal,* **22**(5), pp. 624–630. 12

[68] Gore, R., and Crowe, C. T., 1989. “Effect of particle size on modulating turbulent intensity.” *International Journal of Multiphase Flow,* **15**(2), pp. 279–285. 13

[69] Tu, J., and Fletcher, C., 1994. “An improved model for particulate turbulence modulation in confined two-phase flows.” *International communications in heat and mass transfer,* **21**(6), pp. 775–783. 13

[70] Kenning, V., and Crowe, C., 1997. “On the effect of particles on carrier phase turbulence in gas-particle flows.” *International journal of multiphase flow,* **23**(2), pp. 403–408. 13

[71] Yarin, L., and Hetsroni, G., 1994. “Turbulence intensity in dilute two-phase flows3 the particles-turbulence interaction in dilute two-phase flow.” *International Journal of Multiphase Flow,* **20**(1), pp. 27–44. 13

[72] Punati, N., 2012. “An eulerian one-dimensional turbulence model: application to turbulent and multiphase reacting flows.” PhD thesis, University of Utah. 15, 22, 72

[73] Wunsch, S., and Kerstein, A., 2001. “A model for layer formation in stably stratified turbulence.” *Physics of Fluids,* **13**, pp. 702–712. 19

[74] Gosman, A., and Loannides, E., 1983. “Aspects of computer simulation of liquid-fueled combustors.” *Journal of Energy,* **7**(6), pp. 482–490. 23, 46, 51, 63

[75] Shuen, J., Chen, L., and Faeth, G., 1983. “Evaluation of a stochastic model of particle dispersion in a turbulent round jet.” *AIChE Journal,* **29**, pp. 167–170. 23, 46, 51, 63

[76] Zhou, Q., and Leschziner, M., 1991. “A time-correlated stochastic model for particle dispersion in anisotropic turbulence.” In *8th Symposium on Turbulent Shear Flows, Volume 1*, Vol. 1, pp. 10–3. 23

[77] Ormancey, A., and Martinon, J., 1984. “Prediction of particle dispersion in turbulent flows.” *PhysicoChemical Hydrodynamics,* **5**, pp. 229–244. 23

[78] Clift, R., Grace, J. R., and Weber, M. E., 1978. *Bubbles, drops and particles*. Academic Press, New York. 26

[79] Lynch, P., Krier, H., and Glumac, N., 2009. “A correlation for burn time of aluminum particles in the transition regime.” *Proceedings of the Combustion Institute,* **32**(2), pp. 1887–1893. 42

[80] Glumac, N., and Krier, H., 2012. Fundamental particle combustion kinetics measurement in the shock tube in support of enhanced blast weapons development Tech. rep., DTIC Document. 42

[81] Sullivan, K., Piekiel, N., Wu, C., Chowdhury, S., Kelly, S., Hufnagel, T., Fezzaa, K., and Zachariah, M., 2012. “Reactive sintering: an important component in the combustion of nanocomposite thermites.” *Combustion and Flame,* **159**(1), pp. 2–15. 42

[82] Gottiparthi, K. C., Menon, S., Elert, M. L., Buttler, W. T., Borg, J. P., Jordan, J. L., and Vogler, T. J., 2012. “Simulations of heterogeneous detonations and post-detonation turbulent mixing and afterburning.” In *AIP Conference Proceedings-American Institute of Physics*, Vol. 1426, p. 1639. 42

[83] Menon, S., Gallagher, T., and Muralidharan, B., 2012. Hybrid solution-adaptive unstructured cartesian method for large-eddy simulation of detonation in multi-phase turbulent reactive mixtures Tech. rep., DTIC Document. 42

[84] Loth, E., 2000. “Numerical approaches for motion of dispersed particles, droplets and bubbles.” *Progress in Energy and Combustion Science,* **26**, pp. 161–223. 45, 59

[85] Einstein, A., 1905. “On the movement of small particles suspended in stationary liquids required by the molecular-kinetic theory of heat.” *Annalen der Physik,* **17**, pp. 549–560. 45

[86] Einstein, A., 1926 reprinted 1956. *Investigations on the theory of Brownian movement.* 45

[87] Taylor, G. I., 1921. “Diffusion by continuous movements.” *Proc. London Math. Soc.,* **20**, pp. 196–211. 46

[88] Batchelor, G. K., 1949. “Diffusion in a field of homogeneous turbulence.” *Australian Journal of Scientific Research, Series A: Physical Sciences,* **2**, pp. 437–450. 46

[89] Saffman, P., 1965. “The lift on a small sphere is slow shear flow.” *Journal of Fluid Mechanics,* **22**, pp. 385–400. 46

[90] Kerstein, A. R., 1991. “Linear-eddy modelling of turbulent transport. part 6. microstructure of diffusive scalar mixing fields.” *Journal of Fluid Mechanics,* **231**, pp. 361–394. 46, 47

[91] Ashurst, W. T., Kerstein, A. R., Pickett, L. M., and Ghandhi, J. B., 2003. “Passive scalar mixing in a spatially developing shear layer: Comparison of one-dimensional turbulence simulations with experimental results.” *Physics of Fluids,* **15**, pp. 579–582. 47

[92] Lignell, D. O., and Rappleye, D., 2012. “One-dimensional-turbulence simulation of flame extinction and reignition in planar ethylene jet flames.” *Combustion and Flame,* **159**, pp. 2930–2943. 47

[93] McDermott, R. J., 2005. “Toward one-dimensional turbulence subgrid closure for large-eddy simulation.” PhD thesis, The University of Utah. 48

[94] Hoffman, J. D., 2001. *Numerical Methods for Engineers and Scientists*. CRC Press, New York. 50

[95] Yeh, F., and Lei, U., 1991. “On the motion of small particles in a homogeneous isotropic turbulent flow.” *Phys. Fluids A,* **3**, pp. 2571–2586. 57

[96] Chien, K.-Y., 1982. “Predictions of channel and boundary-layer flows with a low-reynolds-number turbulence model.” *AIAA Journal,* **20**(1), pp. 33–38. 71

[97] Almeida, T. G., and Jaberi, F. A., 2008. “Large-eddy simulation of a dispersed particle-laden turbulent round jet.” *International Journal of Heat and Mass Transfer,* **51**(3), pp. 683–695. 72, 108, 111

[98] Kennedy, I. M., and Moody, M. H., 1998. “Particle dispersion in a turbulent round jet.” *Experimental Thermal and Fluid Science,* **18**, pp. 11–26. 73, 85

[99] Kerstein, A. R., 2013. “Hierarchical parcel-swapping representation of turbulent mixing. part 1. formulation and scaling properties.” *Journal of Statistical Physics,* **153**(1), pp. 142–161. 73, 100

[100] Kerstein, A. R., 2014. “Hierarchical parcel-swapping representation of turbulent mixing. part 2. application to channel flow.” *Journal of Fluid Mechanics,* **750**, pp. 421–463. 73, 95

[101] Taylor, G. I., 1922. "Diffusion by continuous movements." *Proc. London Math. Soc,* **20**(1), pp. 196–212. 83, 85

[102] Batchelor, G., 1957. "Diffusion in free turbulent shear flows." *Journal of Fluid Mechanics,* **3**(01), pp. 67–80. 86

[103] Budilarto, S. G., 2003. "An experimental study on effects of fluid aerodynamics and particle size distribution in particle-laden jet flows." PhD thesis, Purdue University. 93, 94

[104] Maxey, M., 1987. "The gravitational settling of aerosol particles in homogeneous turbulence and random flow fields." *Journal of Fluid Mechanics,* **174**, pp. 441–465. 111

[105] Hewson, J. C., Lignell, D. O., and Sun, G., 2014. "Statistics of particle time-temperautre histories." *Sandia report*. 117

[106] Kumar, R., Saurav, S., Titov, E., Levin, D., Long, R., Neely, W., and Setlow, P., 2011. "Thermo-structural studies of spores subjected to high temperature gas environments." *International Journal of Heat and Mass Transfer,* **54**(4), pp. 755–765. 118, 130